Energinet Eltransmission A/S

Lot 2 (Kriegers Flak II)

Wind Assessment

REPORT

Date: 2024-09-24
Doc. No: 23072-04-03
Revision: 4

C2Wind ApS | Vesterballevej 5 | 7000 Fredericia | Denmark

C2WIND

Document information and change log.

Revision	Date	Status / Reason for Issue	Author	Checker
0	2024-08-02	Issued for internal review	RGA/DIB	JOG
1	2024-08-19	Issued for Client	JOG	CBM
2	2024-09-05	Addressing Client comments	JOG	RGA
3	2024-09-20	Addressing Client comments	DIB	JOG
4	2024-09-24	Final version to Client	DIB	JOG

Section	Summary of Changes (latest revision only)
All	Final version to Client

C2WIND

Table of Contents

Abbreviations	
AGL	Above Ground Level
ASL	Above Surface Level. This is used when a surface-following vertical reference is needed for measurements on land, whereas SWL is typically used for the same purpose at sea (although ASL could in principle be used there as well).
CRS	Coordinate Reference System
DLC	Design Load Case Table
ECD	Extreme Direction Change
ECN	Energy research Centre of the Netherlands
EDC	Extreme Direction Change
EOG	Extreme Operating Gust
ETM	Extreme Turbulence Model
EVA	Extreme Value Analysis
EWM	Extreme Wind Model
EWS	Extreme Wind Shear
FEED	Front-End Engineering Design
FLS	Floating LiDAR System, Fatigue Limit State
HAT	Highest Astronomical Tide
ibid.	From Latin ibidem ("in the same place"), it is used to save space in textual references to a quoted work, or another section in the present document, which has been mentioned in a previous reference.
IFORM	Inverse first-order reliability method
ILA	Integrated Load Analysis
LAT	Lowest Astronomical Tide
MoMM	Mean Of Monthly Means
MSL	Mean Sea Level
NaN	Not a Number
NSS	Normal Sea State
NTM	Normal Turbulence Model
NWP	Normal Wind Profile
RNA	Rotor-Nacelle Assembly
SWL	Still Water Level
WTG	Wind Turbine Generator

Subscripts	
Hub	Value at Hub height
Free	Undisturbed inflow, i.e. Free Stream
Mean	Mean value
Ref	Reference
Agg	Aggregate (i.e. composed of several parts)

Symbols	
Latin characters	
WS, V	Wind Speed
WD	Wind Direction
N	Number of independent environmental states
A	Weibull scale parameter
k	Weibull shape parameter
g	9.815 m/s^2 is the gravitational acceleration[1]
h	Height
P	Pressure
P_x	Upper x % quantile of a set of values; e.g. P_{90} is the 90 % quantile
TI	Turbulence Intensity
t	Timestamp, i.e. a time-coordinate
T	Temperature, Time period (two separate meanings)
R	Ideal gas constant
RelH	Relative humidity
z	Elevation (i.e. vertical coordinate) above a vertical reference.
Greek characters	
ρ	Density
μ	Mean value
σ	Standard deviation
α	Power-law wind shear exponent

[1] See: https://www.wolframalpha.com/input?i=acceleration+of+gravity+at+r%C3%BCgen

Executive Summary

The present document gives input to the document WTG Site Conditions Assessment for the Kriegers Flak II Offshore Wind farm (KFII), and it is intended for this project only. It covers the analysis of wind conditions and other atmospheric conditions.

The document provides input to:

- The site-specific design of support structures (including towers) for the Wind Turbine Generators (WTGs).
- The evaluation of site suitability of the Rotor-Nacelle Assemblies (RNAs).

The results are referenced below:

Still Water Levels		**Reference**
0 mMSL = 0 mDVR90		Section 1.2
Normal conditions parameters. Given at h_{Hub} = 150.0 mDVR90		**Reference**
Weibull Mean wind speed	Not summarised; see Table 6-1	Appendix A & Table 6-1
Omni-directional Weibull wind speed distribution parameters	Not summarised; see Table 6-1	Appendix A & Table 6-1
Wind profile for wind speed extrapolation with elevation	$WS(z) = WS_{Hub}\left(\frac{z}{h_{Hub}}\right)^{0.089}$ Here, z and h_{Hub} are in mMSL.	Section 6.2.1
Wind profile for load calculations, Normal Wind Profile (NWP)	$WS_{NWP}(z) = WS_{NWP,Hub}\left(\frac{z}{h_{Hub}}\right)^{0.124}$ Here, z and h_{Hub} are in mMSL.	Section 6.2.2
Normal Turbulence Model (NTM)	Not summarised; see Table 6-4	Section 6.3.1
Extreme Turbulence Model (ETM)	Largest of: ➢ IEC Class IB in Table 6-5 ➢ Centre-wake TI(WS)	Section 6.3.2
Normal ambient air temperature range	-7 °C ≤ T < 26.0 °C	Section 6.4.1
Design temperature (lowest daily mean temperature)	0.1 °C	Section 6.4.1
Relative humidity limit	RelH ≤ 100 %	Section 6.4.2

Extreme conditions parameters (Extreme Wind speed Model, EWM). Given at h_{Hub} = 150.0 mDVR90		**Reference**
Wind profile for load calculations	$WS(z) = WS_{Hub}\left(\frac{z}{h_{Hub}}\right)^{0.11}$ Here, z and h_{Hub} are in mMSL.	Section 8.1
Wind profile for extreme wind speed extrapolation with elevation	$WS(z) = WS_{Hub}\left(\frac{z}{h_{Hub}}\right)^{0.11}$ Here, z and h_{Hub} are in mMSL.	Section 8.1
Mean air density	$\rho_{Hub,EWM} = 1.21\ \frac{kg}{m^3}$	Section 8.2
Maximum 10-minute mean wind speed for a 1-year EWM	$WS_{1,Hub}$ = 30.2 m/s	Section 8.3.6
Maximum 10-minute mean wind speed for a 50-year EWM	$WS_{50,Hub}$ = 38.0 m/s	Section 8.3.6
Turbulence Intensity for use with EWM	TI_{EWM} = 11 %	Section 8.4
Other Conditions Given at h_{Hub} = 150.0 mDVR90		Reference
Extreme ambient air temperature range, 1-hour mean:	- 10.0 °C ≤ T < 31.0 °C	Section 6.4.1
Mean air temperature at hub height	8.7 °C	Section 6.4.1

1. Introduction

Energinet Eltransmission A/S (EE, or "the Client") has appointed C2Wind ApS (C2Wind) to carry out Site Wind Conditions Assessment for the Kriegers Flak II project (Lot 2), located in the Danish Baltic Sea. The purpose of this document is to serve as documentation of the wind conditions for WTG FEED. The document is based on an ongoing on-site measurement campaign, and it is intended to be amended by a subsequent note detailing any changes in the conclusions after completion of 12 months of on-site measurements.

1.1 Geographical location

The project site is located between 15 to 35 km off the eastern coast of Denmark, in the Danish Baltic Sea as shown in Figure 1-1. The project site has been further divided into two areas labelled KFII North and KFII South.

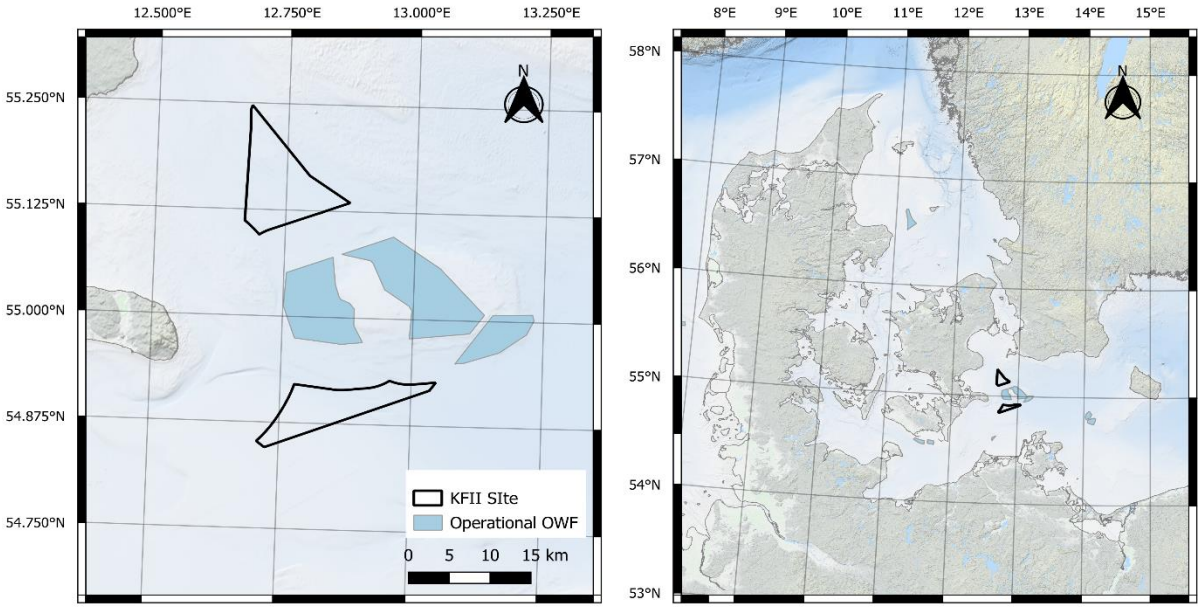

Figure 1-1: **Left**: Location of the KFII project area (black) and closest neighbouring OWFs in operation (blue). **Right**: Larger view of the Baltic Sea. CRS: WGS84.

1.2 General considerations

Elevations in the present document are, unless explicitly stated otherwise, given as distance above Mean Sea Level (MSL) in metres (mMSL). This is done to ease the incorporation of results based on a diverse range of datasets: floating Lidar measurements which provide 10-minute statistics relative to Still Water Level (SWL), model datasets with hourly resolution (or longer periods) whose vertical reference approaches MSL, as well as formulations such as the power law wind profile which are valid relative to a reference such as SWL or MSL but less so relative to a fixed reference like LAT. Nevertheless, this simplification does not introduce significant bias as the applicable vertical reference, DVR90, is approximately equal to MSL at the site, and the tidal range is negligible for the purposes of the present document.

The wind turbine hub height is assumed to be, following input from Energinet [MOMKOM]:

h_{Hub} = 150.0 mDVR90

The distance from MSL to DVR90 is negligible at the site, assuming that the statement in footnote 4 of [MAEIBS] is accurate and applicable to the site:

0 mMSL = 0 mDVR90

Where relevant, atmospheric parameters have been extrapolated to this elevation. For the purposes of the present document, and due to the modest variation of wind speed distribution with elevation, the results in the present report are assessed to be applicable without change for a hub height interval of ± 5 m about the value of h_{Hub} stated immediately above.

Since, as stated above, the results are valid for a hub height interval of ± 5 m, the results are reported at 150.0 mDVR90 only.

Throughout this report, wind directions are coming-from directions, and given as °N; i.e. clockwise compass directions as seen from above.

Density (scatter) plots throughout this report will show normalised densities according to the colour bar in Figure 1-2, where the normalisation is so that the maximum point density in each figure is unity.

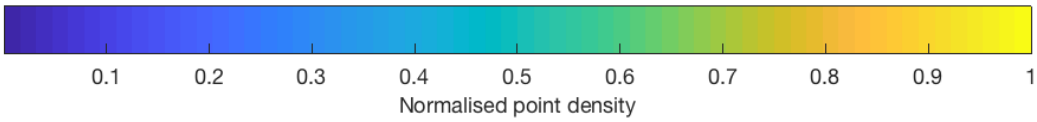

Figure 1-2: Colour bar showing the density of points in density (scatter) plots throughout the present report. Please note that the scatter point densities are normalised so that the maximum density is unity.

Finally, the following conventions and notations are used:

- Occasionally, some values are written in grey text. This is intended to highlight that they are intermediate results, and are included for information only.
- Intervals of numbers are denoted according to Item 2-7.7 of ISO 80000-2:2019-08 for closed intervals, and the optional notation of Items 2-7.8 through 2-7.10 of ibid. for half-open and open intervals[2].
    - For example, the interval from 0 to 1 is denoted:
        - [0;1] if both end points are included in the interval.
        - [0;1[if 0 is included in the interval, but 1 is not.
        -]0;1] if 0 is not included in the interval, but 1 is.
        -]0;1[if neither end point is included in the interval.

In most intervals in the present document, the lower end point is included, but the upper one is not.

[2] That is, the notation used for intervals of numbers is the second option here: https://en.wikipedia.org/wiki/Interval_(mathematics)#Including_or_excluding_endpoints, using semicolon as separator of endpoints as allowed by: https://en.wikipedia.org/wiki/Interval_(mathematics)#Notations_for_intervals.

2. Applied standards and guidelines

The present document is made in accordance with the following design standards and guidelines:

[IEC6131] : IEC 61400-3-1: Design requirements for fixed offshore wind turbines, ed. 1.0 (2019-04).
[IEC611] : IEC 61400-1: Design Requirements, ed. 4.0 (2019-02).
[DNV0126] : DNVGL-ST-0126 - Support structures for wind turbines (2021-12).
[DNV0437] : DNVGL-ST-0437 - Loads and site conditions for wind turbines (2021-11).

In case of discrepancy between the standards and guidelines above, the hierarchy of standards and guidelines is so that documents high on the list overrule documents lower on the list.

3. Overview of available data and review of data quality

3.1 Available data

The analyses presented in this report are based on measurement datasets: three floating Lidar Systems (FLSs) deployed at the KFII site and two FLSs deployed at the nearby Energy Island Bornholm site, see the descriptions in Appendix B. Additionally, data from the FINO2, Arkona and IJmuiden offshore met masts has been used for supplementary analyses related to temperature, turbulence and extreme wind speeds.

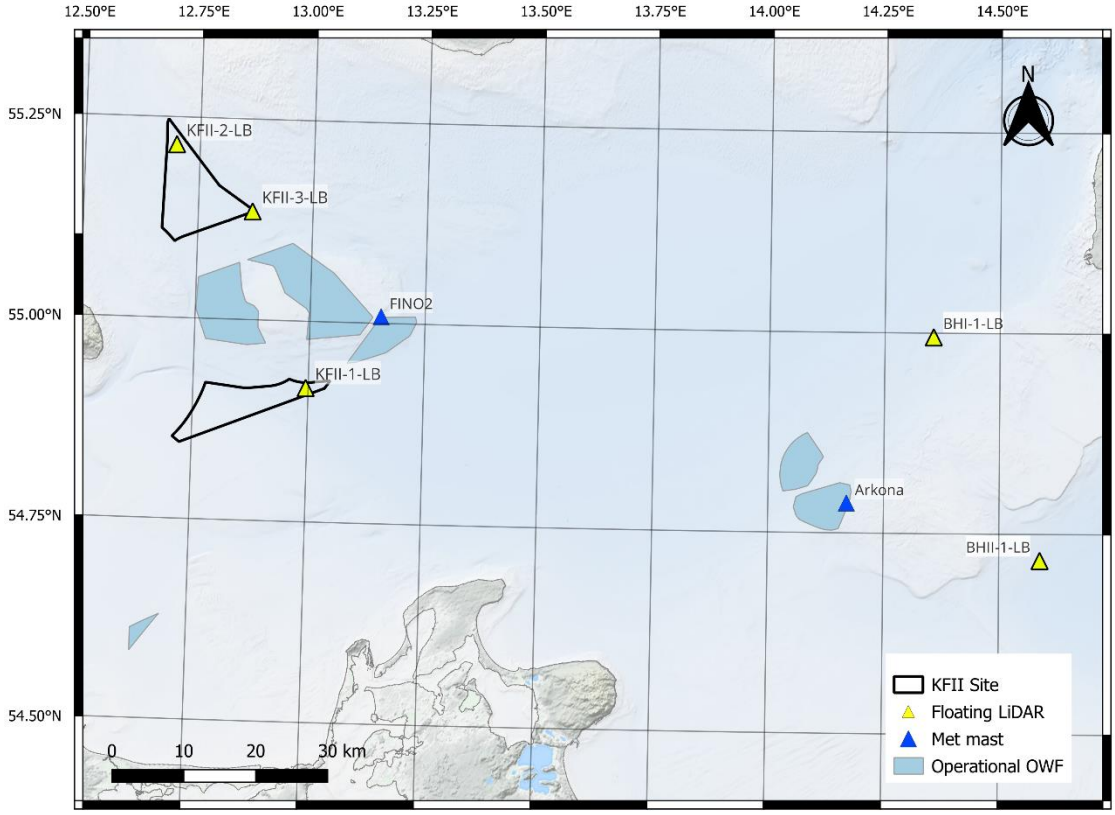

Figure 3-1: Location of the main measurement datasets used in this document. CRS: WGS84.

The measurement datasets used in the present chapter are summarised in Table 3-1. This table shows, each dataset and what it has been used for.

Dataset	Description	Weibull parameters	Shear	TI	Extreme Wind Model	P, T, RelH, air density
KFII FLSs	Appendix B.1	✓	✓	(✓)	×	(✓)
EIB FLSs	Appendix B.2	✓	(✓)	×	×	×
IJmuiden mast	Appendix A of [THORWA]	×	×	✓	×	×
FINO2 mast	Appendix B.3	×	×	✓	✓	(✓)
Arkona mast	Appendix B.4	×	×	(✓)	✓	×
Vortex time series	Not described	(✓)	(✓)	×	×	✓

Table 3-1: Overview of the datasets used in the analyses in the present report. Tick marks indicate that the data have been used for the purpose in the corresponding column, while crosses show that it has not been used for this purpose. Tick marks in parentheses indicate that the datasets have been used for

comparative purposes. A detailed description of the datasets is provided in the references listed in the table.

3.2 Sensor naming convention

The sensors have had names assigned to them, denoting their type, vertical coordinate, and the pointing compass direction of any boom they are mounted on (when relevant). The structure of the sensor names is thus:

{Data Type}_{Vertical Coordinate}_{Boom pointing compass direction}

Here, the {Data Type} field has one of the values in Table 3-2, whereas:

- {Vertical Coordinate} denotes the vertical coordinate above MSL in decimetres.
- {Boom pointing compass direction} denotes the pointing direction of the boom, the sensor is mounted on, in °N. For sensors not associated with a particular boom orientation, the orientation is either suppressed, or a 3-letter description is used instead: For top mounted sensors, "Top" is used, for aggregate sensors (i.e. composed of several sensors' signals), "Agg" is used, and for a virtual sensor at Hub height, "Hub" is used.

{Data Type}	Sensor type:	Symbol used in the present report	Unit
WS	Wind Speed	*WS*	m/s
WD	Wind Direction	*WD*	°N
T	Temperature	*T*	°C
RELH	Relative Humidity	*RelH*	%
P	Air pressure	*P*	hPa

Table 3-2: Data types in sensor names, their abbreviations, and their units.

Note that the sensor naming convention also applies to data from reanalysis and mesoscale models. When referring to data from these models, {*Boom pointing compass direction*} is set to NaN. This also applies to data from LiDAR measurements.

3.3 High-level quality check filters

In addition to the quantitative- and qualitative checks carried out when processing the data, high-level quality checks on the data have been carried out by discarding time stamps for which the data did not fulfil the following criteria:

Data field	Minimum value	Maximum value	Unit
Simple interval criteria			
WS 10-minute mean	0	100	m/s
WS 10-minute standard deviation	0	5	m/s
WS Gust	0	150	m/s
WD 10-minute mean	0	360	°N
T 10-minute mean	-50	100	°C
T 10-minute standard deviation	0	5	°C
T 10-minute maximum	-30	100	°C
P 10-minute mean	950	1050	hPa
RelH 10-minute mean	0	100	%
Other criteria			
WS 10-minute standard deviation must be larger than 0.001 m/s if *WS* 10-minute mean is larger than 0.5 m/s.			

Table 3-3: Initial, automated validation. It was visually checked that this did not exclude valid data. In addition to this very mild validation, validation by visual inspection was performed.

4. Generic methods

A set of generic methods has been used in the analyses carried out in the main body of this report, namely:

- Turbulence intensity detrending: This method accounts for upward or downward trends of wind speed during a 10-min sample which might cause an artificially large value of microscale turbulence.
- Mean-of-Monthly-Means (MoMM), which accounts for gaps in the time series.
- Power-law fit to the wind speed profile for every time stamp.

These generic methods are described in detail in Sections 4.1-4.3 below.

4.1 Turbulence Intensity detrending

Since the Turbulence Intensity (*TI*) is an important parameter in the assessment of the Normal- and Extreme Turbulence Model, the *TI* values, either from cup anemometers or floating Lidars, have been detrended when used in Section 6.3 and Appendix C. The detrending applied in the present report is a simple type of low-pass filtering or algorithm that removes any sudden increase in *TI* (removing any increase by more than 40% from one 10-minute sample to the next, though only in cases with *TI* larger than 8%). This method has been verified as being a conservative estimate using 1 Hz wind data from the Nysted Offshore Wind Farm. The detrended *TI* values are therefore derived as follows:

a) Compute *TI*, for all time stamps, from the 10-minute measurement time series.
b) Progressing through the time series from start to end, check for each timestamp $\{t_1\}$ whether:
    - *TI* at timestamp t_1, $TI(t_1)$, is larger than the $1.40 \cdot TI(t_0)$ at the preceding timestamp t_0. If the sampling time is 10 minutes, then $t_0 = t_1$ - 10 min.
    - The values of $TI(t_0)$ and $TI(t_1)$ are valid (i.e. their values exist and are not faulty).
    - $TI(t_1) > 0.08$.

If the conditions in item b) are fulfilled for timestamp t_1, set: $TI_{\text{Detrended}}(t_1) = TI(t_0)$. Otherwise, set: $TI_{\text{Detrended}}(t_1) = TI(t_1)$.

Detrending is introduced in order to remove events of very large turbulence intensity that are due to a change in mean wind speed (i.e. a trend in mean wind speed) rather than fluctuations around a more stable average level. The latter case would be microscale turbulence, whereas a mean wind speed change is not. C2Wind has carried out a validation of the method against high-frequency data from the IJmuiden met mast, finding that the detrending method applied to 10-minute data yields the same results as analysis of the high-frequency measurements in terms of NTM and ETM.

The aforementioned study is protected by an NDA and thus C2Wind can only share high-level findings, however, extensive checks are made to ensure that the detrending yields reasonable results for the datasets used in this document. For instance, a selection of these checks are illustrated by the plots in Figure 4-1, which show that the detrending affected the expected fraction of the *TI* values, 3.9% of the data points for the sensor labelled *WS_1020_180MC*, and that the effects of detrending are reasonable. Details on

this sensor are excluded from this section in order not to distract from the focus of showcasing the method, but more information can be found in Appendix B.3.

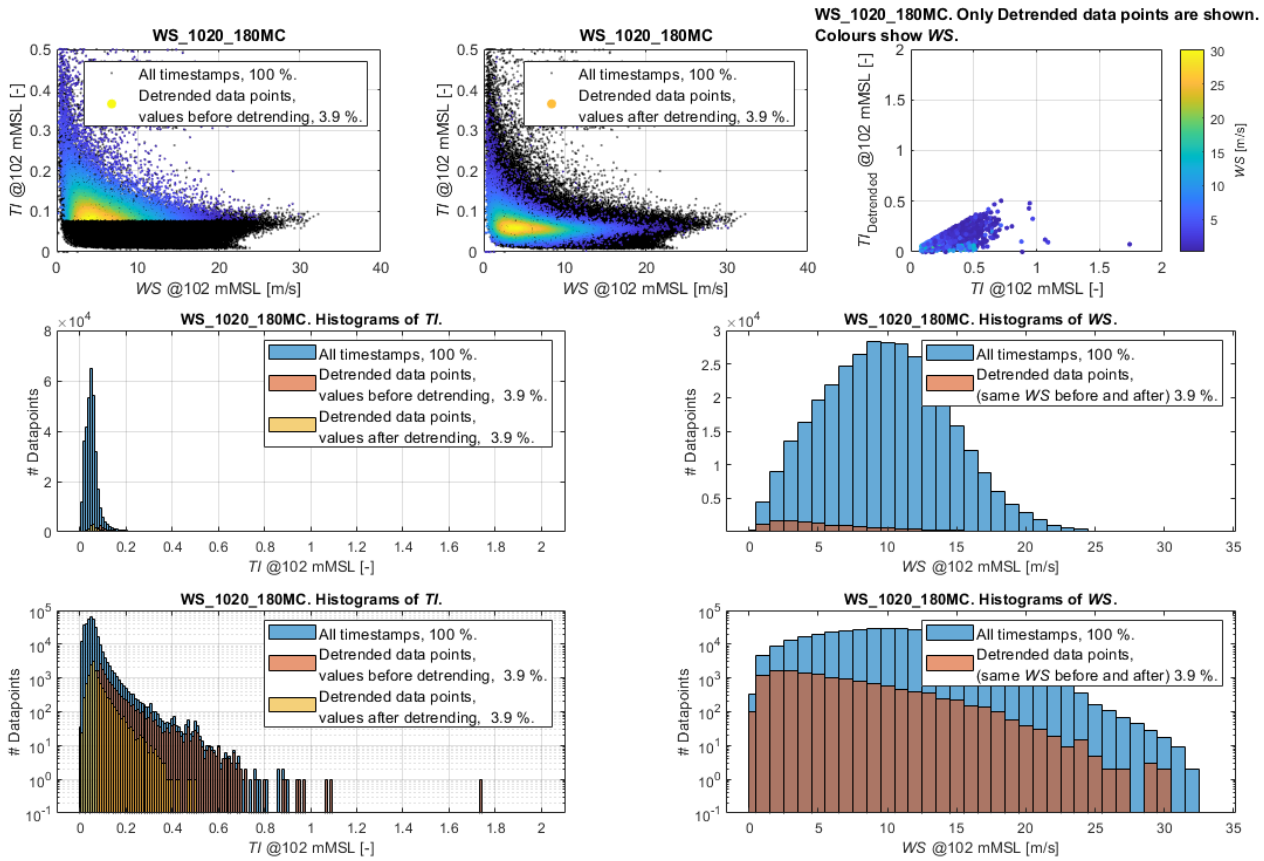

Figure 4-1: Comparison plots illustrating the effects of *TI* detrending for the sensor *WS_1020_180MC* at the FINO2 met mast: In total, 3.9% of the *TI* data is affected by the detrending, which is close to the fraction found for other offshore masts in similar locations. The plot on the upper left shows all values of *TI* vs. *WS* from *WS_1020_180MC* in black, and the affected data points before detrending coloured according to data point density. Please note that there are black points only for $TI \leq 0.08$ since these values are not affected by detrending as stated above. Analogously, the upper middle plot shows the same (coloured) data points, but plotted with their value after detrending. The plot on the upper right shows only those *TI* data points which are affected by detrending, with their detrended values vs. the value before detrending. The points are coloured according to the 10-minute mean wind speed associated with each data point, as shown by the colour bar. The plot on the middle left shows a histogram of the *TI* values: All values in blue, the points affected by detrending with their values before detrending in red, and the points affected by detrending with the values after detrending in yellow. Just below, on the lower left, the same histogram is shown, but with a logarithmic 2nd axis to better show the details. The plot on the middle right shows a histogram of the 10-minute mean wind speeds, where all values are shown in blue, and values with detrended *TI* are shown in red. Just below, on the lower right, the same histogram is shown, but with a logarithmic 2nd axis to better show the details.

4.2 Method of Mean-of-Monthly-Means: Handling missing data

To avoid data gaps and non-integer number of years of data skew the results, all normal conditions analyses in this report have used the method of mean-of-monthly-means. The name of the method "mean-of-monthly-means" has been taken from its use in the Windographer software documentation[3] to describe the method of weighting data points

[3] An example of using the expression "mean-of-monthly-means" is found in earlier versions of the documentation of the Windographer software.

by how often they occur in a month of the year. In the present report, it is implemented in the following way:

- Ascribe to each measurement data point an integer n ϵ [1,12], given by the month in which the data point is recorded.
- Ascribe to each data point a weight, which will be used to weigh the data point in all analyses where the mean-of-monthly-means is used. This weight equals the maximum number of data points that are possible[4] in the month n divided by the actual number of data points.

For example, if we look at a dataset containing 3 separate months of January with full data coverage of 10-minute values, there will be:
3 * 31 days * 24 hours/day * 6 data points/hour = 13,392 data points,
and each will be given a weight of:
(31 days * 24 hours/day * 6 data points/hour) / 13,392 data points = 1/3.

In this way, both non-integer numbers of years as well as gaps in the data will be corrected in a way that assumes the data is representative of both gaps and the missing fractions of years. It is worth noting that the MoMM method is used for calendar months with data gaps, however it is not used – or intended to be used – to bridge the gap in a measurement dataset covering less than a full calendar year.

4.3 Calculation of wind shear and extrapolating to hub height

When using any of the available floating Lidar datasets, a shear analysis is performed for each timestamp, thereby assigning a shear exponent value for each timestamp in the dataset. The shear analysis is done by a least-squares linear fit of the natural logarithm of the 10-minute mean *WS* vs. the natural logarithm of the sensor heights covering the rotor plane and up to 300 mASL (for this purpose, a rotor diameter of 236 m has been assumed, and the results are insensitive to changes, in the order of tens of meters, to this rotor diameter); thus, a power law shear profile is assumed.

[4] In this report, leap years are treated as if they have an extra day of measurements in February. Thus, a dataset with a single year, which has a leap-year February with all possible data points, will have each of these February-data points given a weight of 28/29.

5. Selection of representative analysis points

The KFII OWF area stretches out for approximately 98.5 and 73 km^2 for the northern and southern sub-areas respectively. It is natural to expect a certain degree of geographical variation of the normal- and extreme conditions parameters across the large extent of the project area. For the purposes of the present document, and pursuant to the requirements in [ENCL5], a number of representative analysis points need to be defined.

This section presents the background and analyses leading to the selection of representative analysis points. The selection of analysis points is based both on the geographical variation of key parameters, as well as on the intended use of the conclusions of this document. That is, the goal is to provide a description of the site conditions that is both accurate and useable in the context of FEED of offshore WTGs and support structures.

For normal conditions, the discussion takes as a starting point the general geography of the area and utilises data from NORA3 and NEWA. Figure 5-1 shows the locations of the datasets from both NORA3 and NEWA used for the analyses in this section. The selected nodes have a spacing of approximately 3 km.

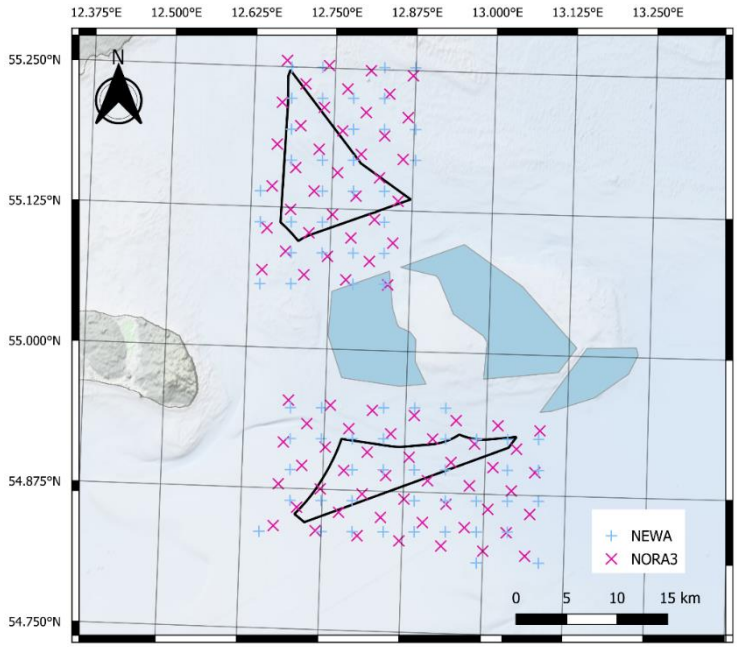

Figure 5-1: Locations of the NORA3 (magenta) and NEWA (light blue) nodes used for the analyses in this section. CRS: WGS84.

For the assessment of the spatial variability of normal conditions, data from both datasets was fetched for the entire period available then trimmed to full years only. This yields the period 1999-01-01 to 2023-12-31 for NORA3, and the period 2005-01-01 to 2018-12-31 for NEWA. Since the scope of the discussion is to assess relative spatial variability rather than absolute values, and since both periods are long enough to reflect long-term behaviour, the fact that the two datasets don't cover the same period is not considered by C2Wind to deter from the conclusions of this analysis.

Figure 5-2 shows the spatial variation of the long-term mean wind speed from NORA3 at 100 mMSL and NEWA at 150 mMSL, where each subfigure has its own colour scale as indicated at the right, along with arrows indicating the most frequently occurring wind direction. The gradient maps have been obtained by linear interpolation of the selected nodes at a finer resolution of 1 km for display purposes. The figures also highlight the highest value found within each sub-area with an upwards-pointing triangle, the lowest value with a downwards-pointing triangle, and the locations of the 3 FLSs as crosses (see Appendix B for more details on the FLSs).

In general terms, the plots show that both datasets predict similar patterns for both sub-areas of KFII: In the case of KFII North, lower wind speeds on the northwestern part of the sites closer to shore and higher wind speeds on the southeastern part further from shore, and the maximum- and minimum mean wind speed points being located in general in the same part of the sub-areas. In the case of KFII South, lower wind speeds are predicted on the western side of the project sub-area, while the highest wind speeds are predicted to occur at the western part of the project sub-area.

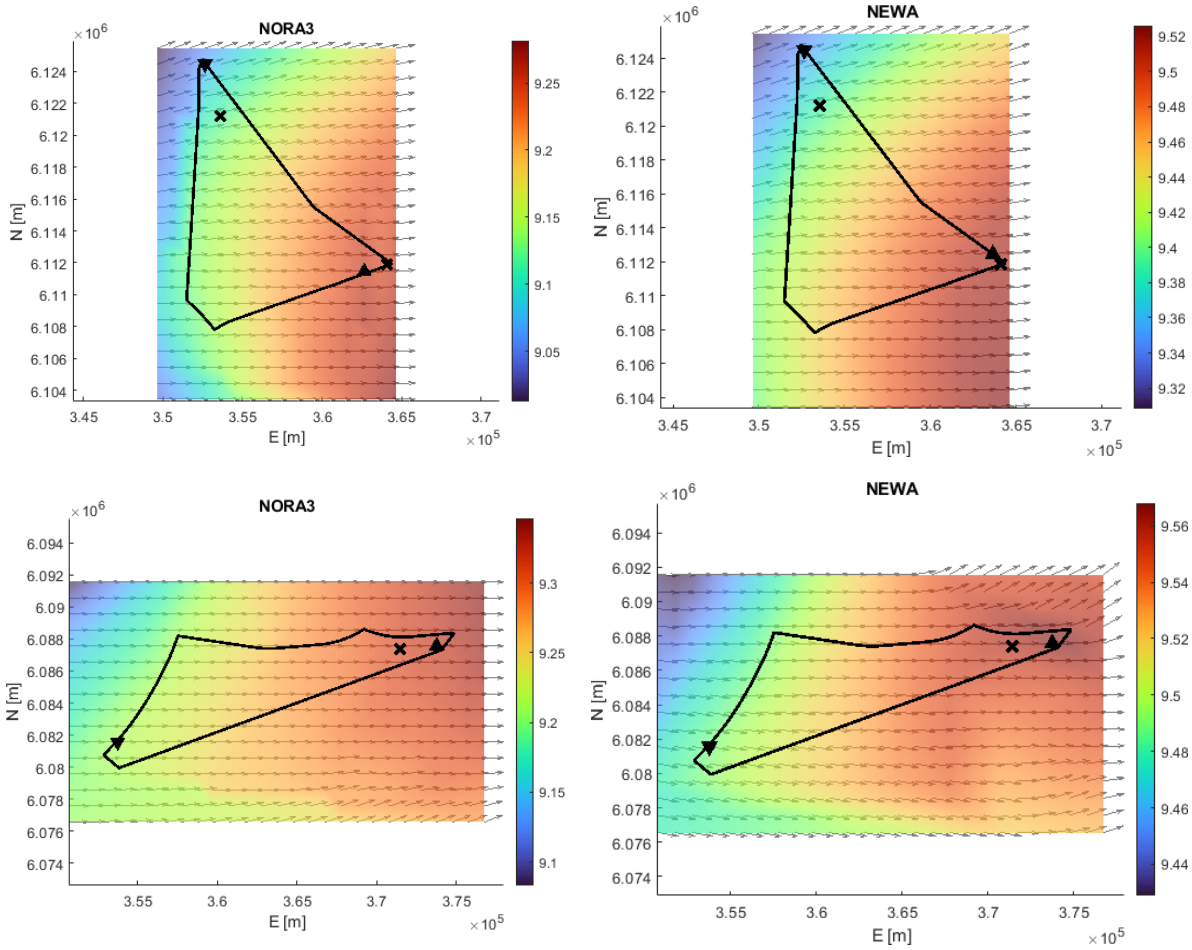

Figure 5-2: Spatial variation of wind speed and wind direction as per the NORA3 (left column) and NEWA (right column) datasets for KFII North (top row) and KFII South (bottom row). Data from the individual nodes has been interpolated throughout the site at a finer resolution for display purposes. The coloured background indicates long-term mean wind speed at 100 mMSL for NORA3 and long-term mean wind speed at 150 mMSL for NEWA, note the different colour scales on the right of each subfigure. The highest value found within each sub-area is marked with an upwards-pointing triangle, the lowest value with a downwards-pointing triangle, and the locations of the 3 FLSs as crosses. The grey arrows on each subfigure show the most frequently occurring wind direction. CRS: WGS84 / UTM Zone 33N.

Figure 5-2 also shows arrows indicating the 10°-wide wind direction bin with the highest population at different locations across the site. For both the NORA3 and NEWA datasets, there is little variability across the two KFII sub-areas, with the most frequent wind direction bin being virtually constant. The apparent variability seen on the eastern part of KFII South predicted by NEWA is produced probably because of the low number of nodes used for that location. For further details, Figure 5-3 and Figure 5-4 show histograms of the wind speed- and direction distributions across both sub-areas of the site and for both datasets, where the histograms show the mean distribution and the mean plus- and minus one standard deviation. Here it is clear that the apparent variability in the most frequent wind direction is simply a reflection of small variability in the individual frequencies for several adjacent wind direction bins, all having significant frequencies. When used in connection with 30°-wind direction bins, as typically done for FEED purposes, the wind direction variability across the site will be of negligible consequence for the results of such studies.

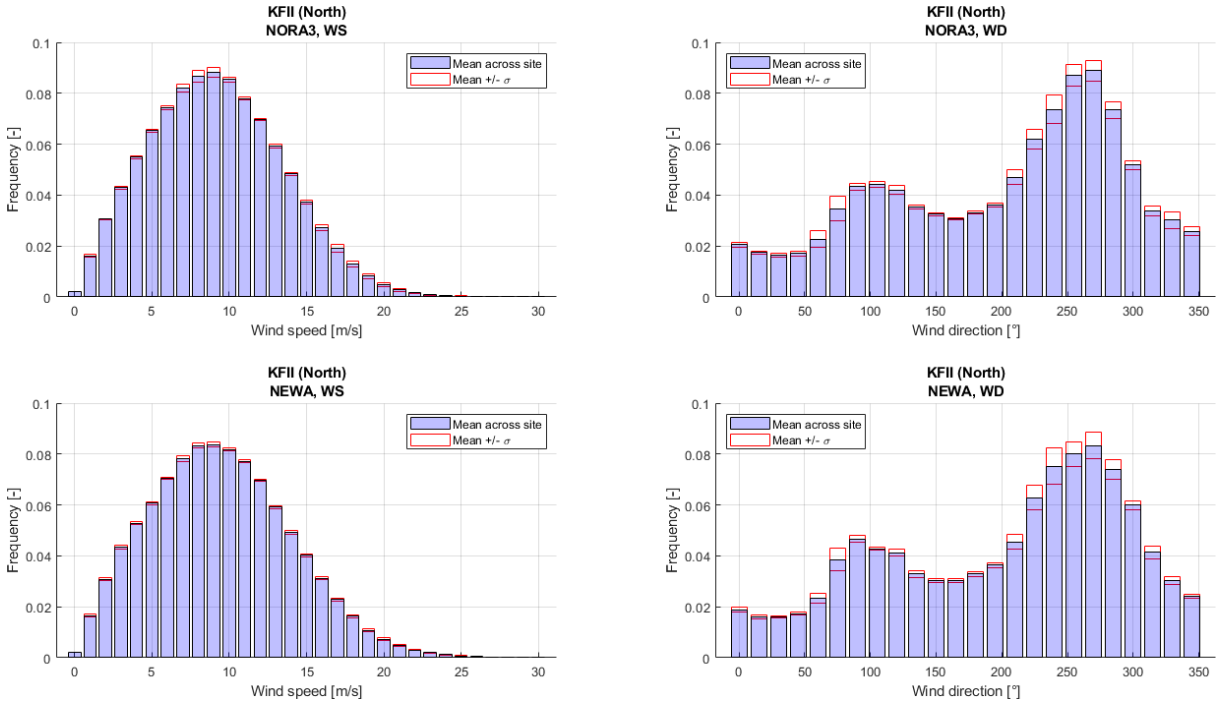

Figure 5-3: For KFII northern sub-area: wind speed (left) and wind direction (right) distributions for the different NORA3 (top) and NEWA (bottom) nodes. The blue bars show the mean frequency at each wind speed- and direction bin, while the red bars show the mean +/- 1 standard deviation.

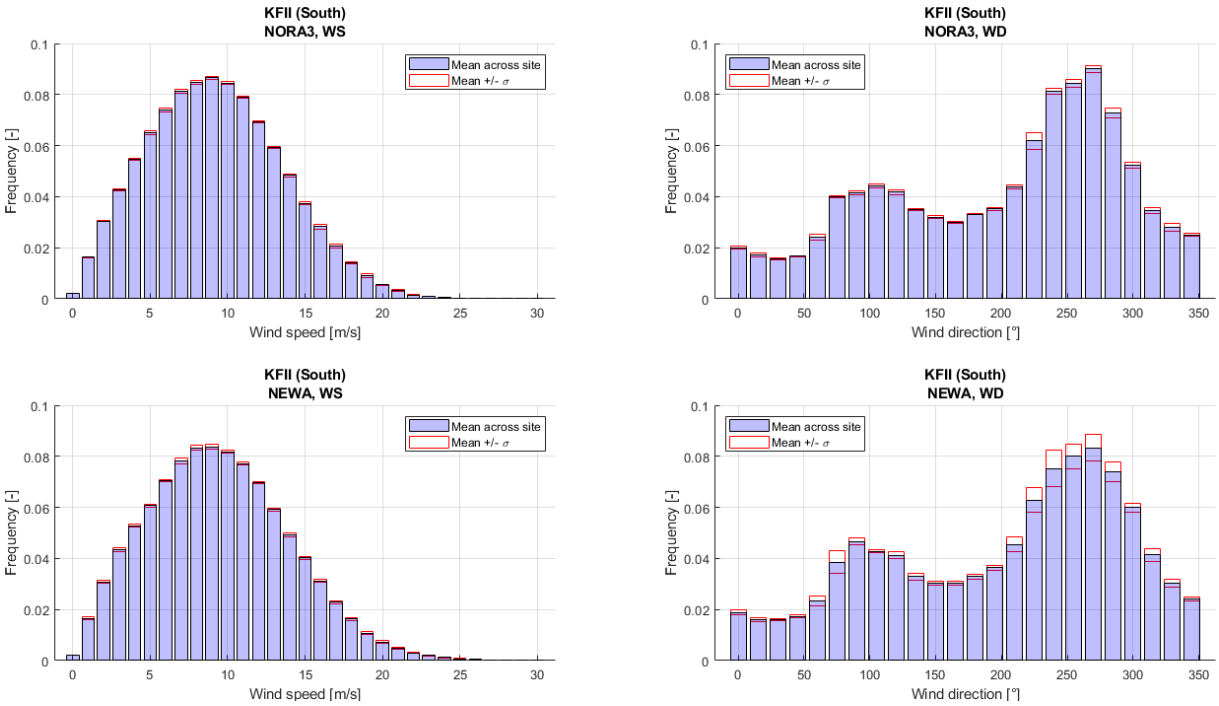

Figure 5-4: For KFII southern sub-area: wind speed (left) and wind direction (right) distributions for the different NORA3 (top) and NEWA (bottom) nodes. The blue bars show the mean frequency at each wind speed- and direction bin, while the red bars show the mean +/- 1 standard deviation.

The selection of representative analysis points needs to also account for the possible variation in extreme wind conditions, mainly extreme wind speed. The GASP dataset has been used to assess the spatial variation of extreme wind conditions here, as shown in Figure 5-5. The figure shows the 10-minute mean wind speed with a 50-year return period at 150 mMSL in the background, along with the minimum- and maximum values in each area subdivision. There is moderate variability within the two sub-areas, but with the maxima being located at a close location to the mean wind speed maxima from NORA3 and NEWA. A summary of the spatial variability of the mean- and extreme wind speeds as per the datasets above is provided in Table 5-1, where the range of values is quantified as the difference between maximum and minimum values in the area divided by the mean value. Both mean wind speed datasets predict very similar degrees of variability, whereas there is more variability in extreme wind speeds.

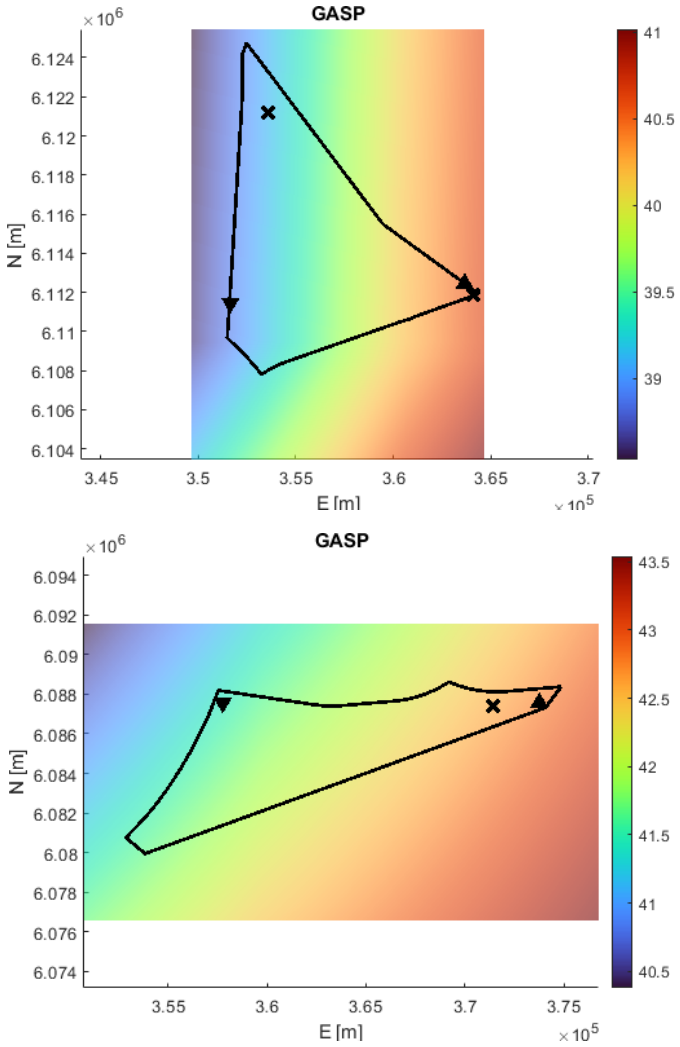

Figure 5-5: Spatial variation of 10-minute wind speed with a 50-year return period at 150 mMSL, from the GASP dataset. The coloured background follows the colour scale on the right. The highest value found within each sub-area is marked with an upwards-pointing triangle, the lowest value with a downwards-pointing triangle, and the locations of the 3 FLSs as crosses. CRS: WGS84 / UTM Zone 33N.

Sub-area	Range = (max – min) / mean		
	NORA3	NEWA	GASP
North	2.1%	1.8%	4.2%
South	1.2%	0.8%	3.2%

Table 5-1: Summary of the variability of mean- and extreme wind speeds across the two site sub-areas. The range metric here is defined as the difference between maximum and minimum values divided by the mean.

Finally, Figure 5-6 shows the locations with the top 25% quantile values for mean wind speed in grey and extreme wind speed in red, the two project sub-areas, along with the grid points that fall in both categories. With these results, the logical consequence of the discussion in this section is to select a representative analysis point out of the subset that is in the top 25% quantile for both metrics for each project sub-area. Given the limited variability within each of the two sub-areas, as summarised in Table 5-1 and the intended use of the conclusions of the present report being FEED of offshore WTGs and support structures, C2Wind considers that a single point is sufficient for the present stage. The coordinates for the selected analysis points are summarised in Table 5-2. As will be further detailed in Sections 8 and Appendix A, the normal wind conditions will be

described by extrapolating the long-term corrected Weibull parameters to the location of the analysis point, whereas the extreme wind speed value of the most severe location within the subdivision will be ascribed to the analysis point. Furthermore, results will also be reported at the locations of the three FLSs within KFII.

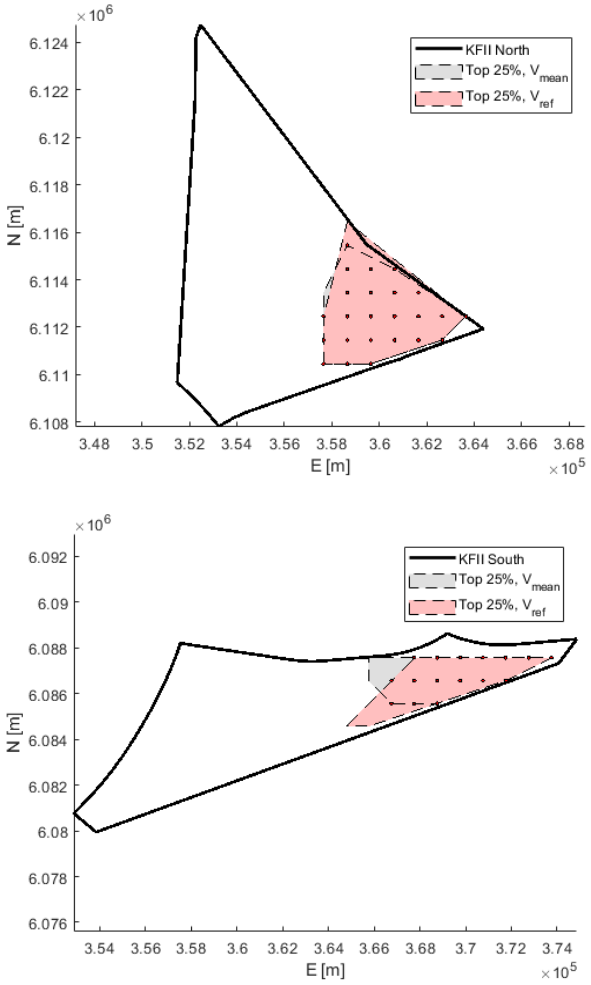

Figure 5-6: KFII sub-areas North and South with the locations of the highest 25% mean wind speed (grey) and extreme wind speed (red). The representative analysis points for each subdivision are defined from the intersection of both areas. CRS: WGS84 / UTM Zone 33N.

Site	Point	Coordinates WGS84 / UTM Zone 33N	
		Easting [m]	Northing [m]
North	P1	362654	6112450
South	P2	373763	6087570

Table 5-2: Location of selected analysis points.

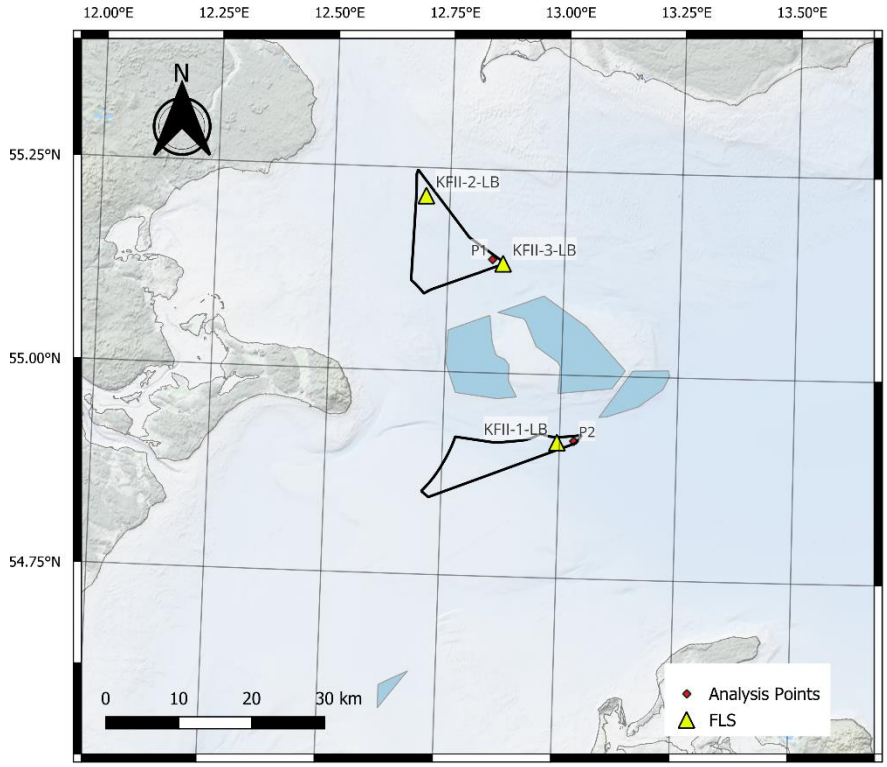

Figure 5-7: Location of analysis points. CRS: WGS84.

6. Normal Wind Conditions

This section describes the free stream wind conditions for normal conditions[5]. The conditions stated here do not cover any effects from neighbouring wind turbine wake.

The shear conditions are characterised using the KFII FLS data, supplemented by the EIBS FLSs and Vortex series to discuss the impact of the short measurement campaign. The turbulence intensity conditions are characterised using the FINO2 met mast data and additional analysis of directional turbulence as measured by the FLSs, as well as the IJmuiden met mast data for supporting discussions in Appendix C.

6.1 Normal conditions wind Weibull distributions and wind roses

The omnidirectional wind speed distribution Weibull parameters at hub height have been derived in Appendix A for the analysis points found in Section 5. The analysis in Appendix A consisted of long-term correction of the measurements with an MCP approach, followed by spatial extrapolation to the analysis points. The Weibull parameters describing the wind speed distribution at the analysis points are summarised in Table 6-1, while the wind rose applicable to all points is shown in Figure 6-1.

Site	Point	A	k	Mean wind speed
		[m/s]	[-]	[m/s]
KFII North	P1	11.13	2.199	9.89
KFII South	P2	11.01	2.173	9.79
KFII-1-LB		10.99	2.173	9.73
KFII-2-LB		10.93	2.199	9.68

Table 6-1: Weibull parameters estimated at the analysis points and FLS locations at hub height. The mean wind speed is calculated from the fitted Weibull parameters.

[5] Please note that the definition of “Normal conditions” in Section 6.3.1 of [IEC6131] is somewhat less specific than that of Section 6.3 of [IEC613]: the latter states that normal conditions occur “more frequently than once per year”, while the former states they occur “frequently during normal operation”. In this report, the definition from [IEC613] has been used.

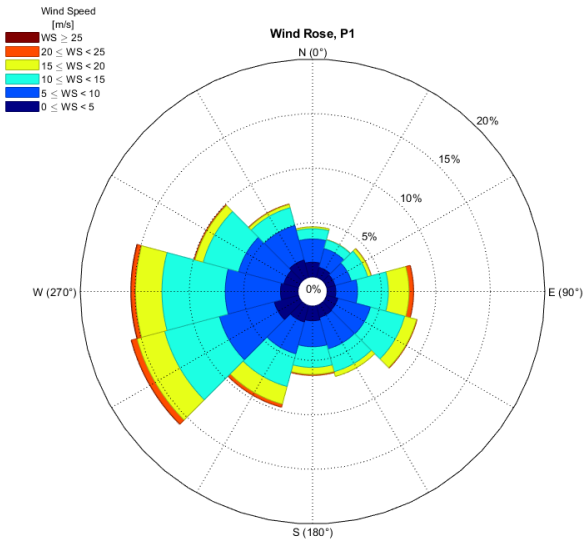

Figure 6-1: Wind rose corresponding to the long-term wind distribution at point P1, applicable to all analysis points.

For use in Fatigue Limit State (FLS) Design Load Cases (DLCs) in Integrated Load Analysis, particularly those involving Normal Sea States (NSS), joint directional occurrence frequencies for the wind speed and (Wind-Sea) wave directions are needed. These are unambiguously provided through the misalignment tables in a Marine Assessment.

For some purposes, e.g. calculation of Wind Farm Turbulence, it is necessary to use directional occurrence frequencies of wind speeds. These can be found by summing over (Wind-Sea) wave directions in the aforementioned misalignment tables provided in the project's Marine Assessment. Alternatively, and requiring that the user first justifies its applicability for that purpose, the Marine Assessment provides directional Weibull fits that can be used for input to Wind Farm Turbulence analyses.

6.2 Wind shear and wind shear profile for normal conditions

In this document, the wind shear will be modelled as:

$$WS(h) = WS(h_{Ref})\left(\frac{h}{h_{Ref}}\right)^{\alpha} \qquad \text{Eq. 6-1}$$

where:

h_{Ref}	is the reference height
h	is the height of the needed wind speed,
α	is the wind shear exponent.

In the two Sections 6.2.1 and 6.2.2, this wind shear description is used for two different purposes:

- In Section 6.2.1, the focus is on normal conditions wind speed extrapolation over a small elevation difference; for example, extrapolating a few tens of metres beyond the ±5 m elevation interval around h_{Hub} for which the present report's ILA-values need not be changed. For this purpose, and to make the most accurate mean wind shear description for such elevations, the wind shear exponent is

calculated by fitting a power law across a FLS measurement elevations between 40 and 300 mMSL, and for all model elevations between 50 and 300 mMSL for the mesoscale data, and taking the mean value.

- In Section 6.2.2, the focus is on the derivation of the Normal Wind Profile (NWP), wherefore the wind shear exponent is calculated by fitting a power law to wind speeds vs. elevation across the same range of elevations, but the mean absolute wind shear is used instead of the simple mean.

Ideally, on-site measurements would provide the best data source for prescribing wind shear values. Due to the short duration of the measurement campaign, which as of writing this document has collected less than a full year of data, additional analysis is required to ensure that no seasonal bias is introduced into the estimates. Figure 6-2 shows mean wind speed profiles and fitted shear exponents to the 2 main KFII FLSs, their co-located Vortex model time series, and the 2 EIBS FLSs. For the Vortex and EIBS4 FLS datasets, two versions are presented: one corresponding to their full dataset (indicated by the legend suffix "*Full*"), and one corresponding only to timestamps concurrent with the KFII FLS measurements (indicated by the legend suffix "*Conc*"). The plot shows the following:

- All datasets find similar wind shear exponent values and similar shapes of the wind profile.
- The two KFII FLSs conclude very similar values of the wind shear exponent, ranging between 0.079 and 0.089.
- For the co-located Vortex time series, the wind shear exponent fitted to the long-term time series is always a lower value than that fitted to the concurrent period only.
- The Vortex series underestimates the mean wind speed and overestimates the wind shear exponent when compared to the KFII FLSs over their concurrent period.

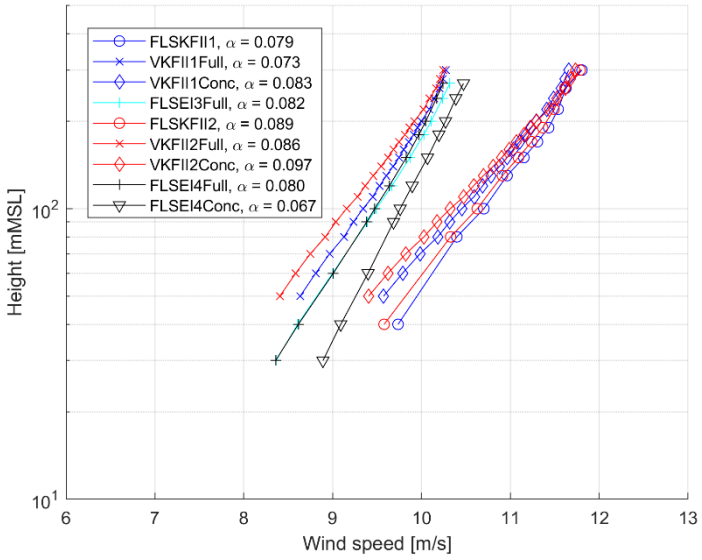

Figure 6-2: Mean wind speed profiles and fitted shear exponents to the 2 main KFII FLSs, their co-located Vortex model time series, and the 2 EIBS FLSs.

From the observations above, the KFII FLS measurements can be used to characterize wind shear at the site despite their shorter duration.

6.2.1 Normal conditions wind climate scaling

The time series of fitted wind shear exponent for each time stamp across measurement elevations between 40 and 300 mMSL has been used for deriving the shear exponent in this section. The mean shear exponent values for the two main FLSs were compared and the largest of them, found for KFII-2-LB in Table 6-2, is chosen to characterize wind shear conditions at the KFII site. On this basis, normal conditions wind speeds shall, for all wind directions, be transformed to other heights using a shear exponent of 0.09.

$$WS(h) = WS_{Hub}\left(\frac{h}{h_{Hub}}\right)^{0.09} \qquad \text{Eq. 6-2}$$

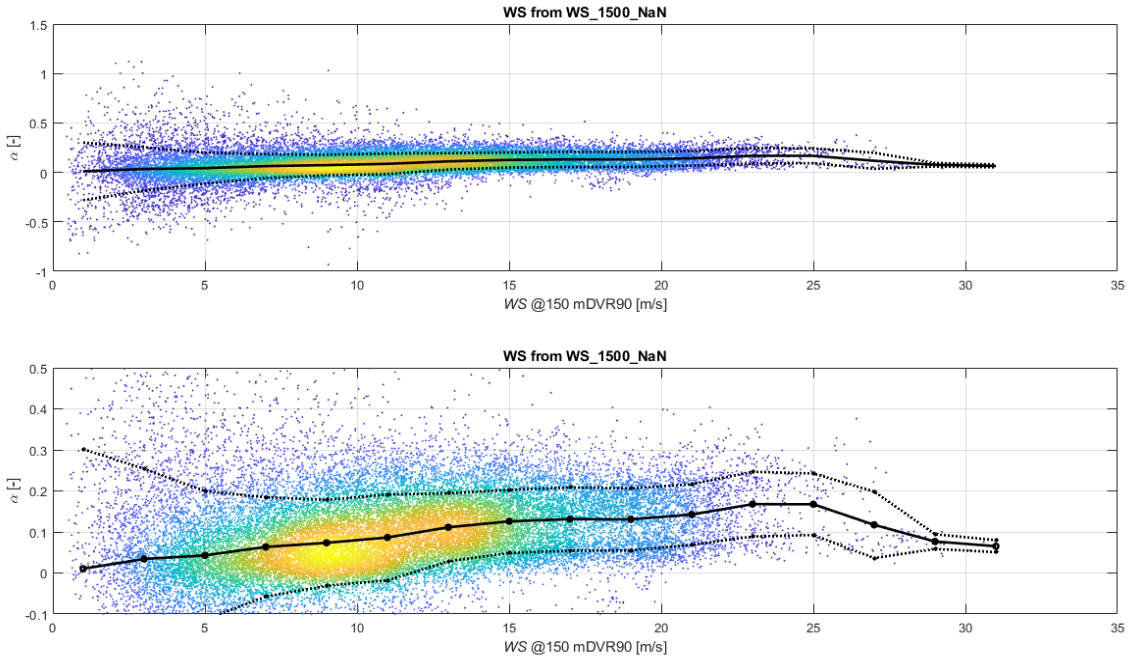

Figure 6-3: Scatter plots of wind shear exponents vs. hub height wind speed, obtained from the hub height sensor at the KFII2 FLS and fitting the wind profile across all elevations covering the rotor plane and up to 300 mMSL as listed in Section 6.2. The plots show the points coloured according to density. The upper plot shows all data, whereas the lower plot shows details for the most widespread values. The black points, joined by the fully drawn black line, show the mean-of-monthly means wind-speed binned mean values. The markers joined by dashed lines show the mean values described in the preceding sentence, plus and minus one mean-of-monthly-means wind speed binned standard deviation.

Wind Direction [°N]															
***WS* bin**		**Min**	-15	15	45	75	105	135	165	195	225	255	285	315	
[m/s]		**Max**	15	45	75	105	135	165	195	225	255	285	315	345	**Omni**
≤	**<**	**Centre**	**0**	**30**	**60**	**90**	**120**	**150**	**180**	**210**	**240**	**270**	**300**	**330**	
0	2	**1**	-0.040	-0.063	-0.028	0.053	0.090	0.022	0.046	-0.058	0.016	0.013	-0.122	0.085	0.010
2	4	**3**	0.103	-0.039	0.028	0.073	-0.021	0.043	-0.021	0.010	0.042	0.125	0.067	0.084	0.034
4	6	**5**	0.065	-0.009	0.003	0.044	0.016	-0.031	0.012	0.046	0.087	0.119	0.054	0.053	0.043
6	8	**7**	0.067	0.040	0.006	0.018	0.024	0.047	0.083	0.099	0.091	0.082	0.062	0.077	0.064
8	10	**9**	0.049	0.008	0.020	0.040	0.021	0.092	0.078	0.102	0.128	0.107	0.080	0.042	0.073
10	12	**11**	0.070	-0.003	0.022	0.018	-0.015	0.088	0.121	0.136	0.147	0.120	0.102	0.067	0.087
12	14	**13**	0.053	-0.021	0.067	0.051	0.036	0.094	0.149	0.128	0.154	0.122	0.112	0.086	0.111
14	16	**15**	0.060	-	0.074	0.077	0.070	0.112	0.159	0.160	0.165	0.132	0.110	0.092	0.126
16	18	**17**	-	-	0.139	0.073	0.138	0.124	0.171	0.167	0.181	0.146	0.097	0.067	0.131
18	20	**19**	-	-	0.108	0.059	0.137	0.185	0.169	0.162	0.197	0.149	0.117	0.071	0.131
20	22	**21**	-	-	0.125	0.106	0.052	-	0.193	0.128	0.196	0.178	0.114	-	0.142
22	24	**23**	-	-	0.070	0.157	-	-	0.200	0.180	0.218	0.203	0.112	-	0.168
24	26	**25**	-	-	0.030	0.120	-	-	0.171	0.209	0.206	0.221	0.096	-	0.167
26	28	**27**	-	-	0.066	0.072	-	-	-	0.233	0.222	0.164	0.320	-	0.117
28	30	**29**	-	-	-	0.077	-	-	-	-	-	-	-	-	0.077
30	32	**31**	-	-	-	0.065	-	-	-	-	-	-	-	-	0.065
Mean over WS:			**0.064**	**-0.001**	**0.035**	**0.062**	**0.028**	**0.067**	**0.089**	**0.110**	**0.139**	**0.130**	**0.089**	**0.066**	**0.089**

Table 6-2: Mean shear exponent measured at KFII-2-LB, binned as a function of wind speed and wind direction.

6.2.2 Wind shear exponent to use in load calculations requiring Normal Wind Profile

For modelling the shear across the wind turbine rotor, a different approach to that of Section 6.2.1 is needed. In particular, it could be inaccurate to average positive and negative values of the shear, since both large positive and large negative shear values could yield larger loads, despite their mean being numerically small.

Therefore, to find a fair value of the shear exponent to use to model the shear across the wind turbine rotor in Integrated Load Analyses, the analysis leading to Figure 6-3 was repeated, now including the mean of the absolute values of the shear exponents (i.e. treating negative shear exponents as if they were positive shear exponents of the same numerical magnitude). The results for KFII-2-LB, which yields the highest resulting value, together with wind-speed binned standard deviations, are tabulated in Table 6-3.

WS bin [m/s]		# 10-min samples [-]	Mean shear exponent [-]	Std. dev. of shear exponent [-]	Mean absolute shear exponent [-]	Std. dev. of absolute shear exponent [-]
≤	<					
0	2	396	0.010	0.291	0.215	0.197
2	4	1936	0.034	0.220	0.152	0.162
4	6	3123	0.043	0.157	0.109	0.120
6	8	3560	0.064	0.121	0.093	0.100
8	10	4461	0.073	0.105	0.092	0.089
10	12	4238	0.087	0.105	0.106	0.085
12	14	3798	0.111	0.083	0.119	0.072
14	16	2916	0.126	0.077	0.127	0.075
16	18	2129	0.131	0.077	0.133	0.073
18	20	1724	0.131	0.076	0.134	0.070
20	22	1106	0.142	0.074	0.142	0.074
22	24	365	0.168	0.079	0.168	0.079
24	26	97	0.167	0.075	0.167	0.075
26	28	56	0.117	0.081	0.117	0.081
28	30	18	0.077	0.018	0.077	0.018
30	32	2	0.065	0.015	0.065	0.015

Table 6-3: Statistical shear exponent values to use as input for the selection of shear exponent to use for deriving the Normal Wind Profile (NWP); i.e. for use in the Integrated Load Analyses that require this wind profile type. The values shaded with light blue are the ones that Section 12.3 in [IEC6131] requires are used to evaluate the shear exponent to be used for Integrated Load Analysis with NWP for an IEC Class I site (0.2-0.4·V_{Ref}); as noted in the text above, this is in line with the suggestions in Section 6.4.3.1 of [IEC6131]. The values for the largest WS_{Hub}-bins have their values listed in grey text to highlight that they are found using only a few data points.

Please note that in the earlier Ed. 3.0 of [IEC611], this wind speed interval to be considered for characterising the shear exponent corresponded to 0.2 to 0.4·V_{ref}, using the terminology in Section 11.3 of Ed. 3.0 of [IEC611]. In contrast, Section 11.3.2 of the newer Ed. 4.0 of [IEC611] implies that the mean shear exponent may be used except for certain areas in connection with highly stratified flow, complex terrain, or severe roughness changes. However, Ed. 4.0 of [IEC611] does not give any guidance on the wind speed range to use for this evaluation. Therefore, the guidance from Section 11.3 of Ed. 3.0 of [IEC611] is maintained in the present document. This is also in line with the suggestions of the (currently valid) Section 6.4.3.1 of [IEC6131] (and Section 12.3 of its earlier edition).

The wind shear exponent for the NWP is found as the (unweighted) mean of the values in the cells shaded light blue in Table 6-3 to 0.110:

$$WS_{NWP}(z) = WS_{NWP,Hub}\left(\frac{z}{h_{Hub}}\right)^{0.124} \qquad \text{Eq. 6-3}$$

Here, z and h_{Hub} are measured in metres above Mean Sea Level (MSL), i.e. mMSL.

This value of 0.124 is larger than the mean value from Table 6-2, but smaller than the mean value for some individual wind directional bins such as [225; 285[°N. This is acceptable since these mean shear values remain smaller than the value of 0.2 used for RNA type certification.

6.3 Free Stream Turbulence Intensity

Appendix C provides an analysis and discussion of free stream turbulence intensity conditions for offshore sites, based on measurements from a series of publicly available offshore met mast datasets. While the discussion in Appendix C is of a general character for sites far enough from shore that coastal effects can be considered negligible, the measurement datasets at KFII can be used to establish whether any effects from nearby land or existing offshore wind farms are present in the measurements, and thus should be accounted for. While turbulence intensity as measured by Lidars and floating Lidars is not directly applicable in a quantitative manner for WTG design purposes, the directional dependence of Lidar measured turbulences at the 3 KFII FLSs can be used to qualitatively support the discussion of whether the site suffers from any land- or wake-added turbulence.

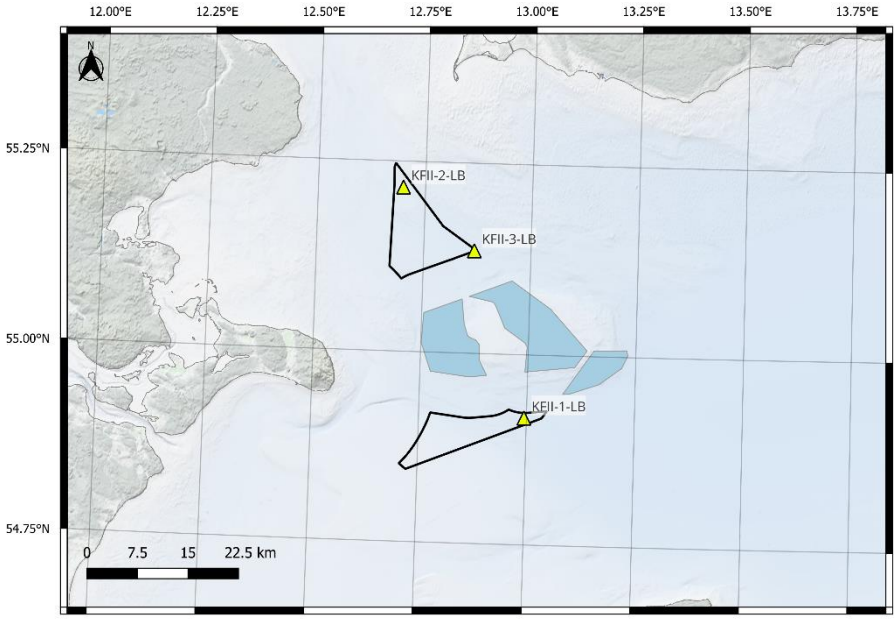

Figure 6-4: Location of the three KFII FLSs as well as nearby land and OWFs in operation (blue polygons). CRS: WGS84.

Figure 6-4 shows the site boundaries, and the locations of the three KFII FLSs, along with the locations of the nearby Kriegers Flak I and Baltic 2 OWFs. The wind directions in which these OWFs are upwind from each FLS have been determined, as well as directions in which there is land less than 30 km upstream. Figure 6-5 shows a scatter plot of FLS-measured turbulence intensity as a function of wind direction, highlighting the wind direction sectors in which the upstream distance to land is less than 30 km in grey and the sectors with neighbouring OWFs in red. OWFs such as Baltic 1 and Lillgrund are excluded from this analysis as they are over 50 km away from the nearest FLS. While the absolute values found in this plot are likely biased compared to cup anemometer measurements applicable for deriving an NTM, their directional dependence is useful in assessing whether the FLSs see differences in the incoming flow that can be clearly attributable to land or neighbouring OWFs.

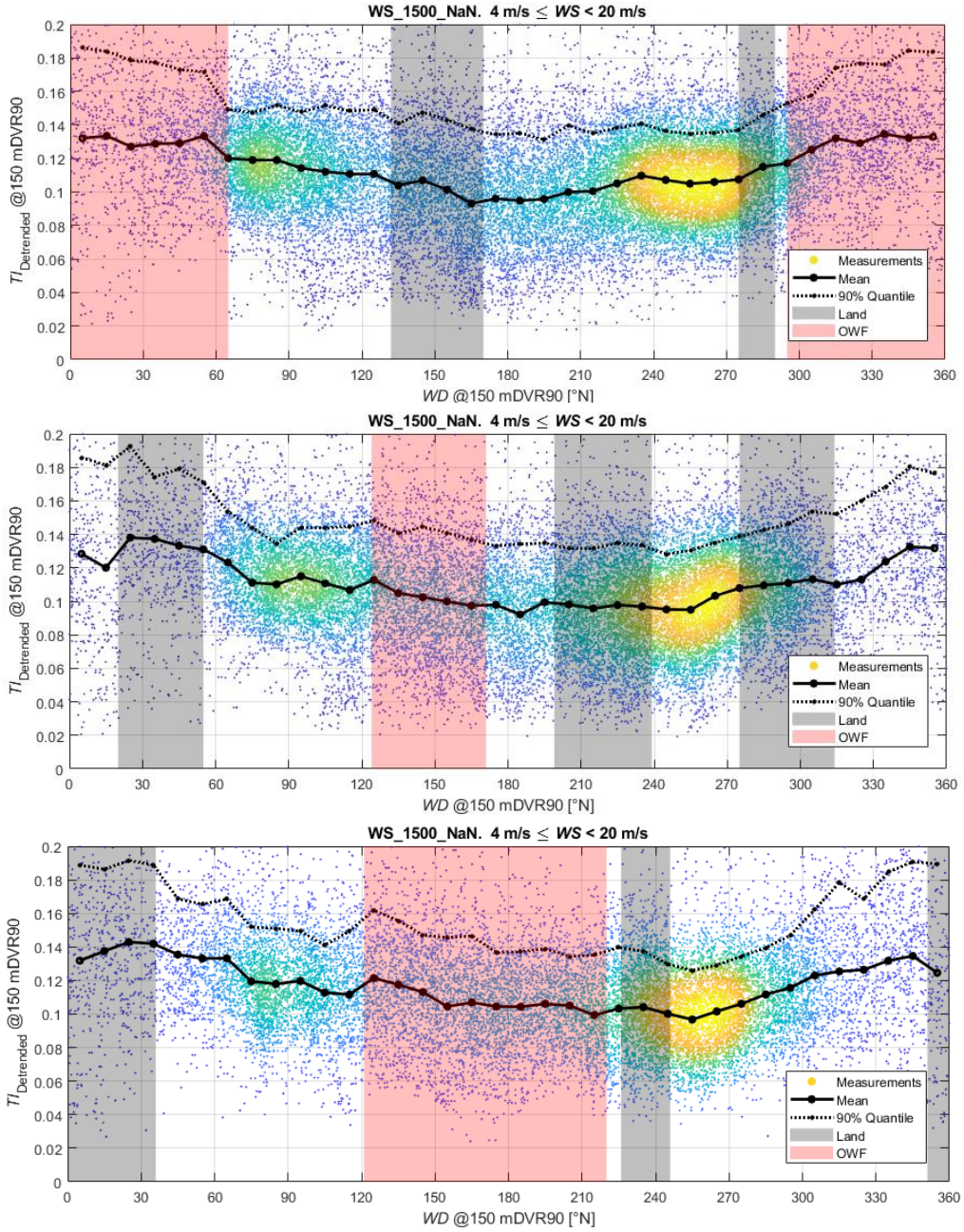

Figure 6-5: FLS-measured *TI* at 150 mMSL as a function of wind direction at 150 mMSL for FLSs KFII1 (top), KFII2 (middle) and KFII3 (bottom). Binned mean values are plotted with a solid black and the 90% quantiles are plotted with a dotted black line. The grey areas indicate wind directions where the wind comes from land, while the red areas indicate directions where there is an operational OWF upstream.

The plots in Figure 6-5 show no conclusive signs of any impact of neighbouring OWFs or land on the Lidar-measured *TI* at 150 mMSL, that is, the three datasets are seen to have the same *TI* trends in the approximate wind direction range [75; 300]°, despite having very different upstream features regarding both neighbouring OWFs and land. While the slight differences in the wind direction range [320; 60]° could seem to indicate a sector of higher turbulence for onshore directions at FLSs 2 & 3, closer inspection reveals this is not the case. The reason for the differences in the wind direction range [320; 60]° and the higher variance – as seen by the gap between the 50- and 90-percent quantile lines in all three subplots – in those directions is likely the small number of datapoints in those directions, as seen in Figure 6-6, where the plots from Figure 6-5 have been reproduced

now removing the point clouds and adding histograms to indicate the amount of data points in each directional bin. The differences and higher variance in the wind direction range [320; 60]° are more likely caused by the low number of data points rather than upstream onshore conditions. Furthermore, the fact that no clear impact of neighbouring OWF wake is visible is expected, since the measurement height at 150 mMSL is much higher than the hub height at the OWFs (between 80 m and 110 m), and since the nearest possible WTG in each OWF is at least 7 km away from any given FLS – equivalent to between 42 and 58 rotor diameters for the WTGs with 167 m and 120 m rotor diameters installed at these parks.

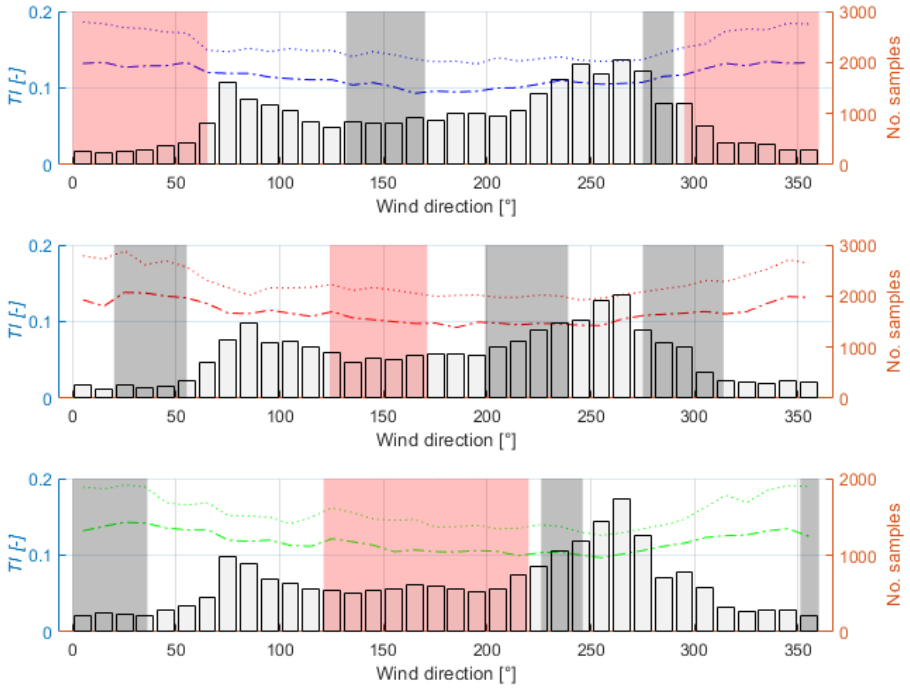

Figure 6-6: Reproduction of the plots from Figure 6-5, removing the point clouds and adding histograms to indicate the amount of data points in each directional bin example.

Thus, after the discussion at the start of this section, the turbulence intensity is treated omnidirectionally in the present document. Furthermore, it is characterized using measurements from the top-mounted and mast-corrected anemometer at the nearby FINO2 met mast described in Appendix B.3, corrected for mast effects, and following the analyses in Appendix C, it is supplemented using measurements from the top-mounted cup anemometers at the IJmuiden met mast, extrapolated to hub height by the measured wind shear from its co-located Lidar.

6.3.1 Normal Turbulence Model and turbulence statistics

In the present section, the Normal Turbulence Model (NTM) and associated statistics are calculated from the FINO2 met mast measurements. While 0 presents and validates a model for offshore turbulence which can be adjusted for atmospheric stability, the FINO2 met mast is so close to the KFII site that its data can be used to accurately describe the turbulence conditions at the site.

As described in Appendix B.3 and shown in Figure B-12 and Figure B-13, the FINO2 dataset needs to be trimmed down to exclude measurements after the start of

operations of the nearby OWF, and wind directions for which the *TI* from the top anemometer is affected by the lightning rod need to be filtered out. After these filtering steps and using only the mast-corrected signals labelled "*MC*" in the dataset, mean wind speeds measured at 102 mMSL at the FINO2 met mast were extrapolated to 150 mDVR90 using the instantaneous measured wind shear exponent fitted to the anemometers at 72, 82 & 92 mMSL, to create the sensor *WS_1500_Hub*. The cup-measured wind speed standard deviation at 102 mMSL was used directly for calculating *TI* at hub height. As per Figures 4.11 and 4.17 of [POLLAK], the wind speed variance is either constant for low wind speeds or decreases with elevation for high wind speeds. Assuming a constant wind speed variance when extrapolating to hub height therefore results in conservatively high *TI*-values.

In Figure 6-7, a scatter plot of *TI* vs. *WS* at 150 mMSL is shown, and *WS*-binned mean values (μ), standard deviation values (σ), and 90%-quantile values (P_{90}) of *TI* are shown; all calculated by using the method of mean-of-monthly-means. In accordance with Section 6.3.1.3 of [IEC611], the NTM values will be set to be the P_{90}-values. One complication of this is that there are too few data points for $WS \geq 31$ m/s to reliably estimate P_{90}, which can be seen in the histogram in the bottom half of Figure 6-7. As a precautionary and conservative measure, the NTM-values, as well as their accompanying statistical values, will be moderately increased compared to the measurements for $WS \geq 30.5$ m/s, as indicated by the black diamonds joined by dashed black lines in the top half of Figure 6-7. Following this procedure, the NTM-values and accompanying statistics are provided in Table 6-4. It is noted that the *TI* mean- and standard deviation values are reasonable and completely in line with values seen from other offshore projects. A comparison can be made with the turbulence intensity statistics from other offshore sites – e.g. Sections 4.1.4 and 4.1.5 of [POLLAK] from where close to identical *TI* values can be found.

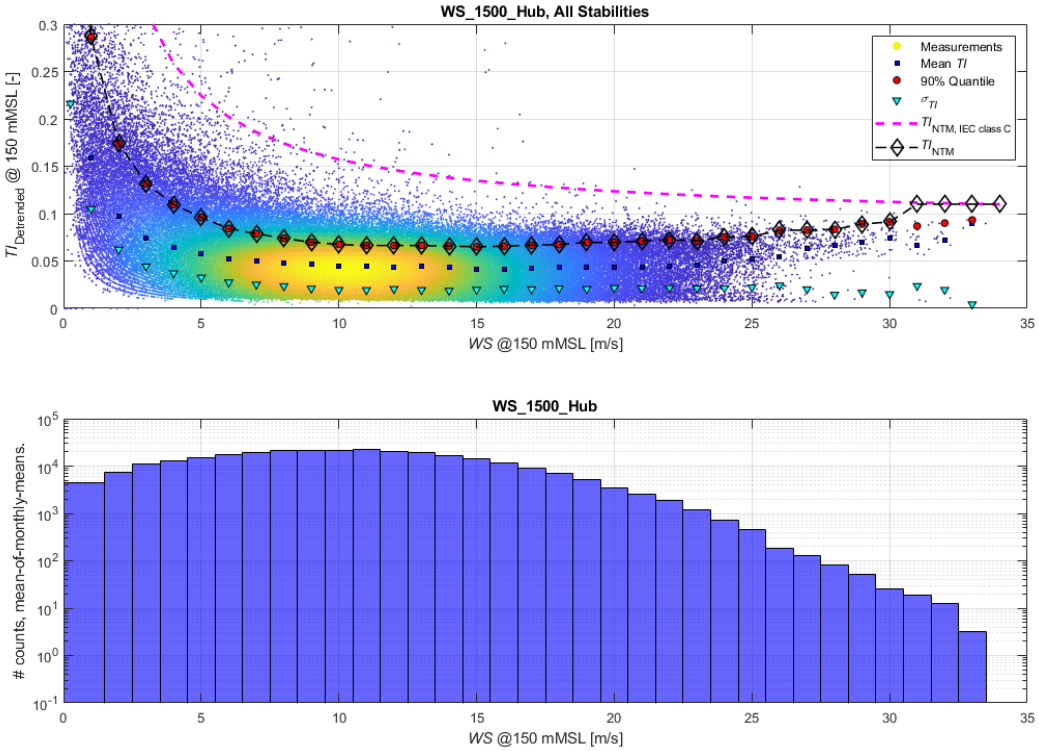

Figure 6-7: The top figure shows a density-scatter plot of detrended *TI* vs. *WS* @150.0 mMSL. The *WS*-binned mean values are shown with blue squares, the standard deviation values with cyan inverted triangles, and P_{90}-values with red dots. All these are calculated by the method of mean-of-monthly-means. The black diamonds joined by the dashed black line show the NTM-values chosen for use in the Integrated Load Analyses requiring this turbulence type. The bottom plot shows a *WS* occurrence frequency histogram, where the 2nd axis is logarithmic. As seen by comparing the upper and lower figures, the NTM values are chosen to equal the P_{90}-values for *WS*-values where there are a sufficient number of data points in each bin, and conservative upper estimates are made for bins that have fewer data points.

Free Turbulence Intensity @150.0 mDVR90 statistics and TI_{NTM}							
***WS* bin**			***TI* statistics**				
[m/s]			μ	σ	P_{90}		TI_{NTM}
≤	<	Centre	[-]	[-]	[-]		[-]
0.5	1.5	1	0.158	0.105	0.287		0.287
1.5	2.5	2	0.098	0.062	0.174		0.174
2.5	3.5	3	0.074	0.044	0.132		0.132
3.5	4.5	4	0.064	0.037	0.110		0.110
4.5	5.5	5	0.058	0.033	0.096		0.096
5.5	6.5	6	0.052	0.027	0.084		0.084
6.5	7.5	7	0.050	0.025	0.079		0.079
7.5	8.5	8	0.048	0.024	0.074		0.074
8.5	9.5	9	0.046	0.021	0.070		0.070
9.5	10.5	10	0.045	0.019	0.068		0.068
10.5	11.5	11	0.044	0.019	0.066		0.066
11.5	12.5	12	0.044	0.020	0.066		0.066
12.5	13.5	13	0.044	0.019	0.066		0.066
13.5	14.5	14	0.043	0.019	0.066		0.066
14.5	15.5	15	0.041	0.020	0.065		0.065
15.5	16.5	16	0.041	0.021	0.066		0.066
16.5	17.5	17	0.042	0.020	0.067		0.067
17.5	18.5	18	0.043	0.021	0.067		0.067
18.5	19.5	19	0.043	0.020	0.070		0.070
19.5	20.5	20	0.043	0.022	0.070		0.070
20.5	21.5	21	0.044	0.021	0.071		0.071
21.5	22.5	22	0.044	0.022	0.072		0.072
22.5	23.5	23	0.046	0.021	0.071		0.071
23.5	24.5	24	0.050	0.021	0.075		0.075
24.5	25.5	25	0.052	0.022	0.076		0.076
25.5	26.5	26	0.054	0.024	0.082		0.082
26.5	27.5	27	0.063	0.020	0.083		0.083
27.5	28.5	28	0.067	0.014	0.083		0.083
28.5	29.5	29	0.070	0.017	0.089		0.089
29.5	30.5	30	0.074	0.015	0.091		0.091
30.5	31.5	31	0.066	0.024	0.087		**0.110**
31.5	32.5	32	0.072	0.020	0.090		**0.110**
32.5	33.5	33	0.089	0.004	0.093		**0.110**

Table 6-4: Free turbulence intensity statistics and TI_{NTM} @150.0 mMSL to be used in Integrated Load Analyses requiring the use of NTM. All *TI* statistics values in non-bold are taken from the statistics shown in Figure 6-7. The *TI* statistics values in bold text are assigned to conform with the assignment of TI_{NTM} in Figure 6-7. Should values for $WS \geq 33.5$ m/s be needed, the *TI* value for $WS = 33$ m/s can be used.

6.3.2 IFORM analysis and discussion of ETM

As stated in Appendix C, the turbulence model presented therein does not account for the stochasticity of the wind field. Similarly, the 10-minute measurements in the FINO2 dataset do not allow for a detailed assessment of extreme turbulence, which would require high-frequency data. Instead, the present section will prescribe an ETM for the KFII site based on the literature.

Figure 2 of [HNSDTR19] shows a considerable number of events seemingly exceeding the IEC Classes IC and IB Extreme Turbulence Model (ETM) thresholds over a duration of 10 years at the Høvsøre met mast in the Danish west coast. The same document discusses that these events are likely not representative of extreme microscale turbulence

(characterised by either the Mann- or Kaimal spectra in Annex C of [IEC611]), but instead originate from mesoscale flow features (fronts, mostly, but also convective structures).

In essence, the difficulty of distinguishing microscale turbulence from mesoscale flow features lies in the use of 10-minute statistics data: For each sample, having only the 10-minute mean- and standard deviation values does not allow discriminating between turbulence features (expressed in terms of eddies of frequencies f) which belong to the microscale inertial subrange (approximately defined as f > 1/300 Hz), and the smaller-frequency features which belong to the low-frequency part of the microscale spectra, i.e. the gap region and the mesoscale spectra (see Figure 3 of [LARSÉN18] for an illustration of these regions, as well as the discussion in Section 1 of [KANG16]). These mesoscale features are also present at other sites across Northern Europe (Høvsøre and Horns Rev, see Section 4 of [LARSÉN16], and at Østerild, see Section 3 of [LARSÉN18]), and up to 241 mASL (at Østerild in Figure 3 of ibid.). The spectral gap, and its corresponding (added) variance noticeable on the 10-minute standard deviation values, is thereby also likely present at the KFII project area.

C2Wind has replicated the findings from [HNSDTR19] using the IJmuiden met mast data (this analysis is not shown in the present report), and there too, large microscale (small mesoscale) features, are responsible for seemingly large standard deviation values which exceed the IEC Class IC ETM threshold. The expression “seemingly large” is used here to underline that these values are real, but cannot readily be compared with the type of flow conditions prescribed for WTG design in [IEC611] (statistically stationary 10-minute time series generated using modified[6] Kaimal spectra, that is: a microscale spectrum which does not include such mesoscale features). As stated at the start of this subsection, such analysis is not possible with the 10-minute measurements at FINO2.

Regarding the Ultimate Limit State (ULS) load effects on the WTGs of the KFII sites, it is helpful to compare with the results of Section 5 and its subsections of [HNSDTR19]. In particular, Figure 9 and Table 3, both from ibid., show that the ULS load effects from DLC 1.3 using an IEC Class IC ETM are larger, in the absolute sense, than those of the constrained simulations therein, where these constrained simulations model the original (i.e. not high-pass filtered) measurement time series[7]. Due to the similarity of the DTU 10 MW reference WTG model used in [HNSDTR19] (see its Section 1) to modern large WTG types relevant for KFII, and due to the considerably larger values in Table 3 of ibid. of the DLC 1.3 load effects, obtained by using an IEC Class IC ETM, than the load effects

[6] Compared to its original formulation in [KAIMAL72].

[7] In more detail, Section 5.2, particularly Figure 9 and Table 3, both of [HNSDTR19], show that the IEC Class IC ETM yields larger maximum absolute load effects than those of the constrained simulations, when this maximum is taken over all wind speed bins. This is furthermore true for most wind speed bins individually, with very few exceptions. In all cases, as stated in the first sentence of this footnote, the load effects from these exceptional wind speed bins are always exceeded, in the absolute sense, by load effects from other wind speed bins. Moreover, although not the focus of [HNSDTR19], several of the load effects of both IEC Class IC ETM- and constrained simulations for the support structure would be exceeded by load effects from other ULS DLCs. This is particularly true for the tower bottom fore-aft moment, shown in Figure 9c of ibid., which is the DLC where the IEC Class IC ETM has the smallest margin to the constrained simulation: For this structural elevation, gust DLCs almost invariably yield larger load effects, and if the WTG had been an offshore type, extreme wave loads in DLCs 6.1 and 6.2 could yield even larger load effects further down in the structure.

from the constrained simulations, the present report concludes that an IEC Class IB ETM can be used for the KFII sites and that further investigation with high-frequency data may allow reduction of this envelope to an IEC Class IC ETM.

Thus, for Integrated Load Analysis using TI_{ETM}:

The largest of the $TI_{ETM}(WS)$ from Table 6-5 and $TI_{Centre\text{-}Wake}(WS)$ shall be used.

ETM Turbulence Intensity @150.0 mDVR90			
WS bin			
[m/s]			TI_{ETM}
≤	<	Centre	[-]
0	1.5	0.75	2.954
1.5	2.5	2	1.158
2.5	3.5	3	0.799
3.5	4.5	4	0.619
4.5	5.5	5	0.512
5.5	6.5	6	0.440
6.5	7.5	7	0.388
7.5	8.5	8	0.350
8.5	9.5	9	0.320
9.5	10.5	10	0.296
10.5	11.5	11	0.277
11.5	12.5	12	0.260
12.5	13.5	13	0.246
13.5	14.5	14	0.235
14.5	15.5	15	0.224
15.5	16.5	16	0.215
16.5	17.5	17	0.207
17.5	18.5	18	0.200
18.5	19.5	19	0.194
19.5	20.5	20	0.188
20.5	21.5	21	0.183
21.5	22.5	22	0.179
22.5	23.5	23	0.174
23.5	24.5	24	0.170
24.5	25.5	25	0.167
25.5	26.5	26	0.164
26.5	27.5	27	0.160
27.5	28.5	28	0.158
28.5	29.5	29	0.155
29.5	30.5	30	0.152
30.5	31.5	31	0.150
31.5	32.5	32	0.148
32.5	33.5	33	0.146

Table 6-5: Extreme Turbulence Model values of TI_{ETM} @ 150.0 mDVR90. In addition to application of these values, Integrated Load Analysis for any WTG at the KFII project area shall also be performed using $TI(WS)$ corresponding to the largest centre-wake TI(WS) that the given WTG at the project area can experience; see item d of Section 11.9.3 of [IEC611] and Annex E.1 of ibid. Naturally, these centre-wake values cannot be tabulated before the WTG type and wind farm layout are known.

6.4 Other normal conditions air parameters

6.4.1 Air temperatures

Air temperature conditions at hub height cannot be evaluated using the FLS measurements due to the short measurement campaign. which would not allow for assessing the design temperature according to Table 1-5 of [DNV0126], and the FLSs would not give a reliable indicator of the yearly mean temperature when lacking the summer months. As a start, the Vortex series are compared to their co-located floating Lidars in terms of air temperatures. Since the mesoscale model has 50 m as its lowest elevation, data at this height is compared to the measurements at 4 mSWL at the FLSs. Figure 6-8 shows an example of such a plot for KFII-1-LB, and C2Wind has confirmed that the other FLS yields similar results. The Vortex series is found to have a remarkably strong correlation with the measurements, with a minor bias in mean air surface temperature not higher than 0.3°C across the two FLSs, which is partly explained by the different elevations being compared.

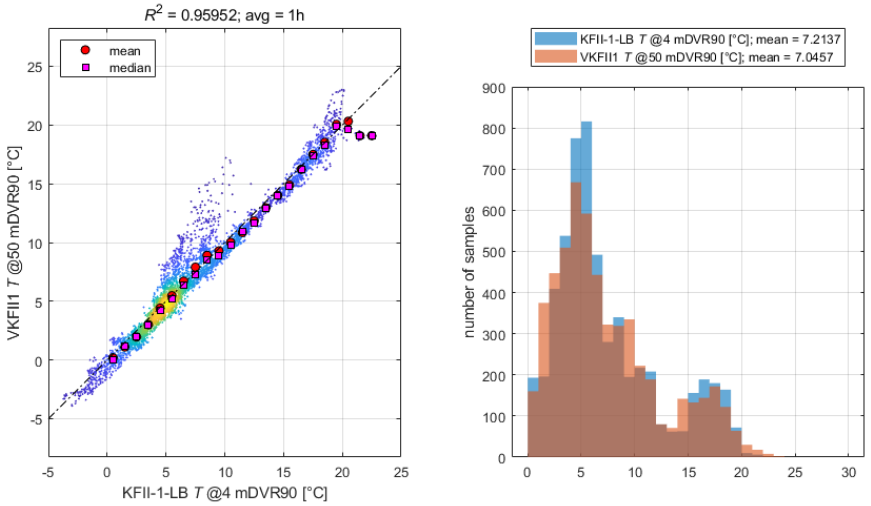

Figure 6-8: Scatter plot and histograms between air temperatures measured by KFII-1-LB and from the co-located Vortex model. The air temperature measured by the FLS is at 4.1 mSWL while the model data is at 50 mMSL.

After the Vortex series has been found to accurately reproduce measured temperatures, the Vortex series for the KFII1 FLS location at 150 mDVR90 is selected for characterising temperatures at the site. The choice of this particular dataset is based on it providing the largest range, ie. it has both the lowest minimum and highest maximum temperature across the two locations with Vortex model data. Furthermore, C2Wind has verified (not shown here) that the conclusions would not change if using the FINO2 temperature measurements at 99 mMSL. See a plot of the Vortex model time series and its histogram in Figure 6-9. Using the time series displayed in the figure, the following design parameters have been evaluated:

Mean air temperature at hub height:	**8.7 °C**
Normal ambient air temperature range, 1-hour mean:	**-7.0 to 26.0 °C**
Extreme ambient air temperature range, 1-hour mean:	**-10.0 to 31.0 °C**

The normal- and extreme ambient air temperature ranges have been assessed using the same type of extreme value analysis as in Section 8.3.2, using 1- and 25-year return periods respectively.

While not explicitly a part of the deliverables requested in [ENCL5], the following temperature-related parameters are often required by WTG OEMs in their site suitability assessments.

Highest temperature in 25 years:	**31.0 °C**
Highest temperature while WTG in production:	**31.0 °C**
Lowest temperature in 25 years:	**-10.0 °C**
Lowest temperature while WTG in production:	**-10.0 °C**

For assessment of the parameters above, “WTG in operation” has been assumed to be equivalent to wind speed at hub height between 3 and 28 m/s, based on modern large WTGs relevant for consideration in the KFII project.

For the selection of steel types for design, the Design Temperature as specified in Table 1-5 of [DNV0126] has been calculated as the lowest daily mean temperature (which is also defined in the same table). Using the time series shown in Figure 6-9 the curve for the daily mean temperature is shown in Figure 6-10, and from its lowest point:

Design Temperature (lowest daily mean temperature): 0.1 °C.

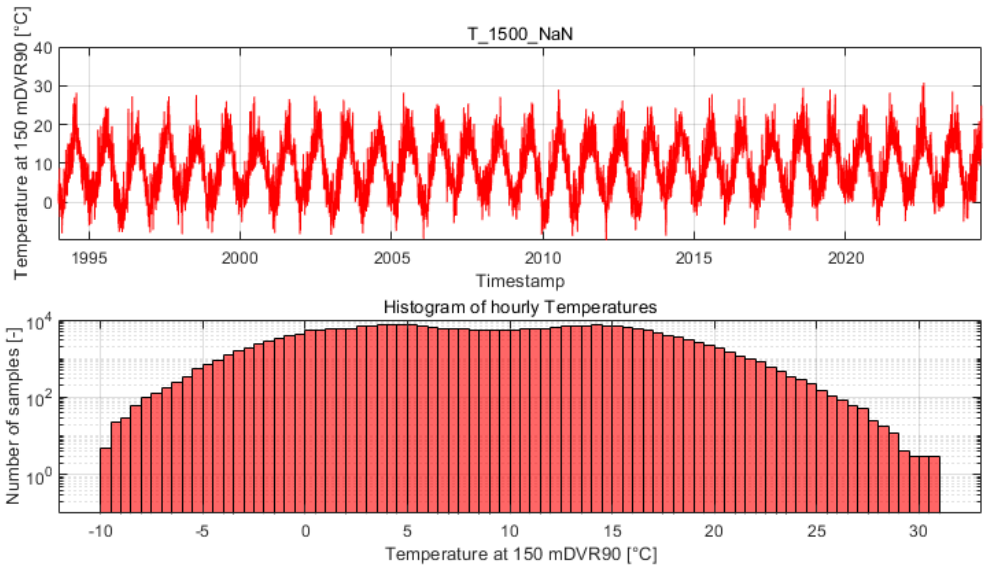

Figure 6-9: Top: time series of hourly air temperature at 150 mDVR90 from the Vortex dataset at the KFII-1-LB location. Bottom: Histogram, with a logarithmic 2nd axis, corresponding to the time series in the top part of the figure.

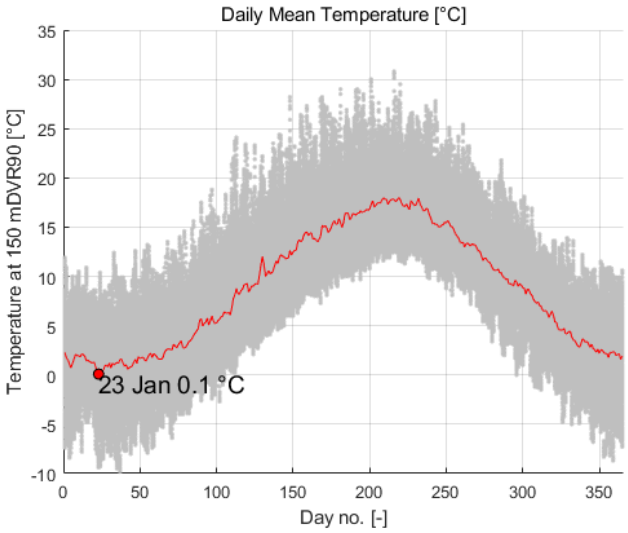

Figure 6-10: Daily mean temperature found from the 1-hour mean temperature values of the dataset shown in the upper part of Figure 6-9. The lowest point on this curve is the design temperature according to Table 1-5 of [DNV0126]. Each value on the red curve is computed as the mean of all the hourly temperature records on the corresponding day of the year denoted on the first axis, using at least 5 different years (which is fulfilled for the Vortex dataset).

6.4.2 Air humidity

In a similar manner to the previous subsection, the relative humidity measurements at the FLSs near the surface were compared to the Vortex time series at its lowest elevation, see Figure 6-11. While the correlation is not as strong as it is for temperatures, C2Wind considers it sufficient for the purposes of this section. From the Vortex mesoscale dataset at the KFII-1-LB location, relative humidity values at 150 mDVR90 are shown as a time series in the left part of Figure 6-12, and a semi-logarithmic histogram in the right part of the figure. On the basis of this information, the following conservative relative air humidity design condition shall be applied:

Relative Humidity design condition, RelH: ≤ 100 %.

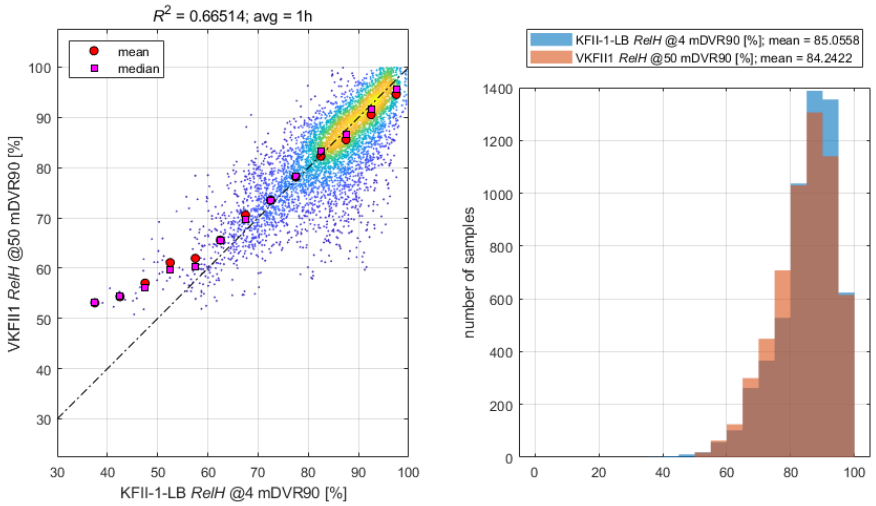

Figure 6-11: Scatter plot and histograms between relative humidity measured by KFII-3-LB at 4.1 mSWL and from the co-located Vortex model at its lowest elevation, 50 mMSL.

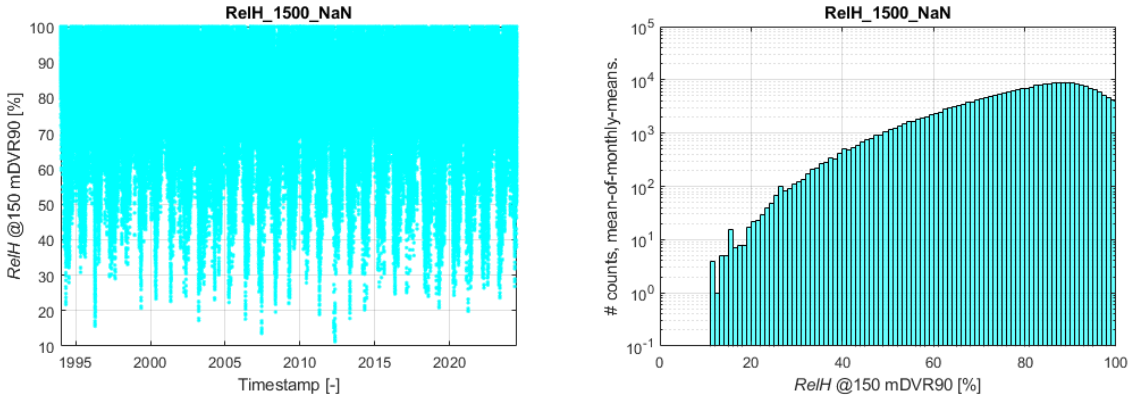

Figure 6-12: The left part of the figure shows the time series of the hourly mean values of relative humidity at 150 mDVR90 from the Vortex mesoscale dataset at the KFII-1-LB location. The figure on the right shows an MoMM histogram of the modelled values with a logarithmic 2nd axis.

6.4.3 Air pressure

In a similar manner to the previous subsection, the atmospheric pressure measurements at the FLSs near the surface were compared to the Vortex time series at its lowest elevation, see Figure 6-13. The correlation is strong, and the small bias can be explained by the comparison between surface level measurements and the lowest model level at 50 mMSL. C2Wind considers the Vortex model dataset adequate for the purposes of this section. Air pressure values from the Vortex mesoscale dataset at the KFII-1-LB location at 150 mDVR90 are shown as a time series in the left part of Figure 6-14, and a semi-logarithmic histogram of these measurements is shown in the right part of the figure.

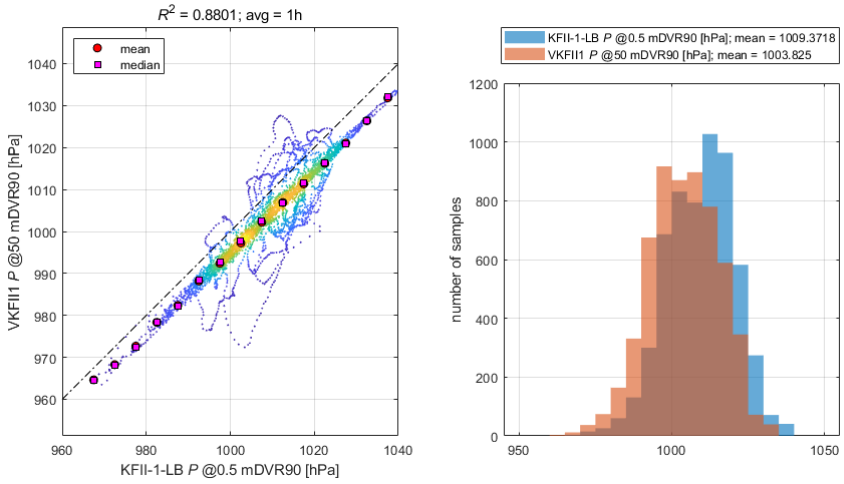

Figure 6-13: Scatter plot and histograms between atmospheric pressure measured by KFII-1-LB at 0.5 mSWL and from the co-located Vortex model at its lowest elevation, 50 mMSL.

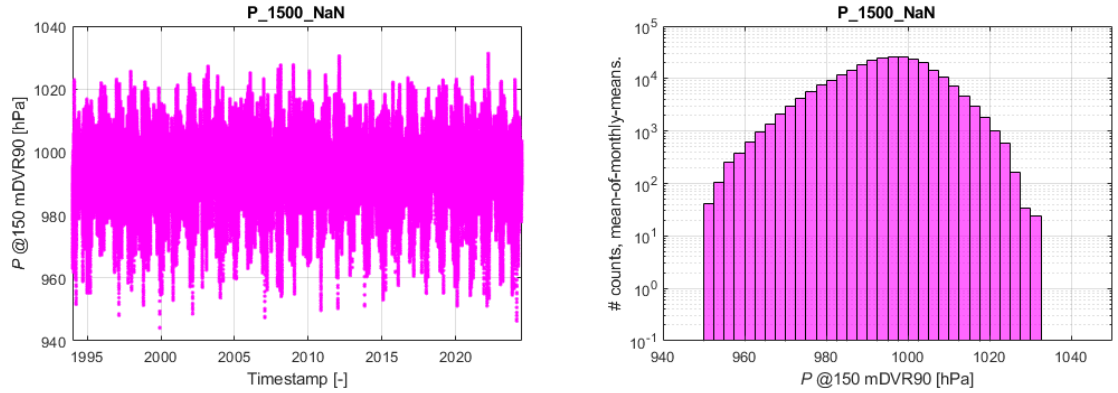

Figure 6-14: The left part of the figure shows the modelled time series of air pressure at 150 mDVR90 from the Vortex mesoscale dataset at the KFII-1-LB location. The right part of the figure shows an MoMM histogram of the modelled values with a logarithmic 2nd axis.

6.4.4 Air density

Air density conditions at hub height have been evaluated using the Vortex mesoscale dataset at the KFII-1-LB location. Using this time series, displayed together with its histogram in Figure 6-15, the normal conditions air density at hub height is assigned the value:

$$\boldsymbol{\rho_{Hub,N}} = \mathbf{1.23}\,\frac{\mathbf{kg}}{\mathbf{m^3}}.$$

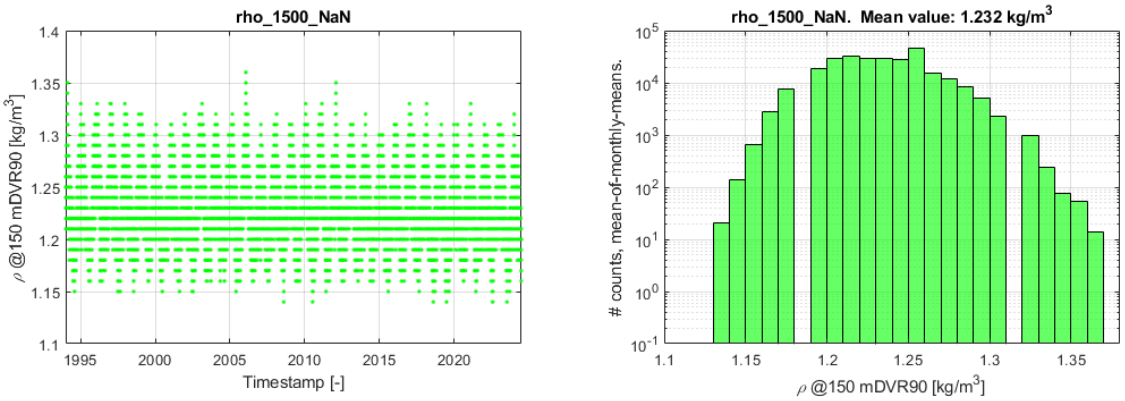

Figure 6-15: Air density at 150 mDVR90 from the Vortex time series computed at the KFII-1-LB location. The left part of the figure shows the model time series, and the right part of the figure shows an MoMM histogram of the model values with a logarithmic 2nd axis. The MoMM mean value is shown in the title above the histogram.

As an additional check, the air density @150 mDVR90 is calculated by using the FINO2 measurements of temperature at 99 mMSL and pressure at 90 mMSL, as well as the KFII-1-LB measurements of temperature and pressure at the surface. The relative humidity could have been included in the calculation, but assuming dry air firstly yields a (conservatively) larger air density, and secondly, the correction due to relative humidity is small enough to be insignificant.

To extrapolate the air density, the air is treated as an ideal gas, i.e. given at each timestamp the pressure *P* and absolute temperature *T*, the density at this timestamp is:

$$\rho = \frac{P \cdot M_{air}}{R \cdot T} \qquad \text{Eq. 6-4}$$

where:

R =	8.3144 J mol^{-1} K^{-1} is the ideal gas constant,
M_{air} =	0.02896 kg/mol is the molar mass of dry air.

With an average atmospheric lapse constant of ca. 0.5 K / 100 m, the transformation of the temperature from measurement elevation to hub height yields only an insignificant difference. The air pressure has been corrected for each timestamp using the equation in the section “Altitude Variation” of [WIKAP]:

$$P(z,t) = P(z_{Ref},t) \cdot \exp\left(-\frac{g\, M_{air}\,(z - z_{Ref})}{R\, T(t)}\right), \qquad \text{Eq. 6-5}$$

where:

$P(z,t)$	is the pressure at elevation z at timestamp t,
$P(z_{Ref},t)$	is the pressure at elevation z_{Ref} at timestamp t,
g =	is the gravitational acceleration; see the table above the Executive Summary,
z =	150 mASL is the elevation,
z_{Ref} =	90 mASL is the reference elevation for FINO2 and 0.5 mMSL for the FLS,
$T(t)$	is the absolute temperature at timestamp t.

The resulting time series are shown in Figure 6-17, and the time series derived from measurements is compared against the Vortex model in Figure 6-16. The results from these two figures confirm that the choice of using the Vortex model time series to describe air density at the site is appropriate for the purposes of the present document.

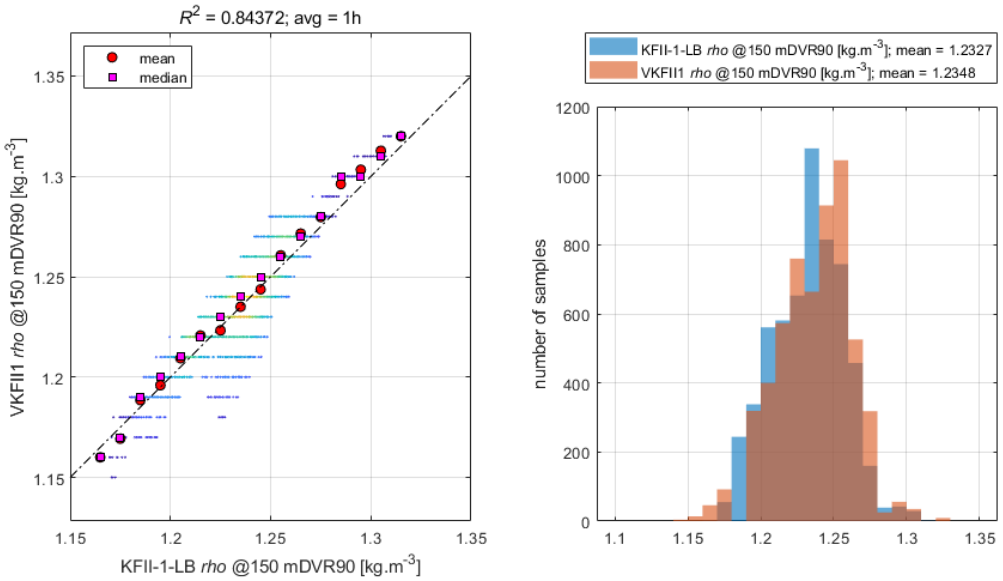

Figure 6-16: Scatter plot and histograms between air density at hub height derived from KFII-1-LB measurements as explained in the text, and modelled by the co-located Vortex model at hub height.

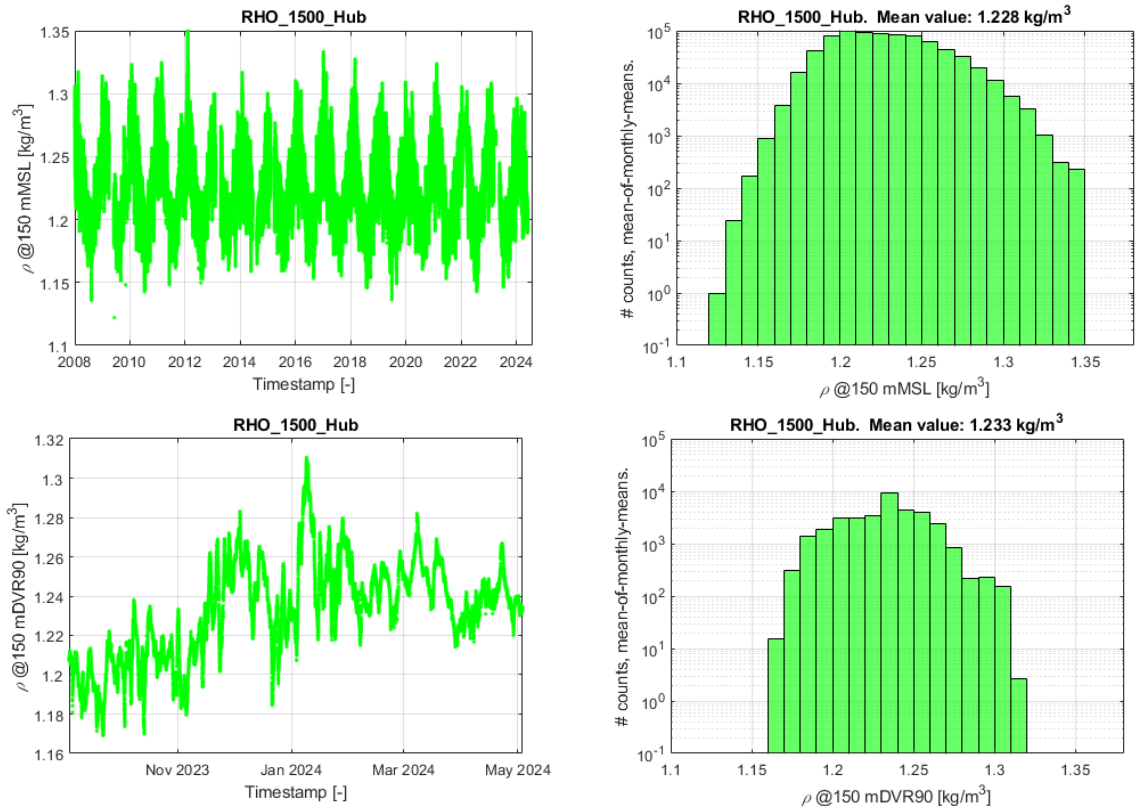

Figure 6-17: Air density at 150 mMSL from the FINO2 measurements (top) and 150 mDVR90 from the KFII-1-LB measurements (bottom). The left part of the figure shows the model time series, and the right part of the figure shows an MoMM histogram of the values with a logarithmic 2nd axis. The MoMM mean value is shown in the title above the histogram.

7. Wind farm induced conditions and gust conditions

7.1 Operational conditions – Wake and Wind Farm Turbulence

The Wind Farm Turbulence is not directly a Site Conditions Assessment issue, since it is both dependent on the RNA type and the wind farm layout and is therefore not included in the present document. The wind farm layout and layout of neighbouring wind farms, wind direction distribution, and wind turbine thrust curves (C_T) shall all be taken into account in the evaluation of the Wind Farm Turbulence.

7.2 Operational conditions – Gust amplitudes

For the Integrated Load Analysis, site specific design gust conditions must be used. This is relevant for the gust types:

- Extreme Operating Gust (EOG);
- Extreme Direction Change (EDC);
- Extreme Coherent Gust with Direction Change (ECD);
- Extreme Wind Shear (EWS).

Evaluation of these gusts is not covered by this report since they depend on both the RNA type and the wind farm layout.

7.3 Extreme wind speed conditions

Effects from neighbouring WTGs during conditions with wind speeds larger than the WTG cut-out wind speed shall be disregarded since their effects are negligible for the purposes of the present document.

8. Extreme Wind Speed Model

This section documents the parameters to be used for load calculations requiring an Extreme Wind Speed Model.

8.1 Wind shear for the Extreme Wind speed Model

The shear exponent for the EWM prescribed in Section 6.3.3.2 of [IEC611], α_{EWM} = 0.11, has been selected for use with the EWM for the present site:

α_{EWM} = 0.11.

This value agrees well with the large wind speed behaviour of the wind shear analysis in both Sections 6.2.1 and 6.2.2. The wind speed profile to be used is the same as prescribed in Section 6.3 (power law). This shear exponent shall be used for scaling extreme wind speeds with elevation, and for describing the wind shear in Integrated Load Analyses that use the EWM.

8.2 Air density for the Extreme Wind speed Model

The three top parts of Figure 8-1 below show data from the time series of the air density calculated from pressure and temperature measurements from the FINO2 met mast and extrapolated to 150 mMSL. Looking only at air densities for the data points with the highest wind speeds, the air density is consistently lower than 1.21 kg/m^3, but as stated in the caption of Figure 8-1, all data points with wind speeds higher than 30 m/s come from only two particular events. Hence, to obtain a better statistical basis for assessing the air density, the top middle and right parts of Figure 8-1 show all data points for *WS* @102 mMSL $\geq$ 25 m/s. Since events with more moderate wind speeds tend to have higher air density than those with higher wind speeds (due to high wind speeds in the region being associated with low values of the air pressure), this leads to a data subset with conservatively high values of the air density associated with high wind speeds. The results obtained with the Vortex dataset (not shown here) are consistent with those found with the FINO2 dataset, which adds confidence to the conclusion reached in Figure 8-1.

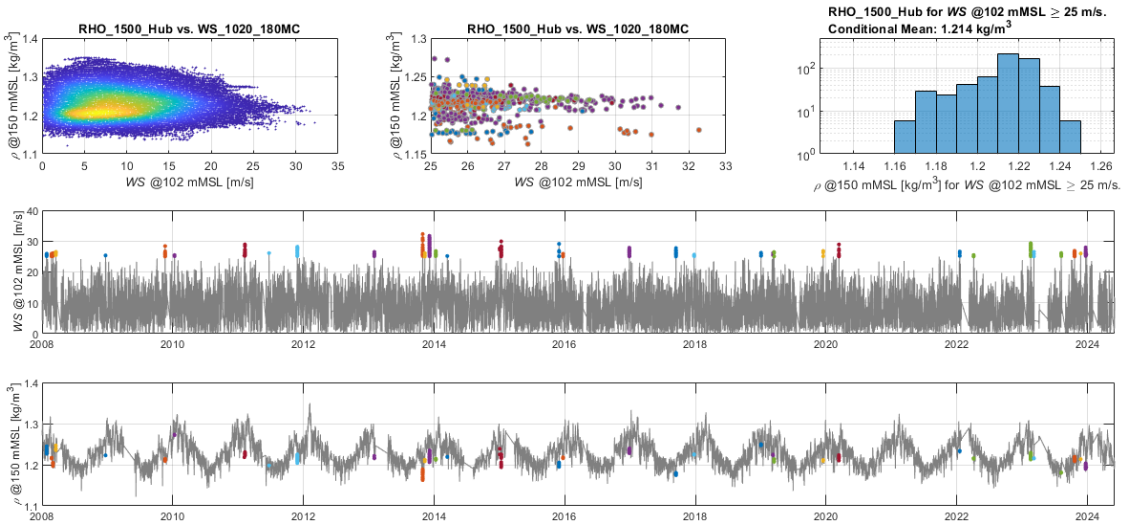

Figure 8-1: Plots for determining the air density for high wind speeds. The scatter plot on the top left shows all air density data from the FINO2 met mast at 150 mMSL vs. wind speed at 102 mMSL, where the colours show the density of points. Density has been extrapolated to hub height as described in Section 6.4.4. The plot at the top in the middle shows a detail of the figure on the left for *WS* ≥ 25 m/s, but the colours here show the timestamp so that similar colours show events that are close in time. By careful study of this figure, one can see that the points with the very strongest wind come from only two events, which is why wind speeds down to 25 m/s have been included in order to capture data from several storms. The top rightmost part of the figure shows a histogram of the data in the plot in the middle, and its title shows the mean value of these air densities. Graphs of the 150 mDVR90 wind speed and -air density time series are shown at the bottom of the figure, where the coloured points correspond to the events shown in the middle figure on the top.

Using the data points highlighted in Figure 8-1 for *WS* @ 150 mDVR90 ≥ 25 m/s, the air density to be used together with the Extreme Wind Model (EWM) is selected as the mean value of their air densities, which is stated in the title of the upper rightmost part of Figure 8-1:

$$\boldsymbol{\rho_{Hub,E} = 1.21 \frac{kg}{m^3}}.$$

8.3 Extreme Wind speeds

The 50-year extreme wind speed estimate has been found by comparing Extreme Value Analysis (EVA) results derived using the FINO2 met mast time series with results derived using standards and guidelines: these derivations are made in the subsections of the present section. Thus, the intermediary results in Sections 8.3.1-8.3.5 (in grey text) shall not be used on their own. Instead, a conclusion on the 50-year extreme wind speed at hub height is provided in Section 8.3.6.

8.3.1 Eurocode 1 supplemented by DS 472

The Danish national annex of [EN01] gives in its Section 4.2 (1)P Note 2 a value of 24 m/s for the basic wind speed applicable all throughout Denmark with the exception of a small area on the west coast, but no value is given for offshore sites. In addition, [EN01] also provides the tools and relations to convert the value given in the national annex to other elevations and recurrence periods. However, [EN01] is not intended to be valid offshore, so the results in the present section are for comparative purposes only.

The Danish standard DS 472 [DS472] also gives in its Section A.2.1 a basic wind speed of 24 m/s applicable all throughout Denmark, and in addition proposes a linear horizontal extrapolation to offshore conditions - increasing to 31 m/s 50 km from the coast. The easternmost point within the KFII site is located approximately 32 km from shore, yielding a basic wind speed of 28.5 m/s (50 years recurrence, 10-minute duration, at 10 mMSL). For the illustrative purposes of this subsection, the same can be applied conservatively to the entire KFII site. Hence:

$$v_{b,0} = 28.5 \text{ m/s}.$$

A roughness length of z_0 = 0.003 m is given for the sea in Table 4.1 of [EN01] and the basic wind speed value above is converted according to the method stated in Section 4.3 of ibid.:

$$WS(z) = 0.19 \left(\frac{0.003 \text{ m}}{0.05 \text{ m}}\right)^{0.07} \ln\left(\frac{\text{z}}{0.003 \text{ m}}\right) v_{b,0} \qquad \text{Eq. 8-1}$$

Please note that the above contains both a conversion to other elevations, but also a conversion from terrain category II to 0 (from roughness length 0.05 m to 0.003 m). The resulting 50-year 10-minute wind speed at 150 mDVR90 is then 48.1 m/s - not to be used; see Section 8.3.6 instead for the conclusion.

8.3.2 Extreme Value Analysis using the FINO2 met mast dataset

Subsets of extreme values belonging to independent storms (separated in time by more than one day) were extracted from the 15-year duration FINO2 met mast 102 mMSL 10-minute wind speed time series, using various threshold values. For each of these subsets, a Generalised Pareto- and a two-parameters Weibull-distribution have been fitted to the histograms of extreme wind speeds. For this particular analysis, the period in which the neighbouring OWF was in operation has not been filtered out, as the threshold values used in the EVA are higher than the expected cut-out wind speed of the neighbouring WTGs.

To estimate the variability of the fit, a bootstrapping-method has been used: Each subset of extreme values has been resampled with replacement, and fitted 1000 times. The Weibull distribution performed better than the General Pareto, and the results are provided in Figure 8-2. These results show that median value results range between 33 and 35 m/s, converging to 33 m/s. From this analysis, a 50-year 10-minute mean wind speed of 34.3 m/s at 102 mMSL has been selected. Extrapolating this to 150 mDVR90, using the shear exponent of 0.11 from Section 8.1, one arrives at 35.8 m/s for the FINO2 mast. Using the 100 m result from [XWIWA] shown in Figure 8-3, the extreme wind speed at 100 mDVR90 is higher at the FINO2 location than at the KFII site, and thus the result for FINO2 can be conservatively used to describe the KFII site with an extreme wind speed of 35.8 m/s at 150 mDVR90 - not to be used; see instead Section 8.3.6 for the conclusion.

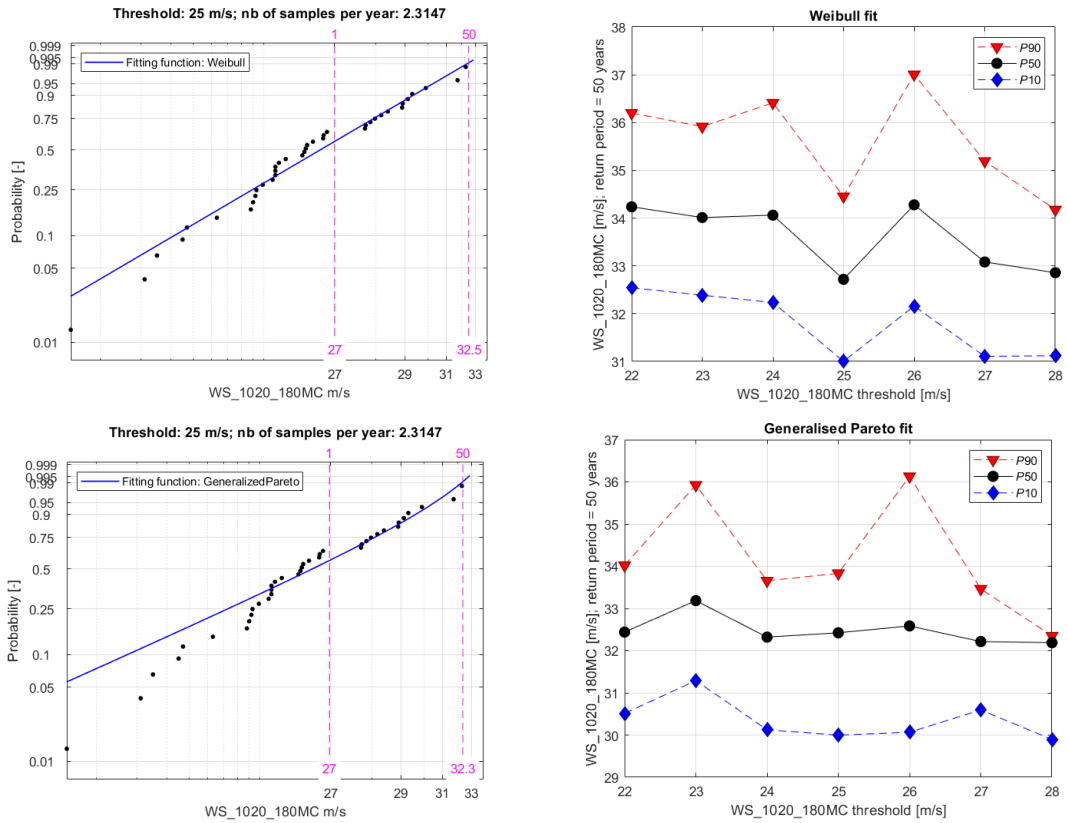

Figure 8-2: Left column: examples of distribution fits to the extreme wind speed values. Right column: results from the Extreme Value Analysis for various wind speed thresholds using the same distribution as on the left. Top row: Weibull distribution. Bottom row: Generalised Pareto distribution.

8.3.3 Extreme Value Analysis using the Arkona met mast dataset

The analysis described in Section 8.3.2 was repeated using the measurements from the 93 mMSL anemometer at the Arkona met mast. The diagnostic plots of the EVA are not shown here for brevity, and the result is a 50-year 10-minute mean wind speed of 35.0 m/s at 93 mMSL, which extrapolated to 150 mDVR90 becomes 36.5 m/s. As in Section 8.3.2, the 100 m result from [XWIWA] shown in Figure 8-3 suggests that the extreme wind speed at 100 mDVR90 is higher at the Arkona met mast location than at the KFII site, and thus the result above can be used to conservatively assign the KFII site an extreme wind speed of 36.5 m/s at 150 mDVR90 - not to be used; see instead Section 8.3.6 for the conclusion.

8.3.4 Estimates from X-WiWa

A map from [XWIWA] of 50-year 10-minute mean extreme wind speed estimates at 100 m (elevation unspecified, but presumably MSL, which for the purposes of the present document equals DVR90 at the KFII site) is shown in Figure 8-3, yielding the largest value for the site of 36 m/s at 100 m. Extrapolating this to 150 mDVR90 using the wind shear description in Section 8.1 yields 37.6 m/s – not to be used; see instead Section 8.3.6 for the conclusion.

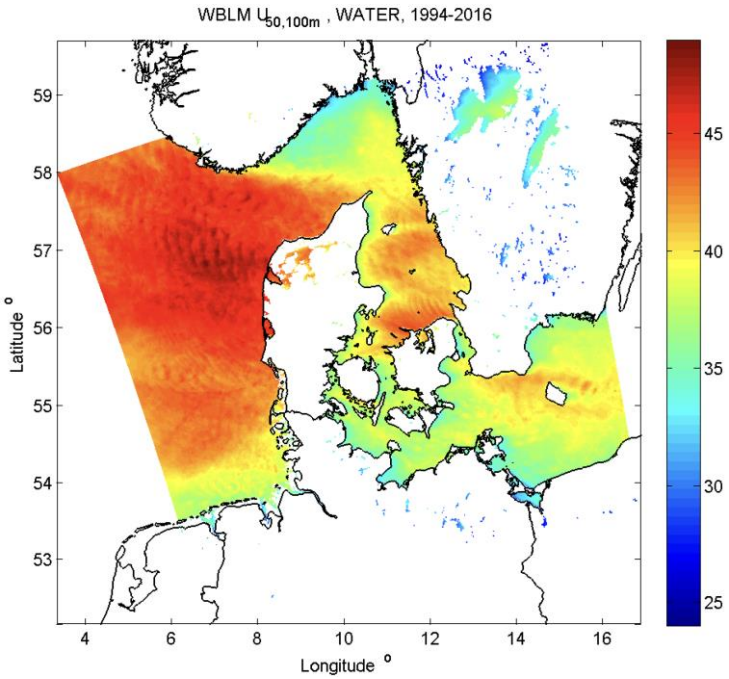

Figure 8-3: Reproduction from [XWIWA] of map of 50-year 10-minute mean extreme wind speed estimates at 100 m (assumed to be 100 mDVR90 – see the text above). CRS: WGS84.

8.3.5 Estimates from Global Atlas of Siting Parameters

A subset of the Global Atlas of Siting Parameters (GASP) data [GASP] covering the KFII project area has been downloaded using windPRO v3.6 and is shown in Figure 8-4. The dataset contains estimates of 50-year 10-minute mean extreme wind speeds at 150 m (elevation unspecified, but presumably MSL, which for the purposes of the present document equals DVR90 at the KFII site). This dataset yields, at the most severe location within the KFII site, an estimate of 42.8 m/s at 150 mDVR90 – not to be used; see instead Section 8.3.6 for the conclusion.

As a side note, the extreme wind speed uncertainties map in [GASP] shows that the site belongs to the medium uncertainty category (this map is not shown in the present report).

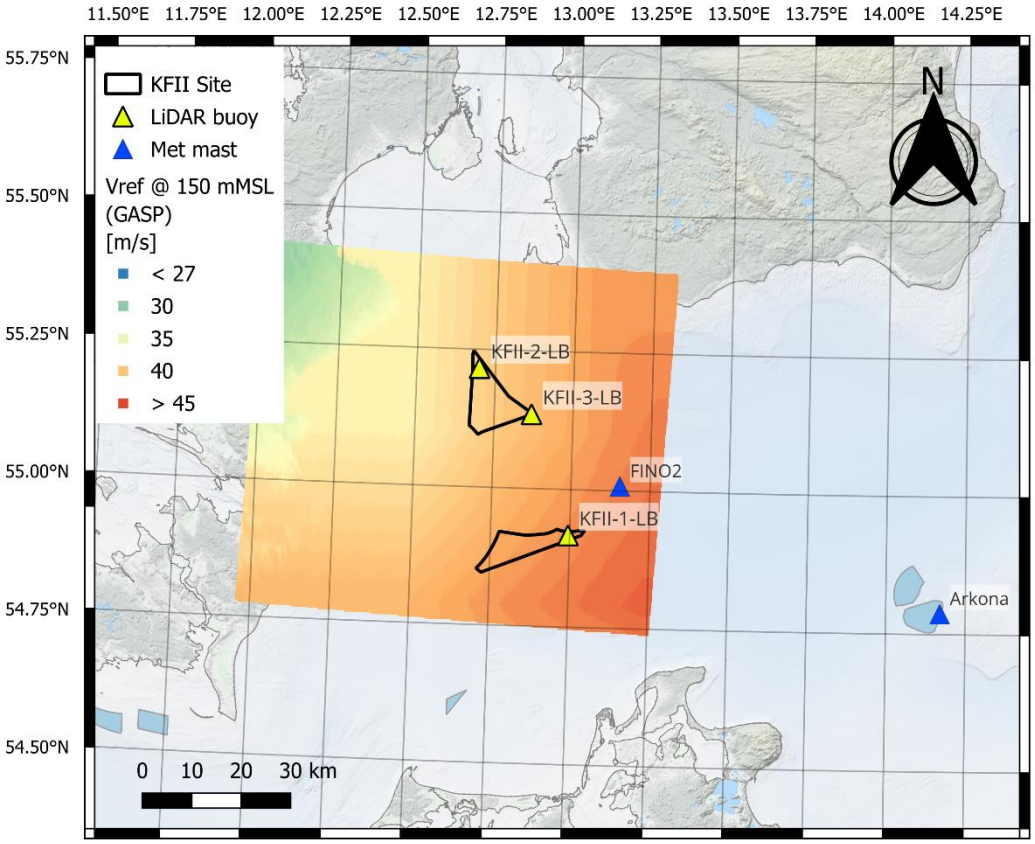

Figure 8-4: Reproduction from [GASP] of map of 50-year 10-minute mean extreme wind speed estimates at 150 m (assumed to be 150 mDVR90 – see the text above). CRS: WGS84.

8.3.6 Comparison of, and conclusion on, extreme wind speed estimates

The results of the previous sections are listed in Table 8-1.

Source	Extreme wind speeds, 10-min mean values at 150 mDVR90
	[m/s]
Section 8.3.1: Eurocode 1991-1-4 / DK NA & DS 472	48.1
Section 8.3.2: FINO2 met mast	35.8
Section 8.3.3 Arkona met mast	36.5
Section 8.3.4: X-WiWa	37.6
Section 8.3.5: Global Atlas of Siting Parameters	42.8

Table 8-1: Overview of the extreme wind speed estimates from standards and guidelines, and from the Extreme Value Analysis using the FINO2- and Arkona met mast measurements; see text. Not to be used in ILA – see instead the conclusion below.

Carefully considering the relevance and uncertainties of the sources yielding the values in Table 8-1, drawing in from C2Wind's experience in the region, the present report selects the following value of the 50-year 10-minute wind speed at hub height:

$WS_{Hub,50}$ = 38.0 m/s.

This value gives weight to the two independent estimates based on near-site measurements, adding a small measure of conservatism on them, and reflects C2Wind's expectations of a certifiable result for the site.

As an intermediate result, the same method and input dataset as in Section 8.3.2 has been used to estimate the 1-year 10-minute wind speed at 102 mMSL at the FINO2 met mast location:

$WS_{102\,mMSL,FINO2,1}$ = 27.3 m/s. Not to be used in ILA – see instead the value below.

The 1-year wind speed at hub height at the site has then been estimated from $WS_{Hub,50}$ above and the ratio between $WS_{102\,mMSL,FINO2,1}$ and $WS_{102\,mMSL,FINO2,50}$ = 34.3 m/s (see Section 8.3.2):

$$\boldsymbol{WS_{Hub,1}} = 38.0\ \text{m/s} \cdot \frac{27.3}{34.3} = \mathbf{30.2\ m/s.}$$

Extreme wind speeds at the additional return periods requested by [ENCL5] have been calculated in a similar manner to that of the 1-year return period, namely, by deriving ratios of EVA results between the different return periods and the 50-year return period.

$\boldsymbol{WS_{Hub,5}}$ **= 33.3 m/s**
$\boldsymbol{WS_{Hub,10}}$ **= 34.7 m/s**
$\boldsymbol{WS_{Hub,25}}$ **= 36.3 m/s**

Furthermore, in order to provide extreme wind speed estimates at each of the analysis points identified in Section 5 and the locations of the two main FLSs, the ratio between the GASP values at the analysis points was used to scale the 50-year wind speed found above, assigning the maximum value to point P2. The scaled results are summarised in Table 8-2.

Point	$WS_{Hub,1}$	$WS_{Hub,5}$	$WS_{Hub,10}$	$WS_{Hub,25}$	$WS_{Hub,50}$
	[m/s]	[m/s]	[m/s]	[m/s]	[m/s]
P1	28.6	31.5	32.8	34.3	35.9
P2	30.2	33.3	34.7	36.3	38.0
KFII-1-LB	30.1	33.2	34.5	36.2	37.8
KFII-2-LB	27.7	30.5	31.7	33.2	34.7

Table 8-2: Summary of 50-year 10-minute wind speed at hub height at the 5 analysis points.

8.4 Turbulence for the Extreme Wind speed Model

For the EWM, the Free Stream Turbulence Intensity used for Integrated Load Analysis shall be set to a conservative value of 11.0 % as suggested in Section 6.3.3.2 in [IEC611].

$\boldsymbol{TI_{EWM}}$ **= 11.0 %.**

9. Other environmental conditions

This section provides background and results for a range of additional environmental conditions relevant to WTG site suitability and design.

9.1 Lightning

[DMILYN] gives an indication of the frequency of lightning strikes in Denmark through stating that the older, rough, estimate of the average area-specific yearly frequency of lightning strikes in Denmark of 1 strike per km^2 per year is an overestimation made by using older measurements from 1965-1978. Furthermore, [DMILYN] uses data from 1991-2000 to state that there may be regional differences in Denmark, with a somewhat larger density in the southwest than in other regions, which seems to be based on the reference (DEFU 2001) on Page 40 of [VEJR130]. Nevertheless, newer high-precision measurements recorded from 2002-2010 treated on Page 40 of [VEJR130] do not indicate any significant regional differences. Furthermore, the 8 years of measurements shown in Figure 4 of [VEJR130] show, together with the corresponding area in Figure 3 of ibid., that the area-specific frequency of lightning strikes can be approximated at ca. 0.5 strikes per km^2 per year. This value agrees well with the result of 0.4-0.65 strikes per km^2 per year shown in Figure 4 of [ATD5] and Figure 5 of [ATD6], which are obtained from data from the years 2008-2012 (for [ATD5]) and 2008-2013 (for [ATD6]).

Thus, for the site in the absence of Wind Turbine Generators (WTGs), the design value is conservatively set to the average value from [VEJR130], which is consistent with the intervals in [ATD5] and [ATD6]:

N_g = 0.5 strikes per km^2 per year. **Valid for the entire site.**

The Lightning Current Parameters, as specified in Table 1 of [IEC24], are such that a conservative Lightning Protection Level is:

Lightning Protection Level: LPL = I. **Valid for the entire site.**

9.2 Solar radiation

The site's maximum solar radiation intensity is conservatively set to a value slightly larger than the maximum theoretical value shown in Figure 5 of [PBUR], which is for a latitude of 52 °N, i.e. several hundred kilometres south of the site. For comparison, this value exceeds by 7% the largest measured value from all of the six Danish measurement stations in Section 10 of [DMIRY]:

Solar Radiation intensity: 1000 W/m^2. **Valid for the entire site.**

9.3 Earthquakes

Peak Ground Acceleration, (PGA), values are derived and reported from the Danish national annex to Eurocode 1998-1, [DK1998NA], see Figure D.2 of ibid., from which a PGA value of 0.2 m/s^2 is prescribed for the site.

As a supplement, a second source is the PGA values derived from the [SHARE] online database, see Figure 9-1, from which a PGA interval of 0.20-0.25 m/s^2 is prescribed for the site.

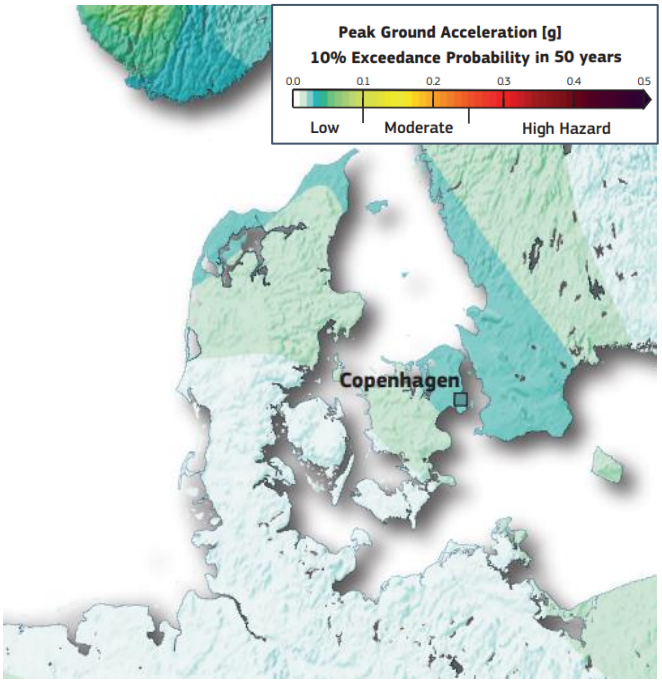

Figure 9-1: Map and colour bar showing the 475-year return period PGA, extracted from the [SHARE] database. Note that the values are in units of g, yielding a PGA interval at the site of <0.25-0.29 m/s^2.

On this basis, the following design value and specification is selected:

Peak Ground Acceleration, 475-year return period: 0.20 m/s^2.

Valid for the entire site.

Depending on the hierarchy of design standards applied in support structure design, the structural designer could be able to justify that seismic Design Load Cases may be neglected. For example, Section 4.2.4.7(2) of [GL12] states that earthquake analyses are not required when PGA < 0.05g, (ca. 0.5 m/s2) where g is the acceleration of gravity.

Alternatively, according to Eurocode 1998-1, [DK1998NA], vertical seismic actions may be ignored. Horizontal seismic actions can be calculated using the PGA value specified above and the simplified load effect evaluation rules in Annex D of [DK1998NA] may be used.

9.4 Icing on blades

As for the vast majority of the Danish Inner Waters coastal areas, the risk of icing on blades is considered to be negligible at the site; see Figure 9-2. Therefore, it is not needed to take into account icing on blades in the Integrated Load Analyses.

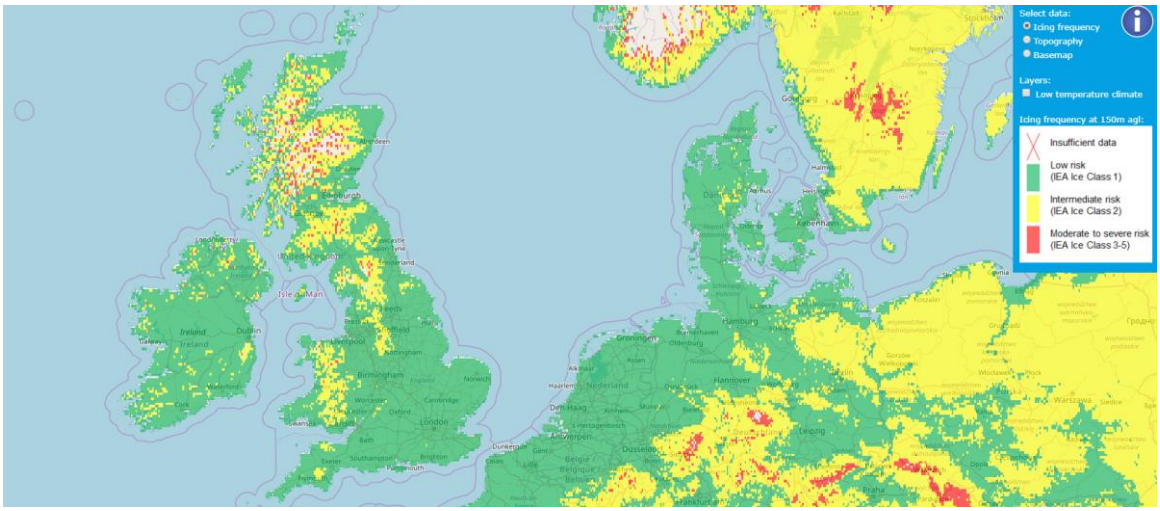

Figure 9-2: IEA wind turbine icing classes, from http://virtual.vtt.fi/virtual/wiceatla/.

Please note that the assessment of sea-ice conditions is outside the scope of the present section and the present document, and thus the conclusions above are limited to icing on blades.

9.5 Precipitation

9.5.1 Seasonal precipitation

The rain- and snow-conditions for the KFII site are in the present report assessed to be representable by the hourly precipitation time series from the ERA5 dataset, interpolated at the centre of the KFII project area, see Figure 9-3. The values correspond well to the representative ones for Denmark and Vordingborg municipality, see Figure 9-4.

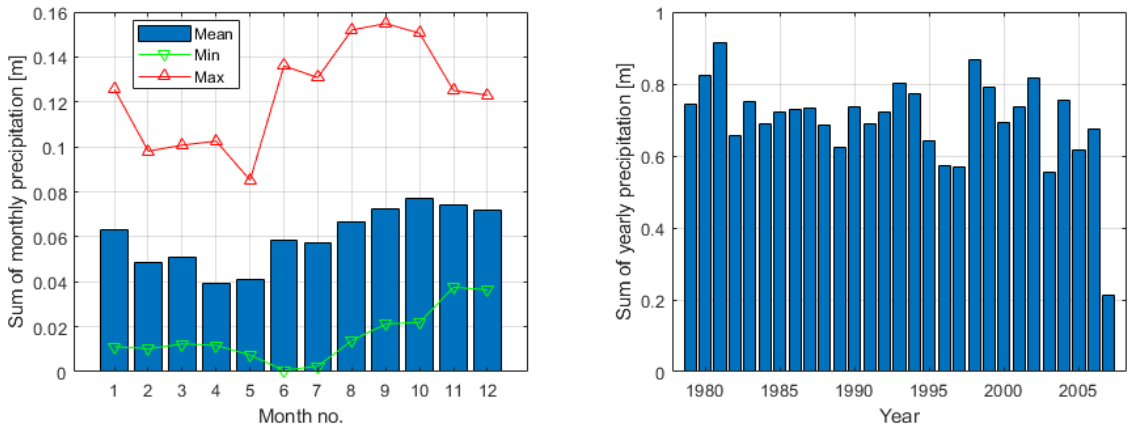

Figure 9-3: Statistics of monthly precipitation at the KFII site, from ERA5 (1979-2007).

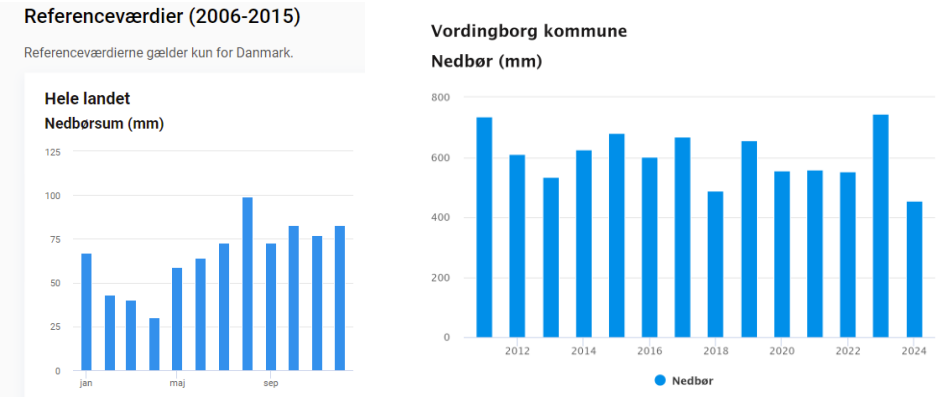

Figure 9-4: Statistics of yearly and monthly precipitations for Denmark (left) and the Vordingborg municipality (right). Source: https://www.dmi.dk/vejrarkiv/.

9.5.2 Hail

The hail conditions at the site are assessed in this report using the [TORRO] scale defined in Table 9-1and Table 9-2 below.

THIS	Intensity Category	Typical Hail Diameter	Probable Kinetic Energy per area	Typical Damage Impacts
		[mm]	[J/m^2]	
H0	Hard Hail	5	0-20	No damage.
H1	Potentially Damaging	5-**15**	>20	Slight general damage to plants, crops.
H2	Significant	10-**20**	>100	Significant damage to fruit, crops, vegetation
H3	Severe	20-**30**	>300	Severe damage to fruit and crops, damage to glass and plastic structures, paint and wood scored.
H4	Severe	25-**40**	>500	Widespread glass damage, vehicle bodywork damage.
H5	Destructive	30-**50**	>800	Wholesale destruction of glass, damage to tiled roofs, significant risk of injuries.
H6	Destructive	40-**60**		Bodywork of grounded aircraft dented, brick walls pitted.
H7	Destructive	50-**75**		Severe roof damage, risk of serious injuries.
H8	Destructive	60-**90**		(Severest recorded in the British Isles). Severe damage to aircraft bodywork.
H9	Super Hailstorms	75-**100**		Extensive structural damage. Risk of severe or even fatal injuries to persons caught in the open.

Table 9-1: TORRO Hailstorm Intensity Scale (THIS), reproduced from https://www.torro.org.uk/research/hail/hscale. The first column shows the THIS, and the second columns shows the corresponding intensity category. The third column shows the approximate hail diameter interval (typical maximum size in bold). Please note that other factors (e.g. number and density of hailstones, hail fall speed and surface wind speeds) also affect severity.

Size code	Maximum Diameter	Description
	[mm]	
0	5-9	Pea
1	10-15	Mothball
2	16-20	Marble, grape
3	21-30	Walnut
4	31-40	Pigeon's egg > squash ball
5	41-50	Golf ball > Pullet's egg
6	51-60	Hen's egg
7	61-75	Tennis ball > cricket ball
8	76-90	Large orange > Soft ball
9	91-100	Grapefruit

Table 9-2: Hail size and diameter in relation to TORRO Hailstorm Intensity Scale (THIS); see Table 9-1. Reproduced from https://www.torro.org.uk/research/hail/hscale.

An extensive review of hail climatology studies in Europe was carried out in [PUNGE16]. From its Figure 3, reproduced in Figure 9-5 below, the KFII area is likely to experience hailstorms of intensity H4 or lower.

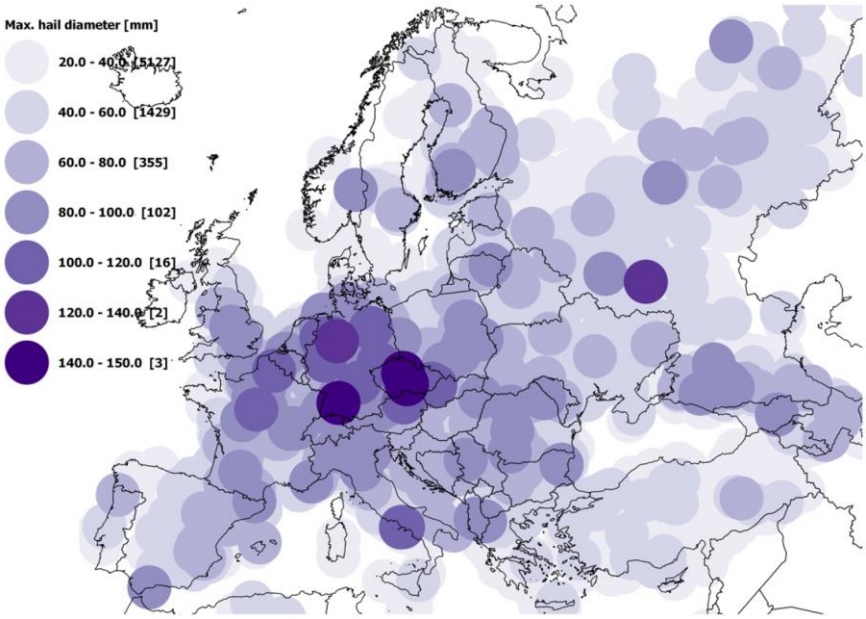

Figure 9-5: Maximum size in mm of hailstones reported to the European Severe Weather Database; reproduced from Figure 3 of [PUNGE16].

Furthermore, from Figure 12 of [HAILCLIM], the number of hail days per year on land close to the site is less than 2 in an area spanning 1° x 1°, when counting only hail with diameters greater than 15 mm. These 2 hailstorms per approximately 7100 km^2 per year will in the present report, by a very conservative assumption of the mean area covered by a hailstorm being 10000 km^2, be translated into 2 per year of such events of hail with diameters greater than 15 mm.

Therefore:

Number of hail days per year (hail diameter ≥ 15 mm): 2.
Maximum THIS to be used in design: H4.

10. References

[ARKDEV] **Deutsche WindGuard.** Offshore Measurement Data Evaluation. Site: Arkona Becken Südost (Germany). Project No. VC11238. Report No. PE11032. Version 1. (2012-09-11).

[ATD5] **Anderson G., Klugmann D**. A European lightning density analysis using 5 years of ATDnet data. Nat. Hazards Earth Syst. Sci. 14, p. 815–829. (2014-04-11). Link: http://www.nat-hazards-earth-syst-sci.net/14/815/2014/nhess-14-815-2014.pdf

[ATD6] **Anderson G., Klugmann D**. A European lightning density analysis using 6 years of ATDnet data. 2014-ILDC-ILMC. (2014-03-18). Link: https://www.vaisala.com/sites/default/files/documents/Anderson%20and%20Klugman-A%20European%20lightning%20density%20analysis-2014-ILDC-ILMC.pdf *Please note: This is partially an extension of [ATD5].*

[DBW] **Marine Data Exchange**. 2013-2017, Zone 3 Dogger Bank, West Met Mast Wind, Wave and CTD Data. Link: https://www.marinedataexchange.co.uk/details/TCE-2465/2013-2017-zone-3-dogger-bank-west-met-mast-wind-wave-and-ctd-data

[DK1998NA] **Danish housing and planning authority**. DS/EN 1998-1 DK NA:2020. National Annex to Eurocode 8: Design of structures for earthquake resistance - Part 1: General rules, seismic actions and rules for buildings. (2020-08-25).

[DMILYN] **DMI**. Lynstatistik. Link: https://www.dmi.dk/vejr-og-atmosfare/temaforside-lyn-og-torden/lynstatistik/

[DMIRY] **DMI**. Technical Report 13-19. 2001 – 2010 Danish Design Reference Year, DMI (2013). Link: https://www.dmi.dk/fileadmin/user_upload/Rapporter/TR/2013/TR13-19.pdf

[DNV0126] **DNV**. DNV-ST-0126 - Support structures for wind turbines (2021-12).

[DNV0437] **DNV**. Standard DNV-ST-0437 - Loads and site conditions for wind turbines, Edition November 2016, Amended November 2021, DNV AS (2021-11).

[DOW30DR] **Energinet Eltransmission**. Stations and deployment record – DOW2030. Filename: *Stations and deployment record - DOW2030.xlsm*

[DOW30GR] **Fugro**. Gap Report 01, Kriegers Flak II. Danish Offshore Wind 2030 – Floating LiDAR Measurements. Doc No. C75517-KFII-GAP-01 03. (2024-02-28).

[DOW30MR] **Fugro**. Danish Offshore Wind 2030 – Floating LiDAR Measurements. Monthly Reports for Kriegers Flak II. Sharepoint folder containing 8 monthly reports for the FLS positions KFII-1-LB and KFII-2-LB in KFII, covering the period 2023-09 to 2024-05.

[DOW30PEPL2] **Fugro Norway AS**. SWLB measurements – Danish Offshore Wind 2030. Project Execution Plan Lot 2. Doc. No. C75517-PEP 05 (2023-12-05).

[DOW30PMP] **Fugro Norway AS**. SWLB measurements – Danish Offshore Wind 2030. Project Measurement Plan, All Lots. Doc. No. C75516/C75517/C75518_Project_Measurement_Plan_All_Lots (2023-11-23).

[DOW30SR] **Fugro**. Danish Offshore Wind 2030 – Floating LiDAR Measurements. Service Reports for Kriegers Flak II. Sharepoint folder containing 1 service report for the three FLSs in KFII.

[DS472] **Dansk Standard**. External conditions in Denmark for the design of wind turbines. DS 472 E. Dansk Standard (2007-06-28).

[DTU24] **Larsén, X. G**. (2024). Calculating Turbulence Intensity from mesoscale modeled Turbulence Kinetic Energy. DTU Wind and Energy Systems. DTU Wind Energy E No. E-0233

[EIBSDR] **Energinet Eltransmission**. Stations and deployment record – EIBS. Filename: *Stations and deployment record - EIBS.xlsx*

[EIFRL3] **Fugro Norway AS.** Energy Islands – Floating LiDAR Measurements. Final Campaign Report for Lot 3, November 2021 – November 2022. Doc. No. C75487-Lot 3-R12-001 06 (2024-05-02).

[EIPMP] **Fugro Norway AS**. SWLB Measurements at Energy Islands. Project Measurement Plan, All Lots. Doc. No. C75486_Project_Measurement_Plan_All_Lots (2023-05-30).

[EMD18] **Svenningsen L., Slot R. M. M., Thørgensen M. L**. A novel method to quantify atmospheric stability. WindEurope 2018.

[EMEIS18] **Emeis S**. Wind Energy Meteorology. Atmospheric Physics for Wind Power Generation (2018).

[EN01] **European Committee for Standard (CEN)**. Eurocode 1: Actions on structures - Part 1-4: General actions - Wind actions. EN 1991-1-4:2007. CEN (2007). The applied Danish Annex is: DS/EN 1991-1-4 DK NA:2015 (2015-07-07).

[ENCL5] **Energinet Eltransmission**. Scope of Services – Site Wind Conditions Assessments for Kriegers Flak II. Document No. 23/14427-6, Version 1. (2023-11-28).

[ERA5] **Copernicus Climate Change Service (C3S)**. ERA5: Fifth generation of ECMWF atmospheric reanalyses of the global climate. Copernicus Climate Change Service Climate Data Store (CDS). (2017). Link: https://cds.climate.copernicus.eu/cdsapp#!/home

[FINO] **BSH**. FINO – Database information – Research platforms in the North Sea and Baltic Sea. Link to database: https://www.bsh.de/EN/TOPICS/Monitoring_systems/MARNET_monitoring_network/FINO/fino_node.html
Link to FINO1 metadata: https://www.bsh.de/DE/THEMEN/Beobachtungssysteme/Messnetz-MARNET/FINO/_Anlagen/Downloads/FINO1_metadata.html;jsessionid=3B88D75F609E26BF35315EF94CA6A9C1.live11293
Link to FINO3 metadata: https://www.bsh.de/DE/THEMEN/Beobachtungssysteme/Messnetz-MARNET/FINO/_Anlagen/Downloads/FINO3_metadata.html;jsessionid=3B88D75F609E26BF35315EF94CA6A9C1.live11293

[FINO2MD] Link: https://www.bsh.de/DE/THEMEN/Beobachtungssysteme/Messnetz-MARNET/FINO/_Anlagen/Downloads/FINO2_metadata.html;jsessionid=5773A236777AD00DC161FFAD25D0C8D7.live11312

[FINOFR] **DWD.** Abschlussbericht - Förderprogramm des Bundesministeriums für Wirtschaft und Energie Forschungsvorhaben FINO-Wind - Standardisierung und vergleichende Analyse der meteorologischen FINO-Messdaten (FINO123). Fördererkennzeichen: 0325508. (2016-11-28).

[FRANDSEN92] **Frandsen S**. On the wind speed reduction in the center of large clusters of wind turbines. Journal of Wind Engineering and Industrial Aerodynamics (1992).

[GASP] **DTU**. Global Wind Atlas Science Portal. Link: https://science.globalwindatlas.info/#/map

[GG24] **Gandoin, R. and Garza, J.** Underestimation of strong wind speeds offshore in ERA5: evidence, discussion, and correction, Wind Energ. Sci. Discuss. [preprint], https://doi.org/10.5194/wes-2024-27 , in review, 2024.

[GL12] **GL**. Rules and Guidelines – Industrial Services: Guideline for the Certification of Offshore Wind Turbines, Edition 2012. GL Renewables Certification (2012-12-01).

[GRYNING07] **Gryning S-E., Batcharova E., Brümmer B., Jørgensen H., Larsen S**. On the extension of the wind profile over homogeneous terrain beyond the surface boundary layer. Boundary-Layer Meteorology (2007).

[GWA] **DTU**. Global Wind Atlas. Link: https://globalwindatlas.info/en

[HAILCLIM] **Handa W. H., and Cappelluti G**. A global hail climatology using the UK Met Office convection diagnosis procedure (CDP) and model analyses. Meteorological Applications 18, p. 446–458 (2011-01-04). Link: http://onlinelibrary.wiley.com/doi/10.1002/met.236/full

[HNSDTR19] **Hannesdóttir Á., Kelly M., and Dimitrov N**. Extreme wind fluctuations: joint statistics, extreme turbulence, and impact on wind turbine loads. Wind Energ. Sci., 4, 325–342 (2019). Link: https://doi.org/10.5194/wes-4-325-2019

[HOLTSLAG15] **Holtslag M.C., Bierboom W.A.A.M., van Brussel G.J.W**. Validation of surface layer similarity theory to describe far offshore marine conditions in the Dutch North Sea in scope of wind energy research (2015). Link: https://www.sciencedirect.com/science/article/abs/pii/S0167610514002153

[HWANG20] **Hwang Y, Lee M**. The mean logarithm emerges with self-similar energy balance. Journal of Fluid Mechanics. 2020;903:R6. doi:10.1017/jfm.2020.730

[IEC24] **IEC**. Wind turbines - Part 24: Lightning Protection, IEC 61400-24 ed. 2.0, International Electrotechnical Commission. (2019-07-03).

[IEC611] **IEC**. IEC 61400-1: Wind energy generation systems – Part 1: Design Requirements. Edition 4.0. International Electrotechnical Commission (2019-02).

[IEC6131] **IEC**. IEC 61400-3-1: Wind energy generation systems – Part 3-1: Design requirements for fixed offshore wind turbines. Edition 1.0. International Electrotechnical Commission (2019-04-05).

[KAIMAL72] **Kaimal J. C., Wyngaard J. C., Izumi Y., Coté O. R**. Spectral characteristics of surface-layer turbulence. Quarterly Journal of the Royal Meteorological Society (1972-07). Link: https://apps.dtic.mil/sti/pdfs/AD0748543.pdf

[KANG16] **Kang S.-L., Won H**. Spectral structure of 5 year time series of horizontal wind speed at the Boulder Atmospheric Observatory. Journal of Geophysical Research – Atmospheres (2016-10-03). Link: https://agupubs.onlinelibrary.wiley.com/doi/full/10.1002/2016JD025289

[LARSÉN16] **Larsén X. G., Larsen S. E., Petersen E. L**. Full-Scale Spectrum of Boundary-Layer Winds. Boundary-Layer Meteorology 159, Page 349-371 (2016-02-02). Link: https://orbit.dtu.dk/en/publications/full-scale-spectrum-of-boundary-layer-winds

[LARSÉN18] **Larsén X. G., Petersen E. L., Larsen S. E**. Variation of boundary-layer wind spectra with height. Quarterly Journal of the Royal Meteorological Society (2018-04-02). Link: https://doi.org/10.1002/qj.3301
Second link: https://backend.orbit.dtu.dk/ws/files/146995032/Lars_n_et_al_2017_Quarterly_Journal_of_the_Royal_Meteorological_Society.pdf

[MAEIBS] **DHI**. Energy Island Baltic Sea – Metocean Assessment – Part A: Description and Verification of Data Basis. IO Number 4500092960, Revision 1.0 (2023-06-28). Link: https://ens.dk/sites/ens.dk/files/Vindmoller_hav/3107a_11829021_dhi_eibs_metocean_parta_description_and_verification_of_data_basis_final_1.2_2024-02-07.pdf

[MARUSIC13] **Marusic I., Monty J. P., Hultmark M., Smits A. J**. On the logarithmic region in wall turbulence. J. Fluid Mech (2013).

[MARUSIC19] **Marusic I., Monty J. P**. Attached Eddy Model of Wall Turbulence. Annual Review of Fluid Mechanics (2019).

[MATAJI22] **Mataji B**. On the extension of streamwise turbulence intensity profile beyond the atmospheric surface layer under neutral to unstable stratifications. Journal of Wind Engineering and Industrial Aerodynamics (2022-07-31). Link: https://www.sciencedirect.com/science/article/abs/pii/S016761052200201X

[MERRA2] **Gelaro R. et al**. The Modern-Era Retrospective Analysis for Research and Applications, Version 2 (MERRA2). Journal of Climate (2017-07-15). Link: https://journals.ametsoc.org/view/journals/clim/30/14/jcli-d-16-0758.1.xml

[MOMKOM] **C2Wind**. Site Wind Conditions Assessment – Kriegers Flak II and North Sea 1 – Kick off meeting. (2024-06-06).

[NEWA] **New European Wind Atlas**. A free, web-based application developed, owned and operated by the NEWA Consortium. Link: http://www.neweuropeanwindatlas.eu

[NORA3] **MET Norway**. The 3-km Norwegian Reanalysis (NORA3). Link: https://data.met.no/dataset/ddb4c5d1-70b5-4d09-98a8-fadbf5e2d2ba

[PANOF84] **Panofsky H., Dutton J**. Atmospheric Turbulence: Models and Methods for Engineering Applications (1984).

[PBUR] **Burgess P**. Variation in light intensity at different latitudes and seasons, effects of cloud cover, and the amounts of direct and diffused light. Presentation to Continuous Cover Forestry Group (CCFG) Scientific Meeting 29 September 2009, Westonbirt Arboretum, Gloucestershire. Cranfield University (2009-09-29). Link: https://www.ccfg.org.uk/wp-content/uploads/2017/11/Conf09_PBurgess.pdf

[PO164] **Neumann T., Bégué F., Wilts F., Leiding T., Tinz B., Gates L., Senet C., Schwenk P., Bastigkeit I., Müller S.** Standardization of meteorological data from offshore platforms. EWEA Offshore 2015 – Copenhagen (2015-03-12).

[PO293] **Przemek M., Grey T., Hay A**. A study of the variation in offshore turbulence intensity around the British Isles (2016). Link: https://windeurope.org/summit2016/conference/allposters/PO293.pdf

[POLLAK] **Pollak D. A**. Characterization of Ambient Offshore Turbulence Intensity from Analysis of Nine Offshore Meteorological Masts in Northern Europe. DTU Wind Energy Master Thesis M-0056. EWEM/DTU/UO (2014-08-03).

[PUCCIONI22] **Puccioni M, Calaf M, Pardyjak ER, et al**. Identification of the energy contributions associated with wall-attached eddies and very-large-scale motions in the near-neutral atmospheric surface layer through wind LiDAR measurements. Journal of Fluid Mechanics. 2023;955:A39. doi:10.1017/jfm.2022.1080

[PUNGE16] **Punge H. J., and Kunz M**. Hail observations and hailstorm characteristics in Europe: A review. Atmospheric Research (2016).

[RAMLI] **Ramli S., and Windolf M. H**. Uncertainty in the application of the Measure-Correlate-Predict (MCP) method in wind resource assessment. EWEA Offshore 2011 (2011-11). Link: http://c2wind.com/f/content/sundus_ramli_p0355.pdf

[SHARE] **Seismic Hazard Harmonization in Europe**. Link: http://www.efehr.org/earthquake-hazard/hazard-map/

[SHAREP] **Energinet Eltransmission**. Sharepoint site: 505-Site Wind Conditions Assessment North Sea I. Link: https://energinet.sharepoint.com/sites/PR_505-SiteWindConditionsAssessmentNorthSeaI

[SINCLAIR22] **Sinclair V. A. et al**. Boundary-layer height and surface stability at Hyytiälä, Finland, in ERA5 and observations (2022).

[SWLB085] **DNV**. SWLB085. Independent performance verification of SEAWATCH Wind Lidar Buoy at Frøya, Norway. Doc. No. 10422674-R-18-A (2023-10-09).

[TENNEKES73] **Tennekes H**. The logarithmic wind profile (1973).

[THORWA] **C2Wind**. Thor Offshore Wind Farm - Wind Conditions for a Light Site Conditions Assessment. Doc. no. 19009-4-2 (2021-01-29). Link: https://ens.dk/sites/ens.dk/files/Vindenergi/2_thor_owf_wind_conditions_for_a_light_site_conditions_assessment.pdf

[TORRO] **The Tornado & Storm Research Organisation (TORRO)**. Full database of TORRO Hail Intensity Scale H5+ hailstorms from the years 1660-2012:

[TOWNSEND76] **Townsend A.A**. The structure of the turbulence shear flow. Second edition (1976).

[VEJR130] **Andersson S., Damsberg N**. En statistisk analyse af danske lyn-data 2002-2010. Vejret 130, p. 35-41. Dansk Meteorologisk Selskab (2012-02). Link: https://www.dams.dk/file-share/e875318a-59d3-4e6d-aea3-f5864c676031

[WANG14] **Wang H., Barthelmie R. J., Pryor S. C. and Kim H. G**. A new turbulence model for offshore wind turbine standards, Wind Energy, 17, pages 1587–1604, doi: 10.1002/we.1654 (2014).

[WIKAP] Link: https://en.wikipedia.org/wiki/Atmospheric_pressure

[WS172] **DNV.** WS172. Independent performance verification of SEAWATCH Wind Lidar Buoy at Frøya, Norway. Doc. No. 10422674-R-6-B (2023-08-25).

[WS190] **DNV.** WS190. Independent performance verification of SEAWATCH Wind Lidar Buoy at Frøya, Norway. Doc. No. 10422674-R-16-A (2023-08-15).

[WS210] **DNV.** WS210. Independent performance verification of SEAWATCH Wind Lidar Buoy at Frøya, Norway. Doc. No. 10422674-R-7-B (2023-09-01).

[XI24] **Xi X., Yang Q., Liu C., Shupe M.D**. Evaluation of the Planetary Boundary Layer Height From ERA5 Reanalysis With MOSAiC Observations Over the Arctic Ocean (2024).

[XWIWA] **X-WiWa**. Main results. Link: https://www.xwiwa.dk/main-results

[ZX1004] **DNV.** ZX1004. Independent analysis and reporting of ZX Lidars performance verification executed by ZX Lidars at the UK Remote Sensing Test Site. Doc. No. 10422597-A-122-A (2023-08-15).

[ZX1915] **DNV.** ZX1915. Independent analysis and reporting of ZX Lidars performance verification executed by ZX Lidars at the UK Remote Sensing Test Site. Doc. No. 10422597-A-134-A (2023-09-26).

[ZX709] **DNV.** ZX709. Independent analysis and reporting of ZX Lidars performance verification executed by ZX Lidars at the UK Remote Sensing Test Site. Doc. No. 10422597-A-82-A (2023-07-31).

[ZX757] **DNV.** ZX757. Independent analysis and reporting of ZX Lidars performance verification executed by ZX Lidars at the UK Remote Sensing Test Site. Doc. No. 10332408-A-29-B (2022-07-26).

[ZX809] **DNV.** ZX809. Independent analysis and reporting of ZX Lidars performance verification executed by ZX Lidars at the UK Remote Sensing Test Site. Doc. No. 10332408-A-65-A (2022-10-27).

Appendices

This page is intentionally left blank.

Appendix A. Derivation of Weibull parameters

The derivation of the Weibull parameters at the analysis points derived in Section 5 was carried out using the following methodology:

1) The long-term wind speed at hub height is estimated at the FLS measurement locations KFII-1-LB and KFII-2-LB. Note that since KFII-3-LB measurements are available for only 5 months while KFII-1-LB and KFII-2-LB measurements are available for 8 months, it was decided not to include KFII-3-LB in the derivation of Weibull parameters.
2) The long-term wind speed time series is spatially extrapolated from KFII-1-LB and KFII-2-LB to the analysis points.
3) Weibull parameters are fitted to the extrapolated time series at the analysis points.

The datasets used to derive the Weibull parameters are summarised in Table A-1, along with an indication of their use for the analysis steps outlined above.

Dataset	Use in the derivation of Weibull parameters	Description
KFII-1-LB	1) Long-term hub height wind speed time series. 2) Horizontal extrapolation.	Section B.1
KFII-2-LB	1) Long-term hub height wind speed time series. 2) Horizontal extrapolation.	Section B.1
BHI-1-LB	1) Long-term hub height wind speed time series. 2) Horizontal extrapolation.	Section B.2
BHII-1-LB	1) Long-term hub height wind speed time series. 2) Horizontal extrapolation.	Section B.2
Vortex	1) Long-term hub height wind speed time series.	Not described in this document
NORA3	2) Horizontal extrapolation.	See [NORA3]
ERA5	2) Horizontal extrapolation.	See [ERA5]
MERRA2	1) Long-term hub height wind speed time series. 2) Horizontal extrapolation.	See [MERRA2]
NEWA	2) Horizontal extrapolation.	See [NEWA]
GWA	2) Horizontal extrapolation.	See [GWA]

Table A-1: Datasets used for the derivation of Weibull parameters.

A.1 Long-term hub height wind speed at the KFII FLSs

The FLS measurements collected within the KFII area are best suited to describe the wind conditions at the project site. The FLS measurements need to be long-term corrected to provide estimates representative of the wind farm lifetime. Furthermore, at the time of writing this report only 8 effective months of FLS measurements are available, and thus additional steps need to be taken to ensure that the Weibull parameters derived from these measurements are free of seasonal bias.

The long-term correction can be done using another available time series which better represents the distribution of the wind speed in the long-term. The following model datasets were considered as potential long-term references:

- **NORA3**: This mesoscale time series was found to have a good correlation with the FLS measurements collected at KFII and Energy Island Bornholm (EIB), but are only available until 2024-02-31, thus having only 4 concurrent months with the

KFII-1-LB and KFII-2-LB datasets. Since such a short concurrent period would exacerbate the risk of seasonal bias already present with the short measurement duration, it was decided not to use NORA3 for the long-term correction of the FLS measurements.

- **Vortex**: This mesoscale time series was found to have a good correlation with the FLS measurements at KFII and is available for the period from 1994-01-01 to 2024-07-01, thus allowing for the use of the full FLS measured dataset.
- **ERA5**: This reanalysis time series was found to have a good correlation with the FLS measurements at KFII and EIB and is available for the period from 1940-01-01 to 2024-06-30, thus also allowing for the use of the entire measured dataset. Since ERA5 was used as input to the Vortex time series, these two datasets are not independent, and only the higher quality Vortex dataset was included in the long-term correction.
- **MERRA2**: This reanalysis time series was found to have a good correlation with the FLS measurements at KFII and EIB and is available for the period from 1980-01-01 to 2024-05-31, thus also allowing for use of the entire measured dataset.

The analysis uses the Measure-Correlate-Predict (MCP) method "Variance Ratio" described in [RAMLI] with 12 wind directional bins. The wind speed from KFII-1-LB and KFII-2-LB at 150 mMSL were used as short-term datasets while data from mesoscale and reanalysis time series Vortex and MERRA2 were used as long-term references. Different MCP configurations were used as part of sensitivity checks and in order to obtain a robust assessment of the long-term wind speed. Such checks included assessment of a range of long-term periods, from 5 to 30 years, as well as directional binning, regression method and time averaging. Table A-2 shows the results for long-term mean wind speed obtained using selected MCP configurations. The results for all long-term reference time series show that the estimated long-term mean wind speed is not highly sensitive to the length of the long-term period for periods between 13 and 23 years. In the case of long-term wind speed estimated at KFII-2-LB, the variance between MCP estimates for the same short-term measurement when using different long-term sources starts to increase for very long-term periods. Furthermore, the variance between individual MCP results for the two FLSs converges to similar values for an 18 year period, whereafter the two FLSs have differing trends in their MCP variances. Thus, an 18-year period seems to be the most appropriate long-term choice valid for both FLSs. Additionally, although not shown in the document, the results obtained when using different averaging periods are very similar.

Results from MCP analysis Long-term *WS* at KFII FLSs @ 150 mMSL [m/s]								
Location	Long-term reference	LT start 2019-06 (5 y)	LT start 2014-06 (10 y)	LT start 2009-06 (15 y)	LT start 2006-06 (18 y)	LT start 2004-06 (20 y)	LT start 1999-06 (25 y)	LT start 1994-06 (30 y)
KFII-1-LB	Vortex	9.69	9.74	9.75	9.77	9.75	9.69	9.68
KFII-1-LB	MERRA2	9.71	9.75	9.75	9.76	9.74	9.68	9.68
KFII-2-LB	Vortex	9.61	9.68	9.69	9.70	9.67	9.62	9.62
KFII-2-LB	MERRA2	9.67	9.72	9.72	9.72	9.70	9.65	9.65
Long-term *WS* for KFII-1-LB		9.70	9.74	9.75	**9.77**	9.74	9.69	9.68
Long-term *WS* for KFII-2-LB		9.64	9.70	9.70	**9.71**	9.69	9.63	9.63

Table A-2: MCP results for the 150 mMSL wind speed time series at the KFII-1-LB and KFII-2-LB locations. The results selected to continue the analysis are highlighted in bold.

The resulting long-term wind speed at 150 mMSL at the KFII-1-LB and KFII-2-LB locations are 9.77 and 9.71 m/s, respectively. These results were obtained as the average of the MCP results in regressions with the two reference datasets shown in Table A-2 for a long-term period of 18 years. The 150 mMSL wind speed and wind direction time series resulting from the MCP analysis with the Vortex time series as a long-term reference has been scaled to the long-term mean wind speed obtained at each FLS location. The decision to use the time series resulting from MCP with the Vortex dataset was taken because:

- The Vortex time series was found to have the best correlation with the FLS measurements, see for instance Figure A-1 for comparisons for KFII-1-LB. Results for KFII-2-LB are consistent with this trend.
- The shape of the wind speed- and direction frequency distributions from the Vortex time series is the most similar to those of the FLS measurements, see Figure A-1 for comparisons for KFII-1-LB. Results for KFII-2-LB are consistent with this trend.
- When comparing the time series resulting from the MCP with their respective short-term measurements over the concurrent period and using the fitted Weibull parameters as metric, the MCP time series obtained using the Vortex time series as long-term reference is consistently found to be the closest to the measurements, see Table A-3.

FLS	MCP time series	*A* FLS	*A* MCP time series	*k* FLS	k MCP time series
		[m/s]	[m/s]	[-]	[-]
KFII-1-LB	VortexKFII1	12.57	12.59	2.32	2.29
	ERA5N03	12.01	11.83	2.40	2.35
	MERRA2N03	10.81	10.46	2.43	2.31
KFII-2-LB	VortexKFII2	12.53	12.41	2.31	2.34
	ERA5N03	11.94	11.70	2.37	2.34
	MERRA2N03	10.61	10.32	2.42	2.29

Table A-3: Weibull parameters from the measurements of the FLSs deployed within Kriegers Flak II and MCP time series obtained when using different long-term reference time series.

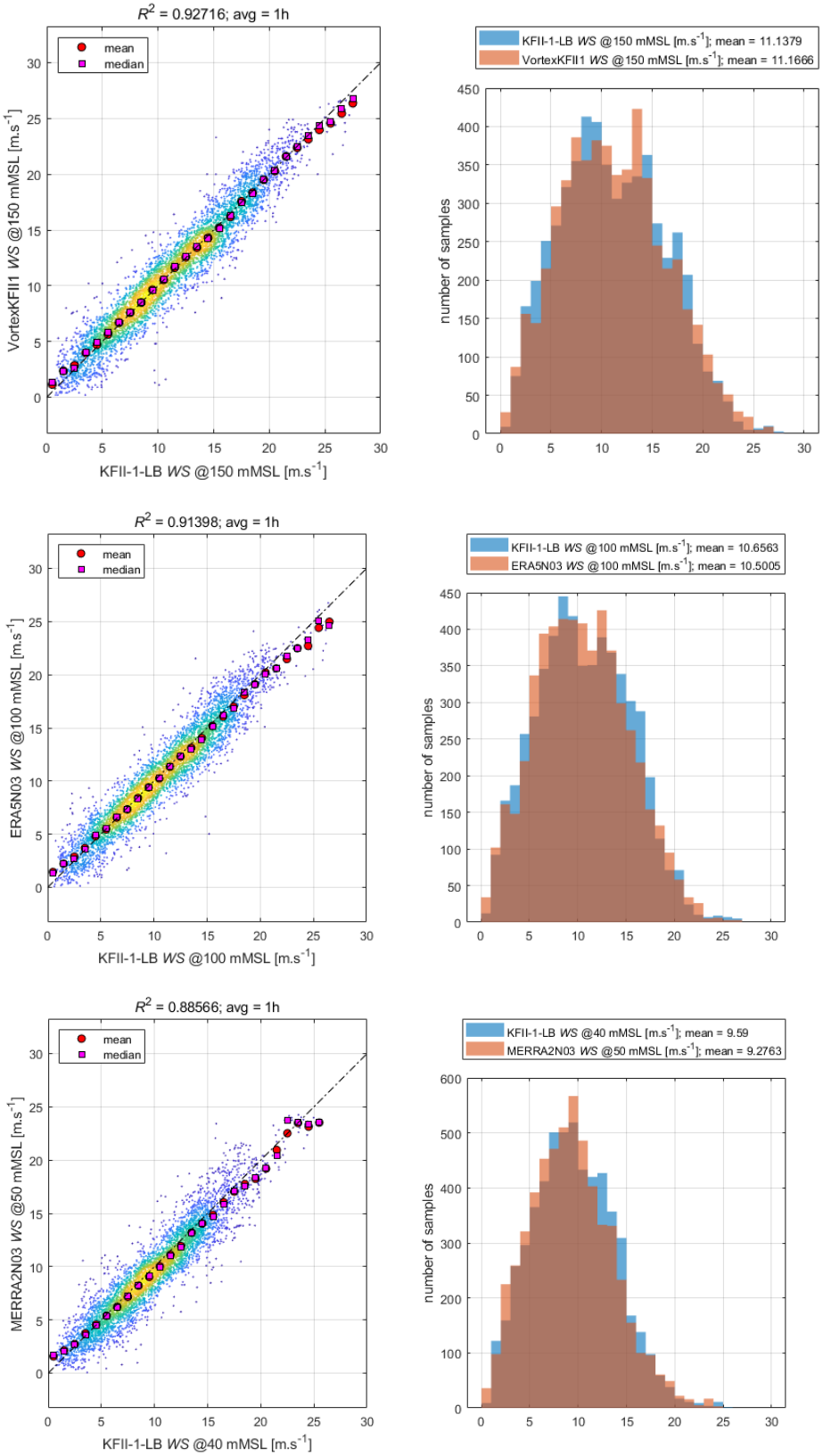

Figure A-1: Wind speed scatter plot (left) and histogram (right) of the FLS measurements and three candidate long-term reference time series (top: Vortex, middle: ERA5, bottom: MERRA2) for KFII-1-LB.

A.2 Horizontal extrapolation to the analysis points location

The long-term wind climates derived in the previous section need to be extrapolated to the analysis points derived in Section 5. Speed-up factors derived from analysis of the NORA3, NEWA and GWA datasets are considered for this purpose, first assessing their performance using the following methodology:

A. The long-term mean wind speeds estimated for the KFII-1-LB and KFII-2-LB, together with long-term estimates at KFII-3-LB, BHI-1-LB and BHII-1-LB (obtained with the same approach) were taken as a starting point, and the speed-up factors between the different pairs of long-term wind speeds were used as reference speed-up factors.
B. The speed-up factors between the different pairs of locations as predicted by the NORA3, NEWA and GWA datasets were calculated.
C. The speed-up factors estimated in the two steps above were compared to assess the ability of the different spatial datasets to predict the observed values.

Results from the evaluation of spatial datasets are shown in Table A-4. NORA3 was the dataset which best replicates the wind speed-up factor from the long-term corrected KFII-1-LB, KFII-2-LB, KFII-3-LB, BHI-1-LB and BHII-1-LB measurements, and was therefore chosen as basis for the horizontal extrapolation of the long-term wind climate. Comparing the model-based speed up factors with those derived from measurements, the NORA3 dataset is found to have the best performance, with an RMSE of approximately 1.3%.

MCP WS@150 mMSL				
From \ To	KFII-1-LB	KFII-2-LB	BHI-1-LB	BHII-1-LB
KFII-1-LB	-	0.9959	1.0237	1.0218
KFII-2-LB	1.0041	-	1.0279	1.0260
KFII-3-LB	1.0019	0.9978	1.0256	1.0237
BHI-1-LB	0.9769	0.9728	-	0.9981
BHII-1-LB	0.9787	0.9747	1.0019	-

GWA WS@150 mMSL				
From \ To	KFII-1-LB	KFII-2-LB	BHI-1-LB	BHII-1-LB
KFII-1-LB	-	1.0062	0.9869	0.9836
KFII-2-LB	0.9938	-	0.9808	0.9775
KFII-3-LB	0.9956	1.0018	0.9826	0.9793
BHI-1-LB	1.0133	1.0196	-	0.9967
BHII-1-LB	1.0167	1.0230	1.0033	-

NORA3 WS@100 mMSL				
From \ To	KFII-1-LB	KFII-2-LB	BHI-1-LB	BHII-1-LB
KFII-1-LB	-	0.9765	1.0095	1.0049
KFII-2-LB	1.0240	-	1.0337	1.0290
KFII-3-LB	1.0052	0.9816	1.0147	1.0100
BHI-1-LB	0.9906	0.9674	-	0.9954
BHII-1-LB	0.9952	0.9718	1.0046	-

NEWA WS@150 mMSL				
Meas From \ To	KFII-1-LB	KFII-2-LB	BHI-1-LB	BHII-1-LB
KFII-1-LB	-	0.9816	1.0038	1.0019
KFII-2-LB	1.0188	-	1.0227	1.0207
KFII-3-LB	1.0023	0.9839	1.0062	1.0042
BHI-1-LB	0.9962	0.9778	-	0.9980
BHII-1-LB	0.9981	0.9797	1.0020	-

Table A-4: Speed-up factors between pairs of locations involving KFII-1-LB, KFII-2-LB, BHI-1-LB and BHII-1-LB. The **top-left** table shows the speed-up factors resulting from the long-term corrected measurements. The **top-right** table shows the speed-up factors from GWA, the **bottom-left** table shows the speed-up factors from NORA3 and the **bottom-right** table shows the speed-up factors from NEWA.

Finally, the wind climate at each of the analysis points was estimated as follows:

1) The wind climate estimated at the KFII-1-LB location was rescaled using the speed-up factor from NORA3 that represents the variation of wind speed between KFII-1-LB and the analysis points located at the southern sub-area of KFII.

2) The wind climate estimated at the KFII-2-LB location was rescaled using the speed-up factor from NORA3 that represents the variation of wind speed between KFII-2-LB and the analysis points located at the northern sub-area of KFII.

A.3 Summary of Weibull parameters

The resulting wind speed distributions and Weibull parameters estimated at each of the analysis points and at the two main FLSs are illustrated in Figure A-2 and summarised in Table A-5.

Site	Point	A	k	Mean wind speed
		[m/s]	[-]	[m/s]
North	P1	11.13	2.199	9.89
South	P2	11.01	2.173	9.79
KFII-1-LB		10.99	2.173	9.73
KFII-2-LB		10.93	2.199	9.68

Table A-5: Weibull parameters estimated at the analysis points.

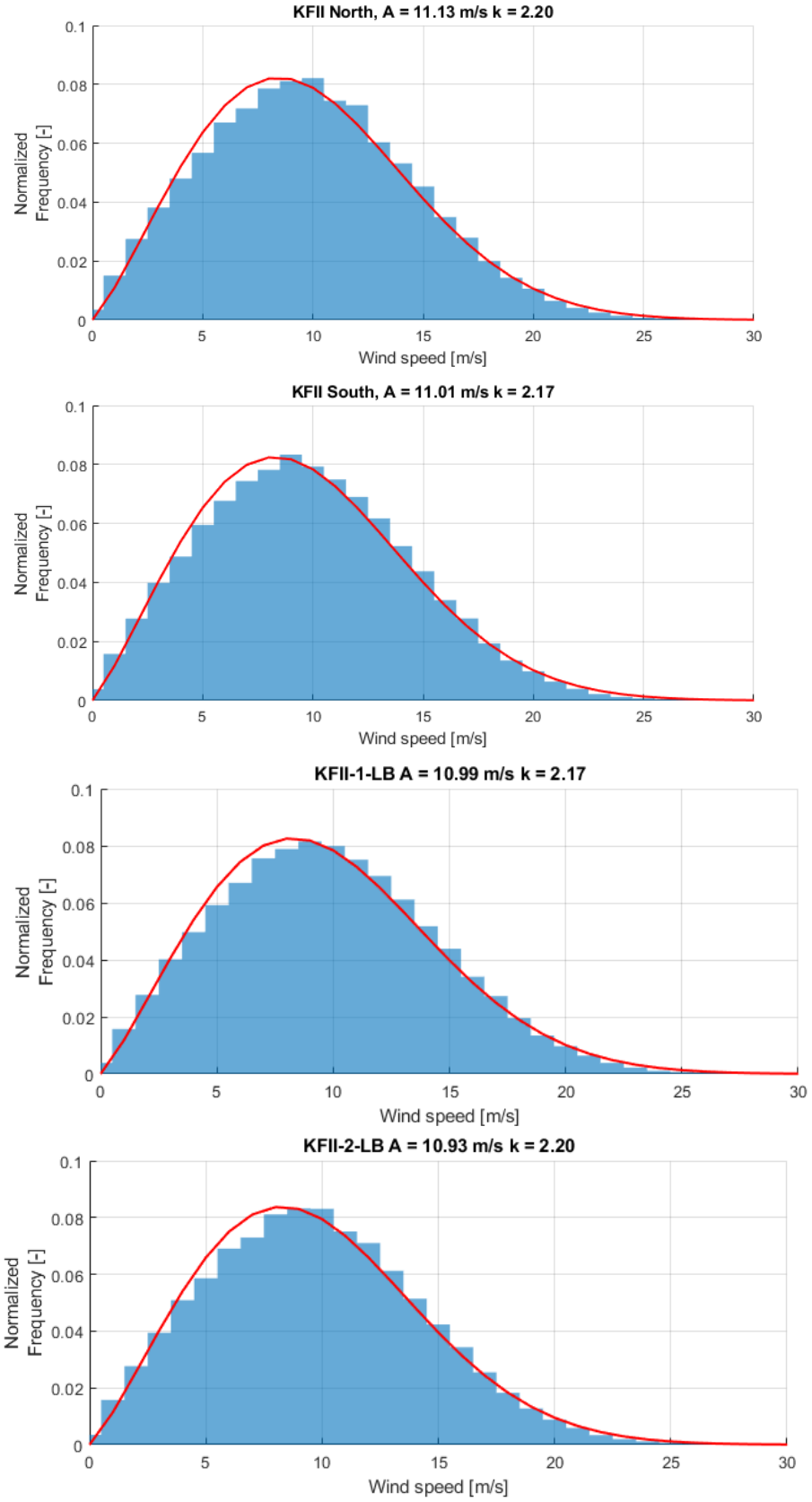

Figure A-2: Wind speed histogram of the wind climate estimated at each of the analysis points.

Appendix B. Description of Wind Measurement Datasets

B.1 Kriegers Flak II FLS measurement campaign

The ongoing metocean surveys for the development of five offshore wind project areas within the Danish exclusive economic zone include measurements at two locations within the KFII North and at one location within KFII South areas using floating LiDAR Systems (FLS), as shown in Figure B-1. The measurement campaign was carried out by Fugro, and it started on the 3rd of September 2023 when a Fugro Seawatch Wind LiDAR (SWLB) buoy was deployed at FLSII North and KFII South FLS measurement locations. The measurement campaign is planned to last for 12 months with the option of being extended [DOW30PEPL2]. A second SWLB was deployed at FLSII North on the 1st of November 2023, and it is expected that the measurements collected at this location will cover a short period of time [DOW30PEPL2]. In this report, the measurement locations within KFII South and KFII North with start date of 2023-09-03 are referred to as KFII-1-LB and KFII-2-LB respectively, while the second measurement location within KFII North is referred to as KFII-3-LB. At each location, a primary SWLB unit has been deployed as summarised in Table B-1, with an additional unit named SWLB085 being available as a spare unit to be deployed in case one of the primary SWLBs encounters problems. As mentioned in the monthly report for month #5 in [DOW30MR], the spare buoy was deployed in KFII-2-LB, replacing WS172. The reason for this replacement was that the Lidar unit on WS172 presented a potential lidar wedge motor failure and stopped collecting measurements on 2023-12-24. According to monthly report #7 in [DOW30MR], buoy WS190 was swapped with buoy WS172 on 2024-02-16, as Lidar measurements collected were interrupted on 2024-02-12 due to a problem with the fuel supply.

The coordinates of the FLSs deployed at Kriegers Flak II are summarised in Table B-1.

FLS location	Primary SWLB unit	Latitude [°N]	Longitude [°E]
KFII-1-LB	WS190	54.9168	12.9945
KFII-2-LB	WS172	55.2156	12.6986
KFII-3-LB	WS210	55.1348	12.8681

Table B-1: Coordinates of the FLS measurement locations within KFII South and KFII North. Reproduced from Table 2.1 of [DOW30PEPL2]. Please note that, as described in Section B.1.3, a given position may have been served by more than one SWLB unit. CRS: WGS84.

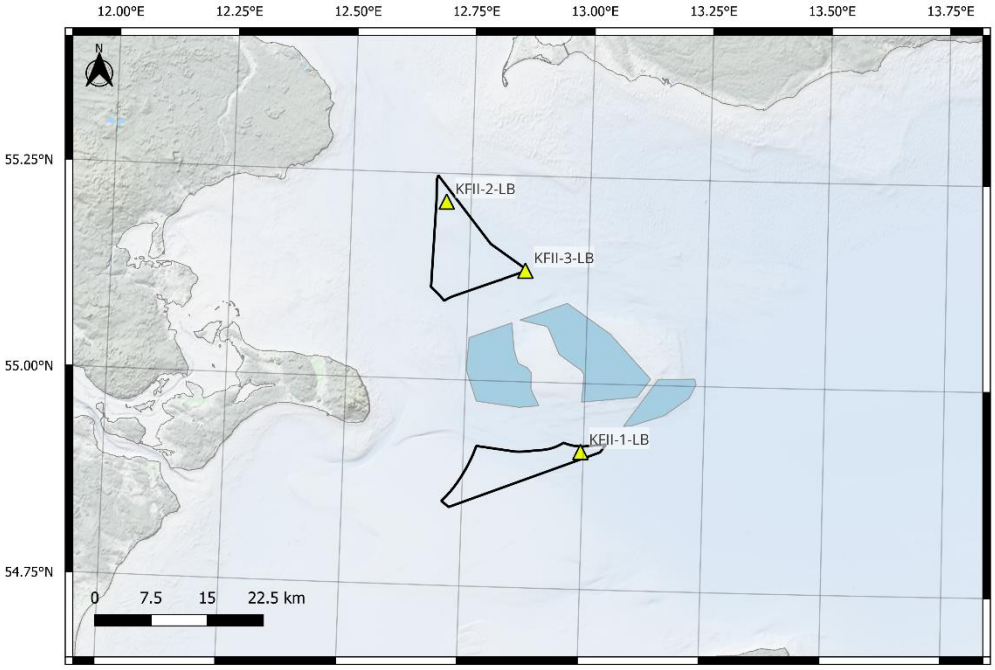

Figure B-1: Deployment location of the three FLSs deployed within KFII South and KFII North.

B.1.1 Instrumentation setup

A list of all instruments installed on each of the FLSs deployed at Kriegers Flak II is shown in Table B-2. All reports, data and calibration certificates were shared by the Client in [SHAREP]. Table B-2 has been compiled by C2Wind from the information in the project execution plan [DOW30PEPL2], project measurement plan [DOW30PMP], deployment record [DOW30DR], as well as monthly- [DOW30MR] and service reports [DOW30SR].

Parameters	Instrument	Serial Number	Calibration certificate
WS172			
Wind speed & direction	ZX Lidars ZX300M	ZX709 ZX757	[ZX709] [ZX757]
Wind speed & direction	Gill Instruments 1405-PK-300	20120010	Y*
Wave parameters	Fugro Oceanor Wavesense 3.2	406	Y
Current profile & water temp.	Nortek Signature500	12612 18050	Y N
Air temp. & humidity	Vaisala HMP155	S0510182	Y
Air pressure	Vaisala PTB330	PTB330	Y
Precipitation	Young 50203	3043	Y
Visibility (fog)	Optical Sensors Sweden MiniOFS	93	Y*
Water level	Thelma Biotel ADT-HP16_v3.0	047I 0055	Y*
Position	Iridium 9602	03043	N/A
Position	Septentrio DualGPS AsteRx4	181014 3034943	N/A N/A
Motions	Fugro LMCU	2319-00105	N/A
WS190			
Wind speed & direction	ZX Lidars ZX300M	ZX809	[ZX809]
Wind speed & direction	Gill Instruments 1405-PK-300	22290121	Y*
Wave parameters	Fugro Oceanor Wavesense 3.2	482	Y
Current profile & water temp.	Nortek Signature500	12679	Y
Air temp. & humidity	Vaisala HMP155	U2910243	Y
Air pressure	Vaisala PTB330	V1941358	Y
Precipitation	Young 50203	03042	Y
Visibility (fog)	Netsens MiniOFS	NA	N/A*
Water level	Thelma Biotel ADT-HP16_v3.0	047G-0051	N*
Position	Iridium 9602	J1926G	N/A
Position	Septentrio DualGPS AsteRx4	3034864 181013	N/A
Motions	Fugro LMCU	2319-00103	N/A
WS210			
Wind speed & direction	ZX Lidars ZX300M	ZX1004	[ZX1004]
Wind speed & direction	Gill Instruments 1405-PK-300	20100083	Y*
Wave parameters	Fugro Oceanor Wavesense 3.2	401	Y
Current profile & water temp.	Nortek Signature500	12613	Y
Air temp. & humidity	Vaisala HMP155	V3550580	Y
Air pressure	Vaisala PTB330	K1020021	Y
Precipitation	Young 50203	03041	Y
Visibility (fog)	Optical Sensors Sweden MiniOFS	23242146	Y*
Water level	Thelma Biotel ADT-HP16_v3.0	1938-0109	N/A*
Position	Iridium 9602	J1B9NY	N/A
Position	Septentrio DualGPS AsteRx4	19363057802	N/A
Motions	Fugro LMCU	2324-00114	N/A
SWLB085			
Wind speed & direction	ZX Lidars ZX300M	ZX1915	[ZX1915]
Wind speed & direction	Gill Instruments 1405-PK-300	23100150	Y
Wave parameters	Fugro Oceanor Wavesense	363	Y
Current profile & water temp.	Nortek Signature500	104487	Y
Air temp. & humidity	Vaisala HMP155	V0831110	Y
Air pressure	Vaisala PTB330	V0831804	Y
Precipitation	Young 50203	3027	Y
Visibility (fog)	Optical Sensors Sweden MiniOFS	23080082	Y*
Water level	Thelma Biotel ADT-HP16_v3.0	047I-0055	Y*

Position	Iridium 9602	0033216	N/A
Position	Septentrio DualGPS AsteRx4	23043092749	N/A
Motions	Fugro LMCU	2319-00107	N/A

* While these instruments are listed as having a calibration certificate in [DOW30DR], the documents uploaded to [SHAREP] are either quality certificates or declarations of conformity issued by the instrument manufacturers.

Table B-2: Instruments installed on the different FLS deployed as part of the DOW2030 campaign. The table summarizes the information in [SHAREP], [DOW30PEPL2], [DOW30PMP], [DOW30DR], [DOW30MR] and [DOW30SR].

B.1.2 Data description

The post-processed data from Fugro described in Table 3.3 of the first monthly report in [DOW30MR] were shared with C2Wind by Energinet in [SHAREP]. For KFII-1-LB and KFII-2-LB, all measurements were extracted from 56 files with the following name structure:

- *KFII-N-LB_Mmm_CurrentData.csv*
- *KFII-N-LB_Mmm_MetOceanData.csv*
- *KFII-N-LB_Mmm_Posdata.csv*
- *KFII-N-LB_Mmm_Status.csv*
- *KFII-N-LB_Mmm_WaveData.csv*
- *KFII-N-LB_Mmm_WindSpeedDirectionTI.csv*
- *KFII-N-LB_Mmm_WindStatus.csv*

Where *N* corresponds to the number of the FLS unit as shown in Table B-1, mm is the measurement campaign month number, which at the time of writing this report ranges from 1 (September 2023) to 8 (May 2024). Each post-processed file contains 10-minute statistics, and for the purposes of the analyses in this document, only data found in the following files were used:

- *KFII-N-LB_Mmm_WindSpeedDirectionTI.csv*
- *KFII-N-LB_Mmm_WindStatus.csv*
- *KFII-N-LB_Mmm_MetOceanData.csv*
- *KFII-N-LB_Mmm_Posdata.csv*

In the case of the measurements collected at KFII3, all measurements were extracted from 12 files with the following name structure:

- *KFII-N-LB_Mmm_WindSpeedDirectionTI.csv*
- *KFII-N-LB_Mmm_WindStatus.csv*

The data signals found in the aforementioned post-processed files are listed in Table B-3. The measurements were concatenated in one single file for each FLS. Data found in the file "*Posdata*" type files were used to ensure that all measurements had been collected within the deployment area of each FLS, as shown in Figure B-5.

Header in file	Elevation [mMSL]	Instrument
File type: *KFII- N -LB_Mmm_WindSpeedDirectionTI.csv*		
TIMESTAMP (ISO-8601) UTC		
WindSpeed004m m/s	4	Gill Windsonic M
WindSpeed012m m/s	12	ZephIR ZX300m
WindSpeed040m m/s	40	ZephIR ZX300m
WindSpeed080m m/s	80	ZephIR ZX300m
WindSpeed100m m/s	100	ZephIR ZX300m
WindSpeed130m m/s	130	ZephIR ZX300m
WindSpeed150m m/s	150	ZephIR ZX300m
WindSpeed170m m/s	170	ZephIR ZX300m
WindSpeed190m m/s	190	ZephIR ZX300m
WindSpeed220m m/s	220	ZephIR ZX300m
WindSpeed260m m/s	260	ZephIR ZX300m
WindSpeed300m m/s	300	ZephIR ZX300m
WindDir004m deg	4	Gill Windsonic M
WindDir012m deg	12	ZephIR ZX300m
WindDir040m deg	40	ZephIR ZX300m
WindDir080m deg	80	ZephIR ZX300m
WindDir100m deg	100	ZephIR ZX300m
WindDir130m deg	130	ZephIR ZX300m
WindDir150m deg	150	ZephIR ZX300m
WindDir170m deg	170	ZephIR ZX300m
WindDir190m deg	190	ZephIR ZX300m
WindDir220m deg	220	ZephIR ZX300m
WindDir260m deg	260	ZephIR ZX300m
WindDir300m deg	300	ZephIR ZX300m
turbulence(TI) 012m	12	ZephIR ZX300m
turbulence(TI) 040m	40	ZephIR ZX300m
turbulence(TI) 080m	80	ZephIR ZX300m
turbulence(TI) 100m	100	ZephIR ZX300m
turbulence(TI) 130m	130	ZephIR ZX300m
turbulence(TI) 150m	150	ZephIR ZX300m
turbulence(TI) 170m	170	ZephIR ZX300m
turbulence(TI) 190m	190	ZephIR ZX300m
turbulence(TI) 220m	220	ZephIR ZX300m
turbulence(TI) 260m	260	ZephIR ZX300m
turbulence(TI) 300m	300	ZephIR ZX300m
File type: *KFII- N -LB_Mmm_WindStatus.csv*		
TIMESTAMP (ISO-8601) UTC		
liPacketCount012m	12	ZephIR ZX300m
liPacketCount040m	40	ZephIR ZX300m
liPacketCount080m	80	ZephIR ZX300m
liPacketCount100m	100	ZephIR ZX300m
liPacketCount130m	130	ZephIR ZX300m
liPacketCount150m	150	ZephIR ZX300m
liPacketCount170m	170	ZephIR ZX300m
liPacketCount190m	190	ZephIR ZX300m
liPacketCount220m	220	ZephIR ZX300m
liPacketCount260m	260	ZephIR ZX300m
liPacketCount300m	300	ZephIR ZX300m
File type: *KFII- N -LB_Mmm_MetOceanData.csv*		
TIMESTAMP (ISO-8601) UTC		
AirHumidity %	4.1	Vaisala HMP155
AirTemperature C	4.1	Vaisala HMP155
AirPressure hPa	0	Vaisala PTB330A
adcp_temperature deg C	0	Nortek Signature500
File type: *KFII- N -LB_Mmm_Posdata.csv*		
TIMESTAMP (ISO-8601) UTC		
irLatitude deg		Iridium 9602
irLongitude deg		Iridium 9602
spLatitude deg		Septentrio DualGPS
spLongitude deg		Septentrio DualGPS

Table B-3: Data signals used in the analyses in this report, found in the post-processed files from Fugro.

B.1.3 Data availability

The FLS measurements collected at Kriegers Flak II are available for the following periods:

- KFII-1-LB: From 2023-09-03 17:00:00 to 2024-05-03 16:40:00
- KFII-2-LB: From 2023-09-03 11:40:00 to 2024-05-03 11:20:00
- KFII-3-LB: From 2023-11-01 16:10:00 to 2024-04-14 03:20:00

The monthly data availability of all three FLSs is summarised in Table B-4. From the data in the table and a high-level analysis of the measurements, the most significant data gaps identified are:

- KFII-1-LB:
  - Wind speed- and direction from the LiDAR device between 2024-02-12 and 2024-02-16: According to Table A-1 of the monthly report of month 6 in [DOW30MR], this gap was due to low input power. The data gap was resolved with the swap of buoy WS190 with WS172 on 2024-02-16.
- KFII-2-LB:
  - Wind speed- and direction from the LiDAR device between 2023-12-24 and 2024-01-16: According to monthly reports #4 and #5 in [DOW30MR] and gap report #1 [DOW30GR], LiDAR unit ZX709 presented a problem in its wedge motor and no measurements were collected during this period. This problem was resolved when spare buoy SWLB085 was deployed at KFII-2-LB and buoy WS172 was recovered. LiDAR unit 709 initially installed on buoy WS172 was replaced by LiDAR unit 757.
- KFII-3-LB: No significant data gaps were identified in the measurements available at this location, see Figure B-4.

The data availability of Lidar wind speed and wind direction measurements for all elevations and for the KFII-1-LB and KFII-3-LB is higher than 93%, as shown in Table B-5. Wind speed and direction data availability of KFII-2-LB is higher than 86% for all elevations due to the 22-day data gap during the period from 2023-12-24 to 2024-01-16.

FLS	Year	Month	System data availability	*WS* @ 4 mMSL	*WD* @ 4 mMSL	*WS* @ 150 mMSL	*WD* @ 150 mMSL	*T* @ 4.1 mMSL	*RelH* @ 4.1 mMSL	*P* @ 0 mMSL
KFII-1-LB	2023	9	0.9097	0.9088	0.9088	0.8958	0.8958	0.9095	0.9095	0.9083
	2023	10	1.0000	0.9989	0.9991	0.9933	0.9935	0.9998	0.9998	0.9996
	2023	11	1.0000	0.9993	0.9995	0.9817	0.9819	1.0000	1.0000	0.9991
	2023	12	1.0000	0.9993	0.9996	0.9828	0.9830	1.0000	1.0000	0.9993
	2024	1	1.0000	0.9993	0.9996	0.9608	0.9610	1.0000	1.0000	0.9996
	2024	2	1.0000	0.9962	0.9964	0.7859	0.7862	0.9966	0.9966	0.9758
	2024	3	1.0000	0.9984	0.9987	0.9283	0.9285	0.9908	0.9908	0.9830
	2024	4	1.0000	0.9984	0.9986	0.9551	0.9553	0.9988	0.9988	0.9958
	2024	5	0.0871	0.0871	0.0871	0.0871	0.0871	0.0871	0.0871	0.0853
KFII-2-LB	2023	9	0.9171	0.9162	0.9162	0.8928	0.8928	0.9167	0.9167	0.8877
	2023	10	1.0000	0.9989	0.9991	0.9875	0.9877	0.9991	0.9991	0.9859
	2023	11	1.0000	0.9986	0.9988	0.9785	0.9787	0.9993	0.9993	0.9741
	2023	12	1.0000	0.9989	0.9991	0.7511	0.7513	0.9962	0.9962	0.9711
	2024	1	1.0000	0.9982	0.9984	0.4839	0.4841	0.9982	0.9982	0.9935
	2024	2	1.0000	0.9990	0.9993	0.9097	0.9100	0.9983	0.9983	0.9988
	2024	3	1.0000	0.9980	0.9982	0.9297	0.9299	0.9991	0.9991	0.9989
	2024	4	1.0000	0.9993	0.9995	0.9516	0.9519	0.9993	0.9993	0.9993
	2024	5	0.0800	0.0800	0.0800	0.0800	0.0800	0.0800	0.0800	0.0800
KFII-3-LB	2023	11	0.9775	0.9604	0.9604	0.9542	0.9542	N/A	N/A	N/A
	2023	12	1.0000	0.9973	0.9973	0.9879	0.9879	N/A	N/A	N/A
	2024	1	1.0000	0.9512	0.9512	0.9220	0.9220	N/A	N/A	N/A
	2024	2	1.0000	0.9966	0.9966	0.9140	0.9140	N/A	N/A	N/A
	2024	3	1.0000	0.9971	0.9971	0.9332	0.9332	N/A	N/A	N/A
	2024	4	0.4382	0.4359	0.4359	0.3963	0.3963	N/A	N/A	N/A

Table B-4: Monthly data availability of wind speed and wind direction at 4 and 150 mMSL, as well as surface level air temperature, relative humidity and air pressure for the three FLSs. The data availability cells are colour coded, light green cells indicate data availability between 0.75 and 1, light yellow cells mean data availability is between 0.5 and 0.75, while light orange cells highlight data availability between 0 and 0.5.

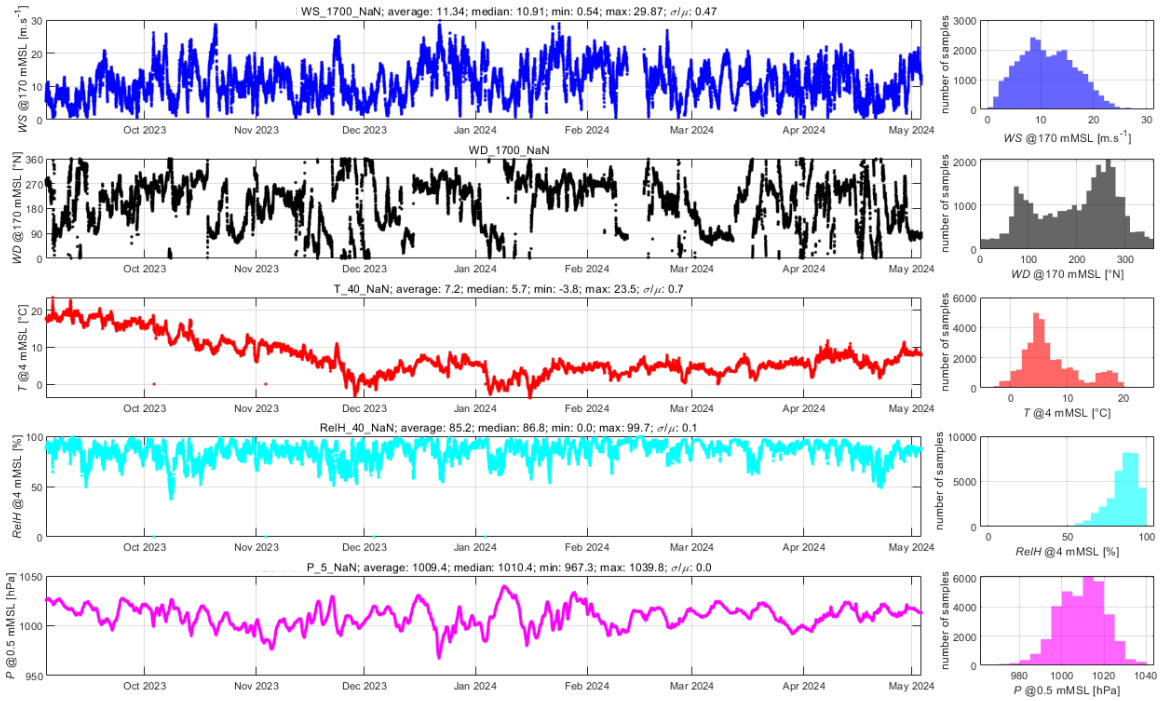

Figure B-2: Time series of wind speed and wind direction at 150 mMSL, as well as surface level air temperature, relative humidity and air pressure collected at KFII-1-LB.

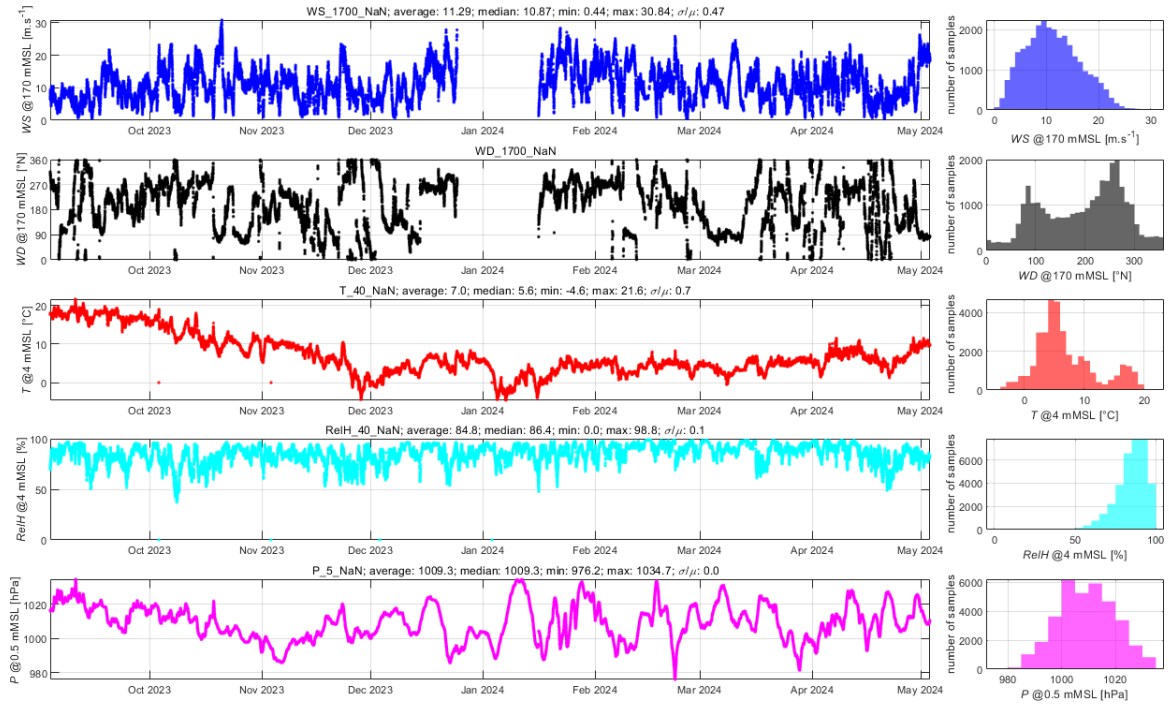

Figure B-3: Time series of wind speed and wind direction at 150 mMSL, as well as surface level air temperature, relative humidity and air pressure collected at KFII-2-LB.

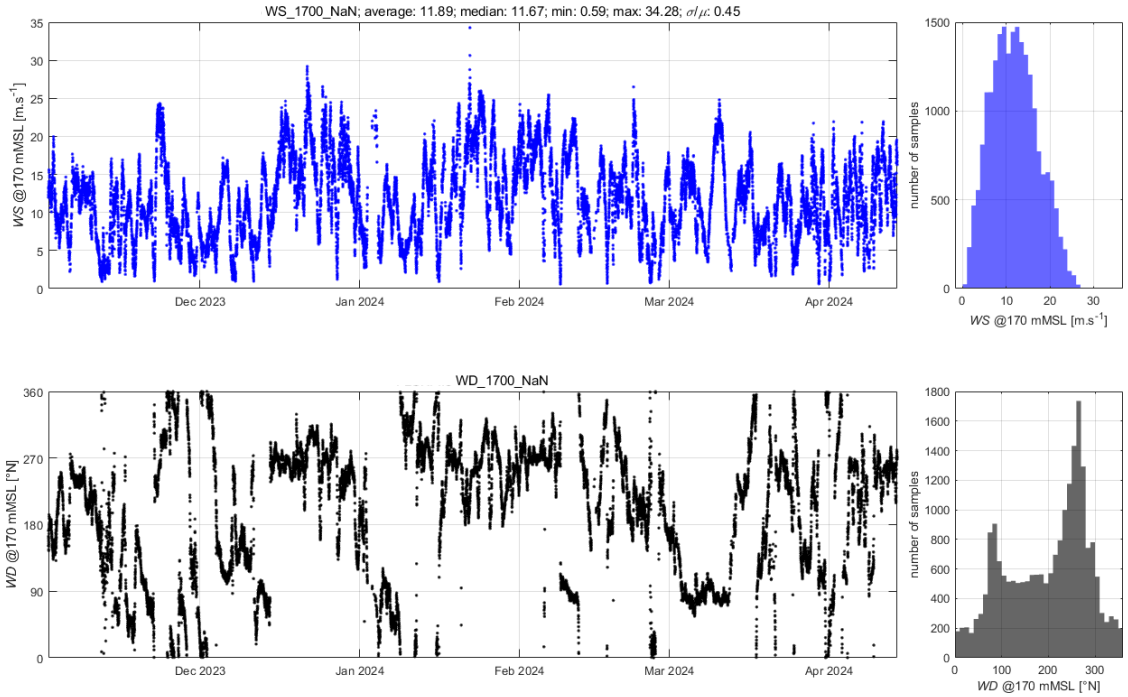

Figure B-4: Time series of wind speed and wind direction at 150 mMSL, as well as surface level air temperature, relative humidity and air pressure collected at KFII-3-LB.

KFII-1-LB			KFII-2-LB			KFII-3-LB		
Elevation [mMSL]	Availability [-]		Elevation [mMSL]	Availability [-]		Elevation [mMSL]	Availability [-]	
	WS	*WD*		*WS*	*WD*		*WS*	*WD*
12	0.9734	0.9736	12	0.8968	0.8970	12	0.9833	0.9833
40	0.9744	0.9746	40	0.9043	0.9045	40	0.9831	0.9831
80	0.9641	0.9643	80	0.8876	0.8878	80	0.9613	0.9613
100	0.9534	0.9536	100	0.8780	0.8782	100	0.9544	0.9544
130	0.9510	0.9512	130	0.8739	0.8741	130	0.9478	0.9478
150	0.9492	0.9494	150	0.8717	0.8719	150	0.9455	0.9455
170	0.9477	0.9479	170	0.8694	0.8696	170	0.9434	0.9434
190	0.9470	0.9472	190	0.8678	0.8680	190	0.9406	0.9406
220	0.9450	0.9452	220	0.8665	0.8667	220	0.9383	0.9383
260	0.9430	0.9432	260	0.8635	0.8637	260	0.9340	0.9340
300	0.9406	0.9408	300	0.8621	0.8623	300	0.9332	0.9332

Table B-5: Data availability of the LiDAR measurements collected by the three FLSs at Kriegers Flak II.

B.1.4 Data reliability and validity

The most critical instruments installed on the SWLB passed their calibration tests, see Table B-2. Those whose calibration certificates were not found in [SHAREP] are either not crucial for the analyses in the present document, or likely simply missing from the data sharing folder rather than non-existent. Since most of the analyses in this document are based on the Lidar measurements, a more detailed description of their validity is provided in this subsection.

Both the Lidar units and the floating Lidar system measurements have been compared against reference measurements prior to deployment:

- The Lidar units have been checked against reference cup anemometer measurements, see [ZX709], [ZX757], [ZX809], [ZX1004] and [ZX1915].
- The floating LiDAR data have been checked against a reference Lidar, see [WS172], [WS190], [WS210] and [SWLB085].

Sections 4.3 of [ZX709], [ZX757], [ZX809], [ZX1004] and [ZX1915] show that for wind speed at the top height in the test (92 m), the mean deviation between the cups and the Lidar ranges from -0.8% to +0.6%. According to Table 5-3 of [WS172], [WS190], [WS210] and [SWLB085], the highest deviations between floating Lidar and reference Lidar mean wind speeds occurred for elevations close to the surface, i.e. between 80 and 40 m above the surface. This is likely due to the reference Lidar being located onshore close to the sea at distances between 480 and 290m from the FLSs and wind conditions when the wind is flowing from land towards the FLSs not being filtered out from the analyses in [WS172], [WS190], [WS210] and [SWLB085]. Table B-6 summarises some of the main results in the pre-deployment validation reports of the Lidar units installed on the SWLBs ([ZX709], [ZX757], [ZX809], [ZX1004] and [ZX1915]) and SWLBs ([ZX709], [ZX757], [ZX809], [ZX1004] and [ZX1915]). Figure B-5 shows the coordinates of all 10-minute statistic measurements from KFII-1-LB, KFII-2-LB and KFII-3-LB, all measurements were collected at a close location to the expected deployment location coordinates.

Elev. [m]	WS ref. [m/s]	WS Lidar [m/s]	Rel. diff. [-]	WS ref. [m/s]	WS Lidar [m/s]	Rel. diff. [%]	WS ref. [m/s]	WS Lidar [m/s]	Rel. diff. [-]	WS ref. [m/s]	WS Lidar [m/s]	Rel. diff. [-]	WS ref. [m/s]	WS Lidar [m/s]	Rel. diff. [-]
	[ZX709]			[ZX757]			[ZX809]			[ZX1004]			[ZX1915]		
92	6.31	6.29	-0.32%	6.68	6.64	-0.60%	6.69	6.71	0.30%	8.05	7.99	-0.75%	8.05	8.01	-0.50%
71	6.05	6.07	0.33%	6.40	6.40	0.00%	6.41	6.45	0.62%	7.68	7.67	-0.13%	7.68	7.68	0.00%
46	5.72	5.74	0.35%	6.07	6.02	-0.82%	6.07	6.08	0.16%	7.19	7.18	-0.14%	7.18	7.19	0.14%
	[WS172]			[WS190]			[WS210]			[SWLB085]					
250	9.39	9.47	0.85%	8.05	8.11	0.75%	10.83	10.76	-0.65%	8.88	8.95	0.79%			
200	9.39	9.44	0.53%	7.89	7.95	0.76%	10.48	10.46	-0.19%	8.84	8.92	0.90%			
180	9.38	9.44	0.64%	7.8	7.84	0.51%	10.39	10.36	-0.29%	8.80	8.88	0.91%			
160	9.34	9.39	0.54%	7.73	7.76	0.39%	10.25	10.22	-0.29%	8.79	8.86	0.80%			
140	9.33	9.37	0.43%	7.64	7.67	0.39%	10.04	10.02	-0.20%	8.74	8.81	0.80%			
120	9.32	9.34	0.21%	7.48	7.53	0.67%	9.83	9.79	-0.41%	8.70	8.77	0.80%			
100	9.23	9.27	0.43%	7.37	7.42	0.68%	9.58	9.53	-0.52%	8.62	8.68	0.70%			
80	9.28	9.23	-0.54%	7.21	7.29	1.11%	9.33	9.29	-0.43%	8.52	8.58	0.70%			
60	9.29	9.28	-0.11%	7.34	7.45	1.50%	8.77	8.73	-0.46%	8.86	8.95	1.02%			
40	9.22	9.22	0.00%	7.11	7.28	2.39%	8.58	8.63	0.58%	8.72	8.82	1.15%			

Table B-6: Mean relative wind speed differences between the Lidar- and floating Lidar measurements, and the reference measurements, from Section 4.3 of [ZX709], [ZX757], [ZX809], [ZX1004] and [ZX1915], as well as Section 5.2 of [WS172], [WS190], [WS210] and [SWLB085]. Apart from the comparison at 40, 60 and 80 mMSL in, where the deviation is likely due to the fact that the reference LiDAR measurements are not located in the marine boundary layer, these comparisons show that the LiDAR measurements are both accurate and precise enough for performing the analysis of this report.

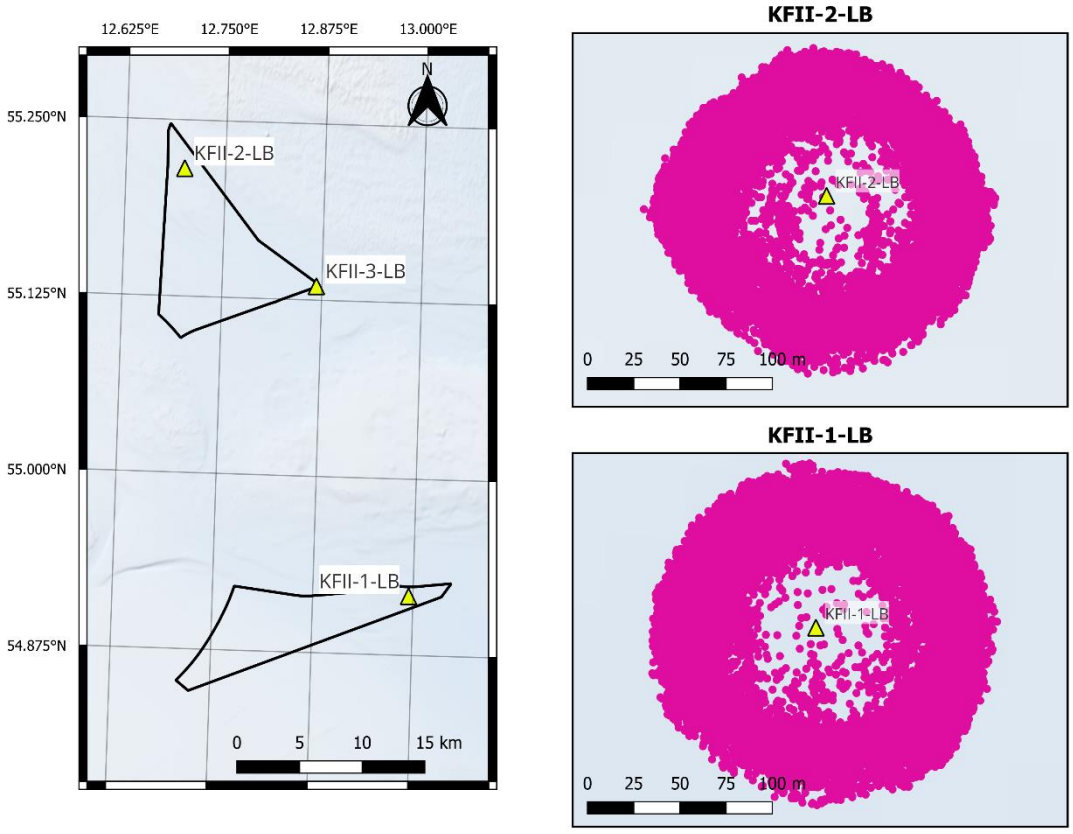

Figure B-5: Coordinates of all 10-minute measurements from KFII-1-LB and KFII-2-LB used in this document. Coordinates for KFII-3-LB were not available. CRS: WGS84.

B.2 Energy Island FLS measurement campaign

The metocean surveys for the development of the Danish Energy Islands included measurements at two locations related to the Energy Island Bornholm, located east of the KFII area, using FLSs as shown in Figure B-6. The two FLS measurement locations within the Energy Island Bornholm project are referred to in this document as BHI-1-LB and BHII-1-LB and their coordinates and locations are shown in Table B-7. The FLS

measurement campaign was carried out by Fugro and consisted of deploying a Fugro Seawatch Lidar Buoy at each measurement location for a duration of at least 1 year with the possibility of extending for one additional year. The FLS measurement campaign at BHII-1-LB lasted two years and covered the period from 2021-11-22 to 2023-11-22. In the case of the measurement campaign at BHI-1-LB, this measurement campaign lasted one year from 2021-11-21 to 2022-11-21.

FLS location	Primary SWLB unit	Latitude [°N]	Longitude [°E]
BHI-1-LB	SW199	54.9948	14.3556
BHII-1-LB	SWLB44	54.7170	14.5882

Table B-7: Coordinates of the FLS measurement locations at BHI-1-LB and BHII-1-LB obtained from Table 1-1 of [EIFMRL3] and [EIFMRL4] respectively. CRS: WGS84.

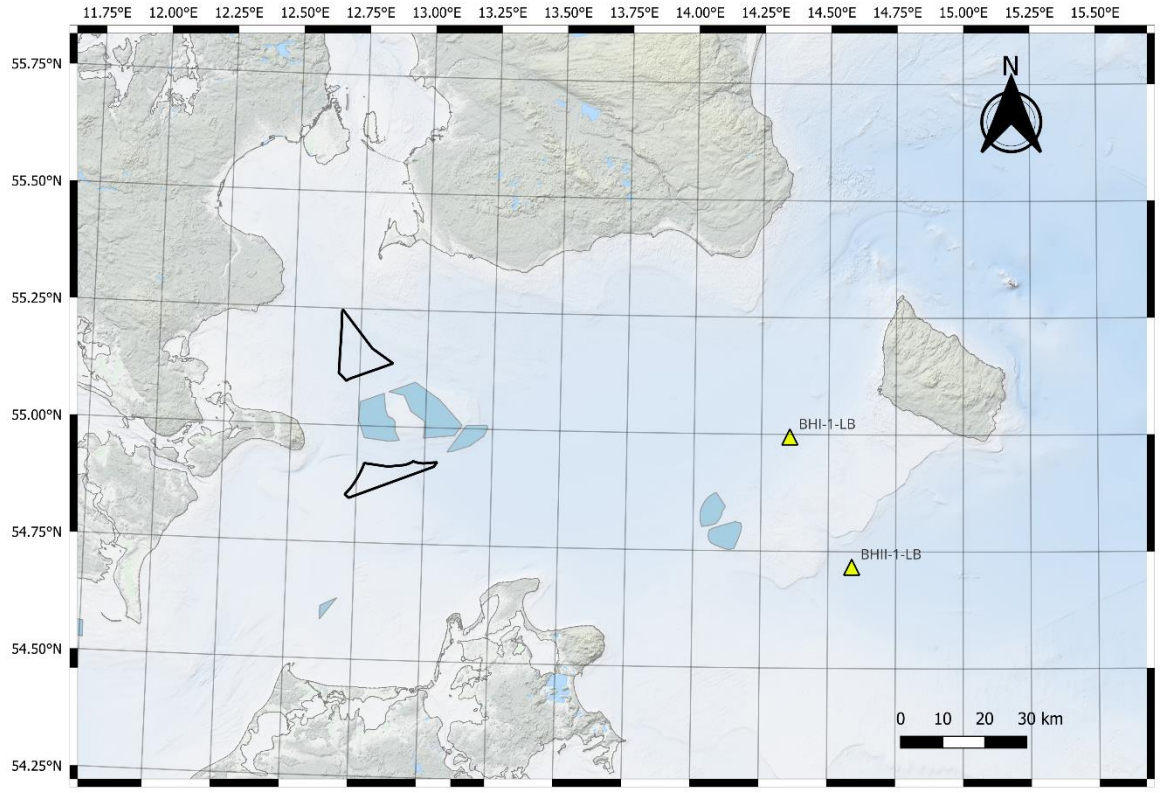

Figure B-6: Deployment locations of the Energy Island Bornholm FLSs relative to the KFII area and OWFs in operation (blue polygons). CRS: WGS84.

B.2.1 Instrumentation setup

As specified in Table 2-1 of [EIPMP], buoys SW199 and SWLB44 were equipped with the same type of instruments as shown in Table B-2. Information regarding the specific serial numbers and calibration certificates, akin to that in Table B-2, is available through [EIBSDR]. The performance verification reports for units SW199 and SWLB44 show similar results as the ones of the DOW2030 campaign.

B.2.2 Data description

The post-processed data from Fugro as described in Table 5-4 of [EIPMP] were shared with C2Wind. Only data containing LiDAR measurements, in addition to other relevant

metocean measurements, were used in this document. These measurements were found in files with the following name structure:

- *Energinet_LotN_SWLB_YYYYMMDD Monthname Year WindSpeedDirectionTI.csv*
- *Energinet_LotN_SWLB_YYYYMMDD Monthname Year WindStatus.csv*
- *Energinet_LotN_SWLB_YYYYMMDD Monthname Year MetOceanData.csv*
- *Energinet_LotN_SWLB_YYYYMMDD Monthname Year Posdata.csv*

Where *N* corresponds to the Lot number (3 and 4 for Energy Island Bornholm), the date components *YYYY*, *MM*, and *DD* are understood by C2Wind to denote the creation date of the post-processed file, and finally *Monthname* and *Year* correspond to the month and year in which the file ends, since each .csv data file contains data from the 21st day of the previous month to the 21st day of *Monthname* for BHI-1-LB. In case of BHII-1-LB each .csv data file contains data from the 22nd day of the previous month to the 22nd day of *Monthname*.

The data signals found in the aforementioned post-processed files are described in Table B-8, all these measurements were concatenated into one single file for each FLS. Note that the measurement elevations are not identical to those for the KFII FLSs listed in Table B-3. Data found in "*Posdata*" files were used to ensure that the measurements available at all timestamps were collected at their expected location.

Header in file	Elevation [mMSL]	Instrument
File type: *WindSpeedDirectionTI.csv*		
TIMESTAMP (ISO-8601) UTC		
WindSpeed004m m/s	4	Gill Windsonic M
WindSpeed030m m/s	30	ZephIR ZX300m
WindSpeed040m m/s	40	ZephIR ZX300m
WindSpeed060m m/s	60	ZephIR ZX300m
WindSpeed090m m/s	90	ZephIR ZX300m
WindSpeed100m m/s	100	ZephIR ZX300m
WindSpeed120m m/s	120	ZephIR ZX300m
WindSpeed150m m/s	150	ZephIR ZX300m
WindSpeed180m m/s	180	ZephIR ZX300m
WindSpeed200m m/s	200	ZephIR ZX300m
WindSpeed240m m/s	240	ZephIR ZX300m
WindSpeed270m m/s	270	ZephIR ZX300m
WindDir004m deg	4	Gill Windsonic M
WindDir030m deg	30	ZephIR ZX300m
WindDir040m deg	40	ZephIR ZX300m
WindDir060m deg	60	ZephIR ZX300m
WindDir090m deg	90	ZephIR ZX300m
WindDir100m deg	100	ZephIR ZX300m
WindDir120m deg	120	ZephIR ZX300m
WindDir150m deg	150	ZephIR ZX300m
WindDir180m deg	180	ZephIR ZX300m
WindDir200m deg	200	ZephIR ZX300m
WindDir240m deg	240	ZephIR ZX300m
WindDir270m deg	270	ZephIR ZX300m
turbulence(TI)030m	30	ZephIR ZX300m
turbulence(TI)040m	40	ZephIR ZX300m
turbulence(TI)060m	60	ZephIR ZX300m
turbulence(TI)090m	90	ZephIR ZX300m
turbulence(TI)100m	100	ZephIR ZX300m
turbulence(TI)120m	120	ZephIR ZX300m
turbulence(TI)150m	150	ZephIR ZX300m
turbulence(TI)180m	180	ZephIR ZX300m
turbulence(TI)200m	200	ZephIR ZX300m
turbulence(TI)240m	240	ZephIR ZX300m
turbulence(TI)270m	270	ZephIR ZX300m
File type: *WindStatus.csv*		
TIMESTAMP (ISO-8601) UTC		
liPacketCount030m	30	ZephIR ZX300m
liPacketCount040m	40	ZephIR ZX300m
liPacketCount060m	60	ZephIR ZX300m
liPacketCount090m	90	ZephIR ZX300m
liPacketCount100m	100	ZephIR ZX300m
liPacketCount120m	120	ZephIR ZX300m
liPacketCount150m	150	ZephIR ZX300m
liPacketCount180m	180	ZephIR ZX300m
liPacketCount200m	200	ZephIR ZX300m
liPacketCount240m	240	ZephIR ZX300m
liPacketCount270m	270	ZephIR ZX300m
File type: *MetOceanData.csv*		
TIMESTAMP (ISO-8601) UTC		
AirHumidity %	4	Vaisala HMP155
AirPressure hPa	2	Vaisala HMP155
AirTemperature C	4	Vaisala PTB330A
WaterTemp001 degC	-1	Nortek Signature500
File type: *Posdata.csv*		
TIMESTAMP (ISO-8601) UTC		
irLatitude deg		Iridium 9602
irLongitude deg		Iridium 9602
spLatitude deg		Septentrio DualGPS
spLongitude deg		Septentrio DualGPS

Table B-8: Data signals used in the analyses in this report, found in the post-processed files from Fugro.

B.2.3 Data availability

The FLS measurements collected at BHI-1-LB and BHII-1-LB are available for the following periods:

- BHI-1-LB: From 2021-11-21 16:00:00 to 2022-11-21 16:00:00
- BHII-1-LB: From 2021-11-22 16:00:00 to 2023-11-22 16:00:00

A summary of the main events that affected the data availability of the FLS measurements can be found in Table B-9. The table offers a condensed version of the event logs of the measurement campaign in [EIFMRL3] and [EIFMRL4] (Appendix A), focusing only on the key instruments for the purposes of the present document (namely Lidars, position and data transmission). Additionally, the data availability of the measurements is summarised in Table B-10 and Table B-11.

The data availability of the LiDAR measurements collected at BHI-1-LB is higher than for the measurements collected at BHII-1-LB. In the case of BHI-1-LB, the data availability of the LiDAR measurements varies between 95.1% and 99.1% over the measurement period, while the data availability for BHII-1-LB varies between 89.2% and 92.2%.

Active FLS	From	To	Description
BHI-1-LB			
SW199	2022-06-20	2022-06-22	SW199 was recovered for service, data download and refuelling. No measurements were collected during this period
BHII-1-LB			
SWLB44	2022-06-22	2022-06-24	SWLB44 was recovered for service, data download and refuelling. No measurements were collected during this period
SWLB44	2022-12-16	2021-01-20	SWLB44 was recovered for service, data download and refuelling. No measurements were collected during this period
SWLB44	2023-08-14	2023-08-17	SWLB44 was recovered for service, data download and refuelling. No measurements were collected during this period

Table B-9: Description of the events impacting data availability for the FLS measurement campaign at Energy Island Bornholm.

FLS	Year	Month	System data availability	*WS* @ 4 mMSL	*WD* @ 4 mMSL	*WS* @ 150 mMSL	*WD* @ 150 mMSL	*T* @ 4.1 mMSL	*RelH* @ 4.1 mMSL	*P* @ 0 mMSL
BHI-1-LB	2021	11	0.3111	0.3109	0.3109	0.3090	0.3090	0.3111	0.3111	0.3111
	2021	12	1.0000	0.9996	0.9996	0.9160	0.9160	0.9998	0.9998	1.0000
	2022	1	1.0000	0.9993	0.9993	0.9366	0.9366	0.9944	0.9944	1.0000
	2022	2	1.0000	0.9995	0.9995	0.9901	0.9901	1.0000	1.0000	1.0000
	2022	3	1.0000	0.9993	0.9993	0.9131	0.9131	0.9984	0.9984	0.9973
	2022	4	1.0000	0.9993	0.9993	0.9752	0.9752	1.0000	1.0000	0.9972
	2022	5	1.0000	0.9991	0.9991	0.9877	0.9877	1.0000	1.0000	0.9964
	2022	6	1.0000	0.9296	0.9296	0.9275	0.9275	0.9301	0.9301	0.9294
	2022	7	1.0000	0.9996	0.9996	0.9861	0.9861	1.0000	1.0000	0.9980
	2022	8	1.0000	0.9996	0.9996	0.9872	0.9872	1.0000	1.0000	0.9973
	2022	9	1.0000	0.9993	0.9993	0.9769	0.9769	1.0000	1.0000	0.9956
	2022	10	1.0000	0.9993	0.9993	0.9400	0.9400	1.0000	1.0000	1.0000
	2022	11	0.6891	0.6889	0.6889	0.6461	0.6461	0.6887	0.6887	0.6891
BHII-1-LB	2021	11	0.2778	0.2775	0.2775	0.2771	0.2771	0.2778	0.2778	0.2778
	2021	12	1.0000	0.9996	0.9996	0.9176	0.9176	0.9989	0.9989	0.9993
	2022	1	1.0000	0.9996	0.9996	0.9297	0.9297	0.9971	0.9971	1.0000
	2022	2	1.0000	0.9993	0.9993	0.9231	0.9231	1.0000	1.0000	1.0000
	2022	3	1.0000	0.9993	0.9993	0.9012	0.9012	1.0000	1.0000	0.9998
	2022	4	1.0000	0.9995	0.9995	0.9613	0.9613	1.0000	1.0000	0.9986
	2022	5	1.0000	0.9993	0.9993	0.9736	0.9736	0.9998	0.9998	0.9991
	2022	6	1.0000	0.9377	0.9377	0.9313	0.9313	0.9384	0.9384	0.9373
	2022	7	1.0000	0.9996	0.9996	0.9901	0.9901	1.0000	1.0000	0.9984
	2022	8	1.0000	0.9996	0.9996	0.9951	0.9951	1.0000	1.0000	0.9989
	2022	9	1.0000	0.9993	0.9993	0.9977	0.9977	1.0000	1.0000	0.9979
	2022	10	1.0000	0.9989	0.9989	0.9639	0.9639	0.9996	0.9996	1.0000
	2022	11	1.0000	0.9995	0.9995	0.9146	0.9146	0.9998	0.9998	1.0000
	2022	12	1.0000	0.4899	0.4899	0.1575	0.1575	0.4901	0.4901	0.4901
	2023	1	1.0000	0.3593	0.3593	0.3562	0.3562	0.3595	0.3595	0.3595
	2023	2	1.0000	0.9995	0.9995	0.9501	0.9501	0.9998	0.9998	0.9998
	2023	3	1.0000	0.9996	0.9996	0.9377	0.9377	1.0000	1.0000	1.0000
	2023	4	1.0000	0.9993	0.9993	0.9824	0.9824	1.0000	1.0000	0.9988
	2023	5	1.0000	0.9996	0.9996	1.0000	1.0000	0.9998	0.9998	0.9975
	2023	6	1.0000	0.9995	0.9995	0.9954	0.9954	1.0000	1.0000	0.9975
	2023	7	1.0000	0.9993	0.9993	0.9982	0.9982	1.0000	1.0000	0.9993
	2023	8	1.0000	0.8992	0.8992	0.8651	0.8651	0.8331	0.8331	0.8985
	2023	9	1.0000	0.9991	0.9991	0.9775	0.9775	0.6433	0.6433	0.9993
	2023	10	1.0000	0.9996	0.9996	0.9922	0.9922	0.8347	0.8347	0.9998
	2023	11	0.7225	0.7222	0.7222	0.7174	0.7174	0.5949	0.5949	0.7218

Table B-10: Monthly data availability of wind speed and wind direction at 4 and 150 mMSL, as well as surface level air temperature, relative humidity and air pressure measured at BHI-1-LB and BHII-1-LB. The data availability cells are colour coded, light green cells indicate data availability between 0.75 and 1, light yellow cells mean data availability is between 0.5 and 0.75, while light orange cells highlight data availability between 0 and 0.5. Please note that the low availability numbers for the first- and last month are in part due to the campaign starting- and ending on the 21st and 22nd of the month for BHI-1-LB and BHII-1-LB respectively.

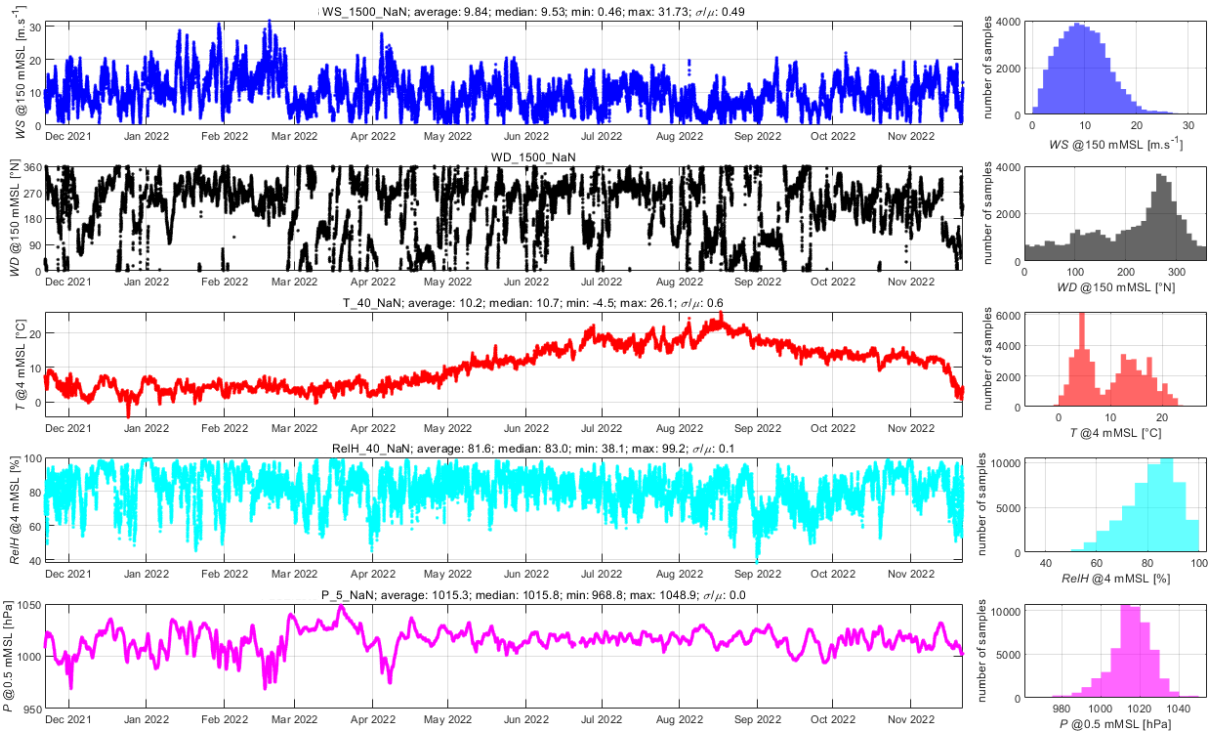

Figure B-7: Time series of wind speed and wind direction at 150 mMSL, air temperature, relative humidity and air pressure collected at BHI-1-LB.

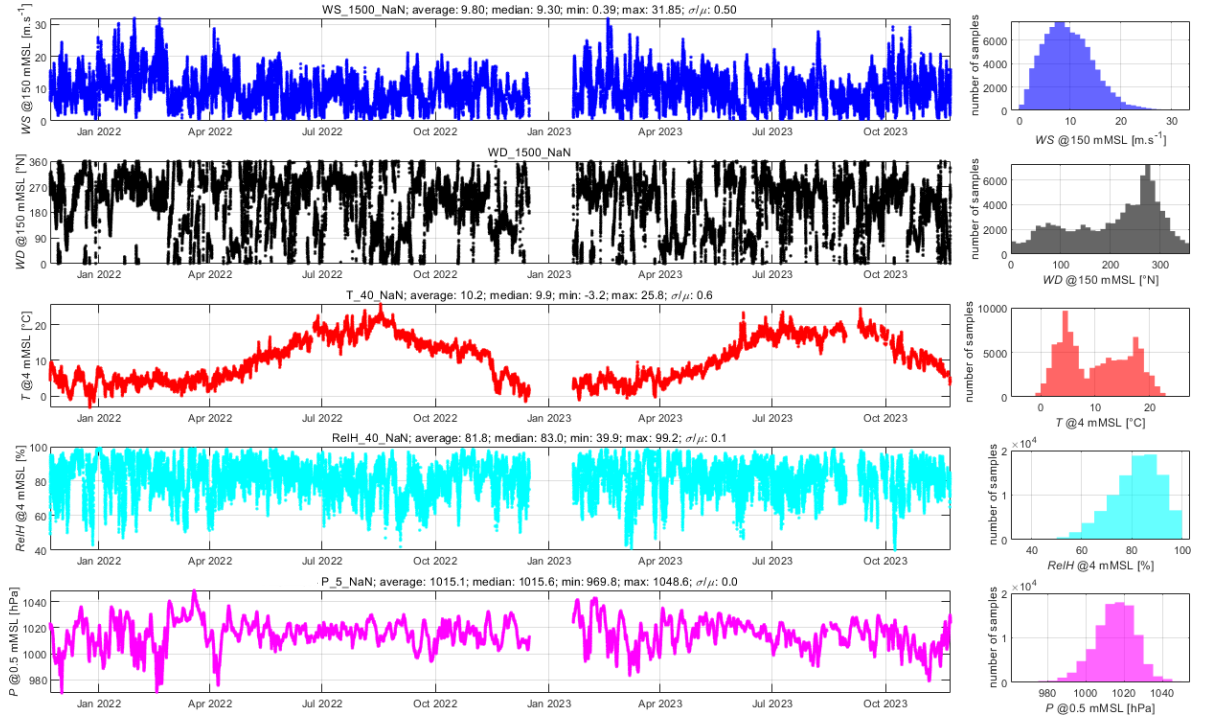

Figure B-8: Time series of wind speed and wind direction at 150 mMSL, air temperature, relative humidity and air pressure collected at BHII-1-LB.

BHI-1-LB			BHII-1-LB		
Elevation [mMSL]	Availability [-]		Elevation [mMSL]	Availability [-]	
	WS	*WD*		*WS*	*WD*
30	0.9902	0.9902	30	0.9216	0.9216
40	0.9911	0.9911	40	0.9225	0.9225
60	0.9894	0.9894	60	0.9205	0.9205
90	0.9646	0.9646	90	0.9054	0.9054
100	0.9626	0.9626	100	0.9035	0.9035
120	0.9601	0.9601	120	0.9010	0.9010
150	0.9573	0.9573	150	0.8992	0.8992
180	0.9552	0.9552	180	0.8975	0.8975
200	0.9545	0.9545	200	0.8965	0.8965
240	0.9519	0.9519	240	0.8934	0.8934
270	0.9513	0.9513	270	0.8924	0.8924

Table B-11: Data availability of the LiDAR measurements collected at BHI-1-LB and BHII-1-LB.

B.2.4 Data reliability and validity

Although the verification reports are not available at the moment, C2Wind understands from the references in [EIBSDR] that the most critical instruments installed on the FLSs passed their calibration tests. Furthermore, comparisons and correlations against nearby datasets such as the KFII FLSs or Vortex series show that the EIBS FLSs record reasonable values. Finally, Figure B-9 shows that the FLSs have been located close to their deployment positions without signs of drift.

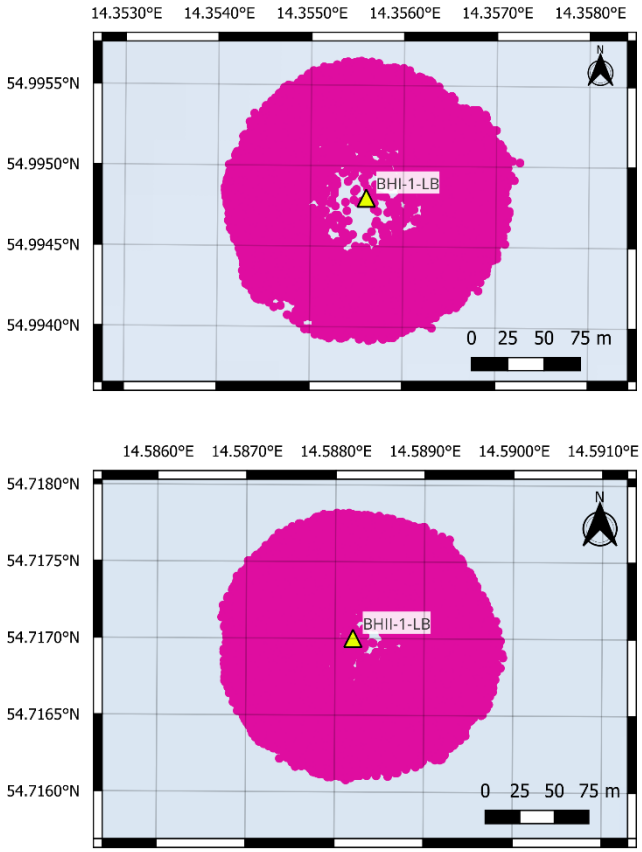

Figure B-9: Measurement location of all 10-minute statistics for BHI-1-LB and BHII-1-LB used in the analysis this document. CRS: WGS84.

B.3 FINO2 met mast

The FINO2 met mast is located approximately 38 km north of the island of Rügen in the Baltic Sea, near the limits of the Danish-, German and Swedish EEZs. The mast is located next to the Baltic 2 and Kriegers Flak I OWFs, both of which commenced operations several years after the met mast was installed.

ID	Latitude [°N]	Longitude [°E]
FINO2 mast	55.0083	13.15417

Table B-12: Coordinates of the FINO2 met mast.

Data from the FINO2 met mast covering the period 2008-01-01 to 2024-08-01 was downloaded from [FINO]. The dataset is described in detail in [FINOFR] and [FINO2MD], and the detailed descriptions are omitted herein for brevity.

B.3.1 Instrumentation setup

The instrumentation on the mast is summarised in the table below. In addition to the signals listed therein, a rain gauge was installed at 90 m, but its data proved to have poor coverage and was not used in the present document. Furthermore, a signal labelled sea surface temperature exists in [FINO] and according to [FINO2MD] it is measured using an IR pyrometer mounted at 11 mMSL. The quality of this signal was found to be rather poor and it is thus not used in this document.

Parameters	Instrument	Elevations*	Calibration certificate
		[mMSL]	
Wind speed	Vector A100 cup anemometer	102, 92, 82, 72, 62, 52, 42, 32	Y
Wind direction	Thies wind vane	91, 71, 51, 31	N
Wind speed & direction	Thies ultrasonic anemometer**	82, 62, 42	N
Air temperature	Thies thermometer	99, 70, 50, 40, 30	N/A
Air pressure	Vaisala barometer	90, 30	N/A
Relative humidity	Thies hygrometer	99	N/A

* The elevations listed correspond to those embedded in the data files downloaded from [FINO], which differ from those reported in [FINO2MD]. The discrepancy is between 0.4 m and 0.5 m for anemometers, and up to 0.8 m for wind vanes. C2Wind considers this minor discrepancy inconsequential for the use given to the dataset in this document.
** The 3D ultrasonic anemometers have not been used in this document.

Table B-13: Instruments installed on the FINO2 met mast.

B.3.2 Data description

The data available at [FINO] was downloaded in the form of an individual netcdf file covering the entire measurement period for each signal type. All wind speed signals from cup anemometers existed in a base version and a mast-corrected version. The mast correction is according to [FINOFR] done with the Uniform Ambient Mast flow method (UAM) briefly presented in [PO164]. C2Wind notes that as per the description of the UAM method in [PO164] and [FINOFR], it fits a logarithmic profile to the measurements under unstable conditions – determined from air- and water temperature differences – and for undisturbed direction sectors, then applying this profile to the top anemometer to derive the correction. No correction is applied to the top anemometer and, as per C2Wind's

reading of [PO164] and [FINOFR], only mean values are corrected, ie. no correction is applied to standard deviation. The effects of the correction are illustrated in Figure B-10.

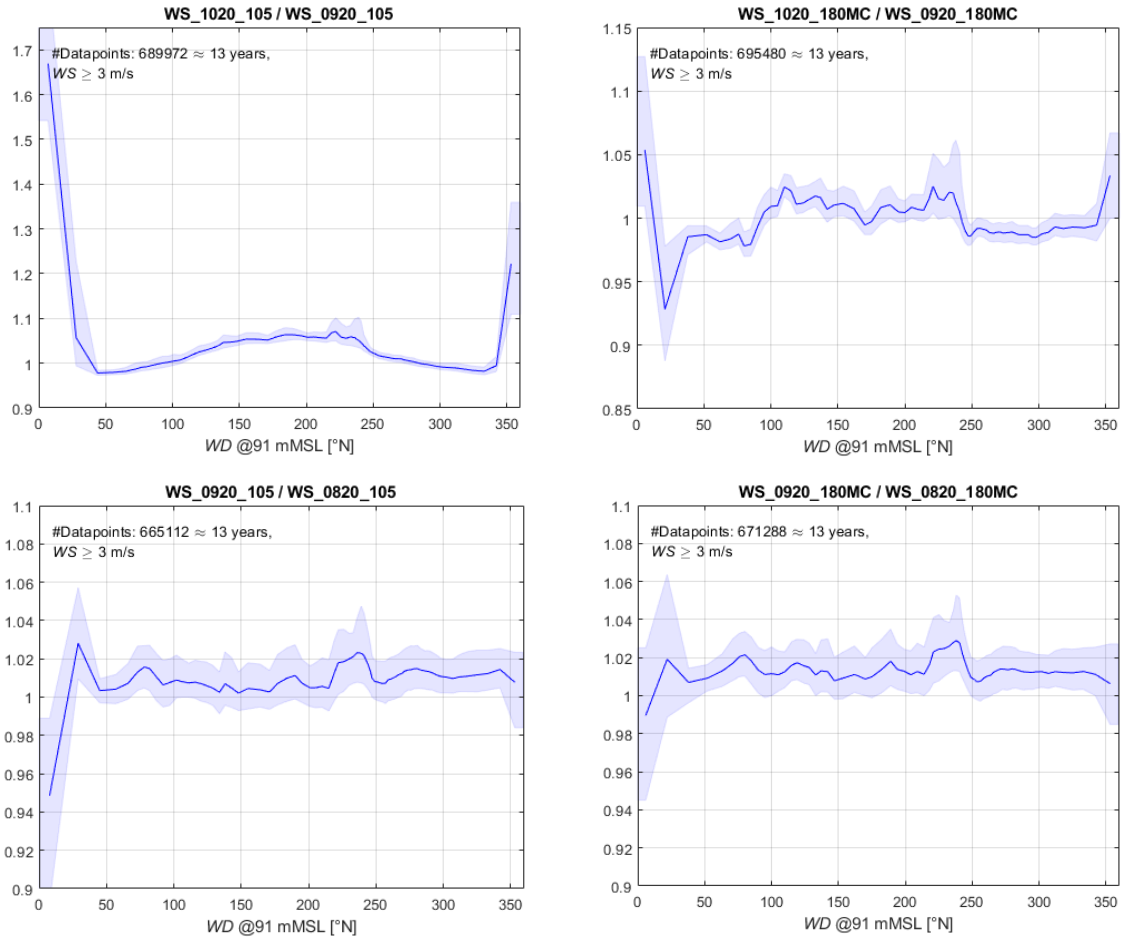

Figure B-10: **Top**: ratio of wind speed measured at 102 mMSL and 92 mMSL. **Bottom**: ratio of wind speed measured at 92 mMSL and 82 mMSL. The left part of the figure shows data without mast-effect correction and the right part shows the results with the mast-effect corrected dataset.

B.3.3 Data availability

The main instruments were found to have excellent data availability as summarised in Figure B-11.

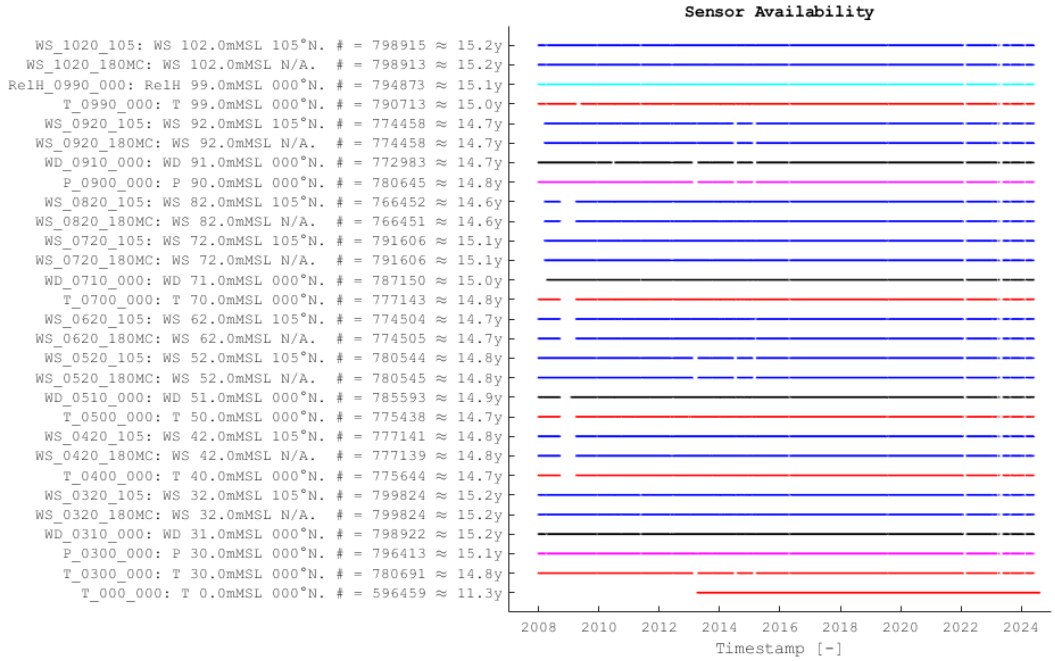

Figure B-11: Sensor availability for the FINO2 dataset.

B.3.4 Data reliability and validity

While the figure above shows that the mast correction does indeed seem to remove disturbance from the boom-mounted anemometers, it does not address flow disturbance on the top anemometer caused by the lightning rod, as seen in Figure B-12. Furthermore, it is clear from the top part of Figure B-13 that the turbulence intensity measurements at the FINO2 mast are heavily affected by the nearby Baltic 2 OWF, which has its nearest WTGs at just a few rotor diameters from the mast as seen in Figure B-12. In order to address these issues when using the dataset:

- When using the dataset for turbulence intensity analyses, the dataset is trimmed and all data recorded after 2015-04-01 (date of commissioning of the first WTG in Baltic 2) is ignored.
- When using the dataset for turbulence intensity analyses, wind directions in the range [5°; 25°], where the lightning rod is upwind of the top-mounted anemometer and causes a local maximum in directional *TI*, are filtered out of the analysis.
- When using the dataset for EVAs and analyses of extreme conditions, the entire dataset is used to allow for EVAs based on a much longer measurement period and since the WTGs are likely to reach their cut-out wind speed at the wind speeds of interest.

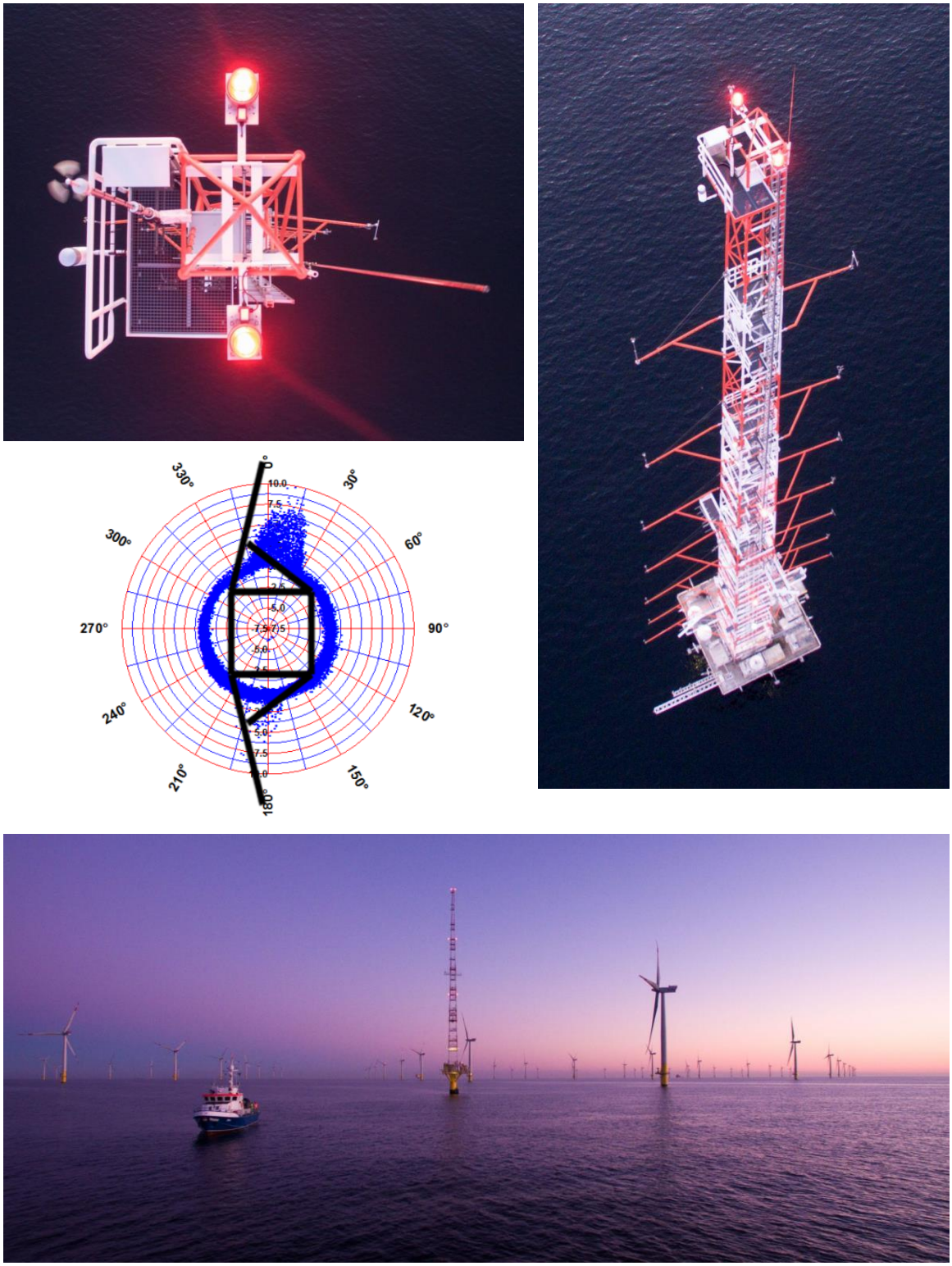

Figure B-12: Photos of the FINO2 met mast, along with a diagram of mast flow distortion. Reproduced from [FINOFR] and [FINO].

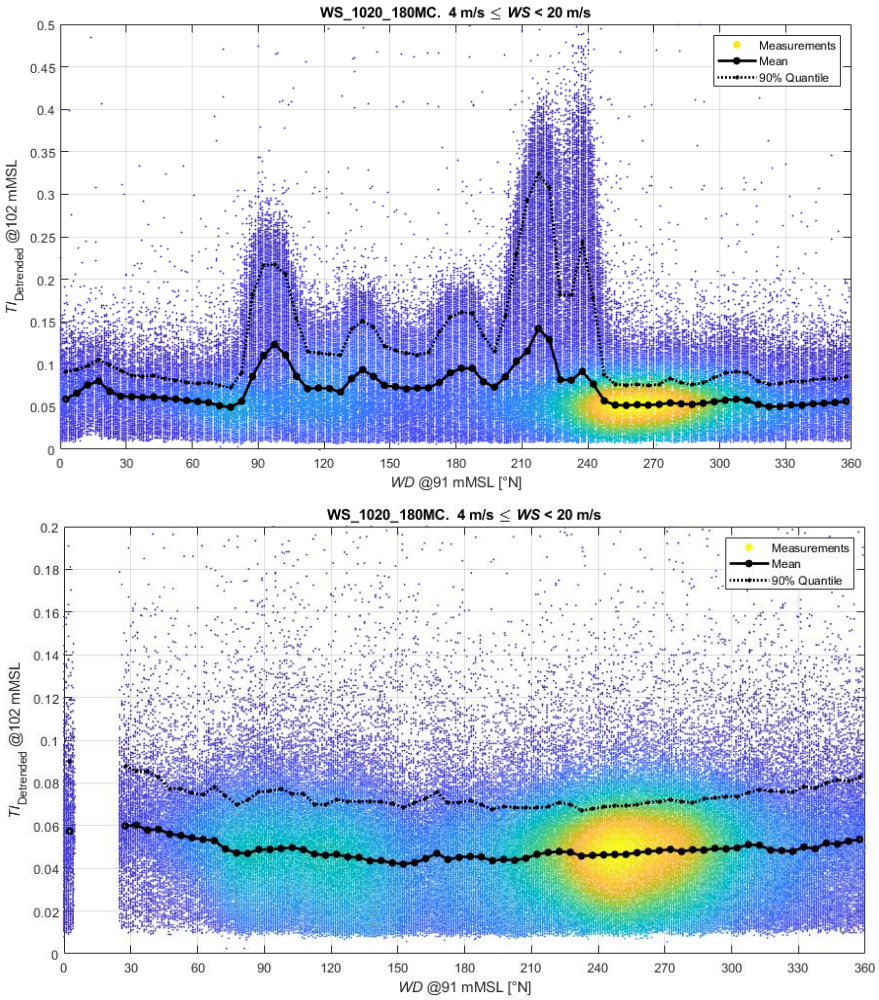

Figure B-13: Mean- and 90% quantile detrended *TI* binned in 5° wind direction sectors from the mast-corrected top-mounted sensor at the FINO2 met mast. The top subplot shows the entire dataset, while the bottom subplot shows only a subset where all data after 2015-04-01 has been removed, and wind directions in the range [5; 25]° have been ignored.

B.4 Arkona met mast

The Arkona met mast is located approximately 40 km northeast of the island of Rügen in the Baltic Sea. The mast is located next to the Wikinger and Arkona Becken Südost OWFs, both of which commenced operations several years after the met mast was installed.

ID	Latitude [°N]	Longitude [°E]
Arkona mast	54.7874	14.1698

Table B-14: Coordinates of the Arkona met mast.

B.4.1 Instrumentation setup

The Arkona mast is a triangular lattice with a top-mounted anemometer and two boom-mounted anemometers at several levels, as summarised in Figure B-14. A detailed description of the instrumentation and dataset is available in [ARKDEV], which also provides details on the calibration certificates and parameters for all anemometers.

General Measurement Features	
Measurement Mast Coordinates	Eastings: 446612, Northings: 6071451 (UTM-WGS 84, Zone 33);; altitude: a.s.l.
Measurement Data	2012-04-01 – 2012-05-31
Sensor Types	Thies Classic cup anemometers at 95 m, 93 m (2x), 80 m (2x), 70 m (2x), 60 m (2x), 48 m (2x), 32 m (2x) & 18 m (2x) heights; Thies wind vanes at 93 m, 70 m, 60 m, 48 m & 32 m heights; Temperature sensors at 93 m and 15 m heights; Pressure sensor (height not specified). Humidity sensors at 93 m and 15 m heights;
Mounting Details	Anemometer boom angular orientations: 95 m (top), 93 m (72.4°), 93 m (312.4°), 80 m (192,4°), 80 m (72.4°), 70 m (192.4°), 70 m (312.4°),60 m (72.4°), 60 m (312.4°), 48 m (72.4°), 48 m (192.4°), 32 m (192.4°), 32 m (312.4°), 18 m (72.4°) & 18 m (312.4°); Wind vane boom angular orientations: 93 m (12.4°), 70 m (252.4°), 60 m (12.4°), 48 m (132.4°) & 32 m (252.4°).
Data Logging System	PC based data logging system, as described in [5] – [9]
Mast Type	Lattice steel mast (triangular shape) – height: 95 m
Data Availability	Primary (top) anemometer: 100 % (filtered orig. data)

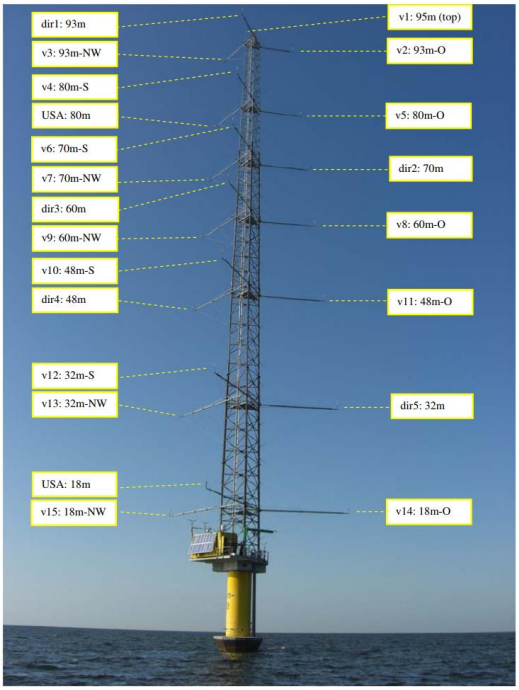

Figure B-14: Overview of instrumentation on the Arkona mast, reproduced from Table 1 and Figure 2 of [ARKDEV]. Please note that the dataset shared with C2Wind is only a subset of this, as described in Appendix B.4.2.

B.4.2 Data description

Only a subset of the dataset described above was shared with C2Wind for the present analysis. Key among this, the top-mounted anemometer was not part of the available dataset, as summarised in the table below.

Parameters	Instrument	Elevations	Orientation	Calibration certificate
		[mMSL]	[°]	
Wind speed	Thies Classic anemometer	93, 80, 70	312, 192, 192	Y
Wind direction	Thies wind vane	93, 70, 60, 48	12, 252, 12, 132	N
Air temperature	Thermometer	93, 15, 0		N/A
Air pressure	Barometer	11, 11		N/A
Relative humidity	Hygrometer	15, 0		N/A

Table B-15: Instruments installed on the Arkona met mast.

B.4.3 Data availability

The main instruments were found to have excellent data availability as summarised in Figure B-15.

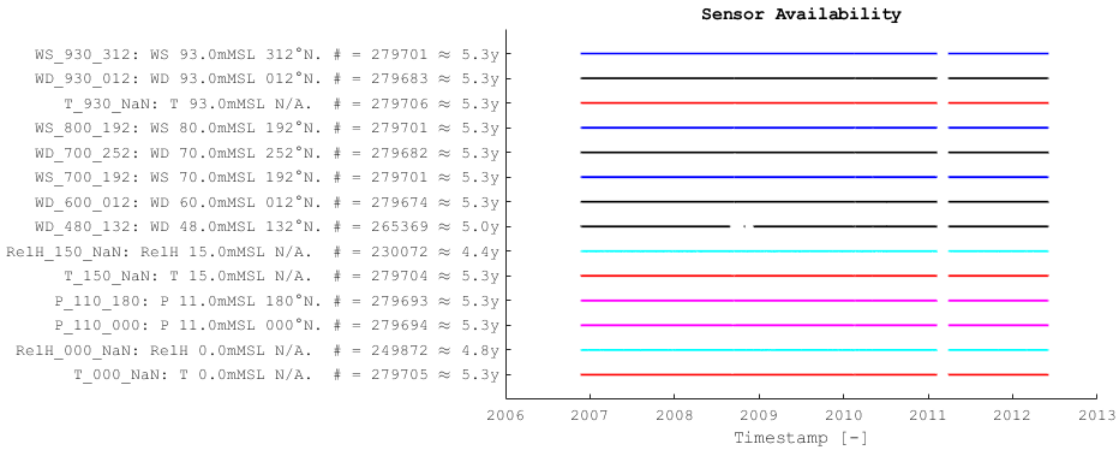

Figure B-15: Overview of sensor availability for the Arkona dataset.

B.4.4 Data reliability and validity

The plots in Figure B-16 show that the dataset has not been corrected for mast effects, neither regarding mean wind speed nor turbulence. As only one signal has been made available at each elevation, it is not possible to replicate a mast-effect correction similar to that in the FINO2 dataset. Nevertheless, since this dataset will not be used to prescribe turbulence intensity values, and it will be used in a supporting capacity for EVA, this limitation is of little impact for the purposes of the present document and the anemometer at 93 mMSL will be used uncorrected.

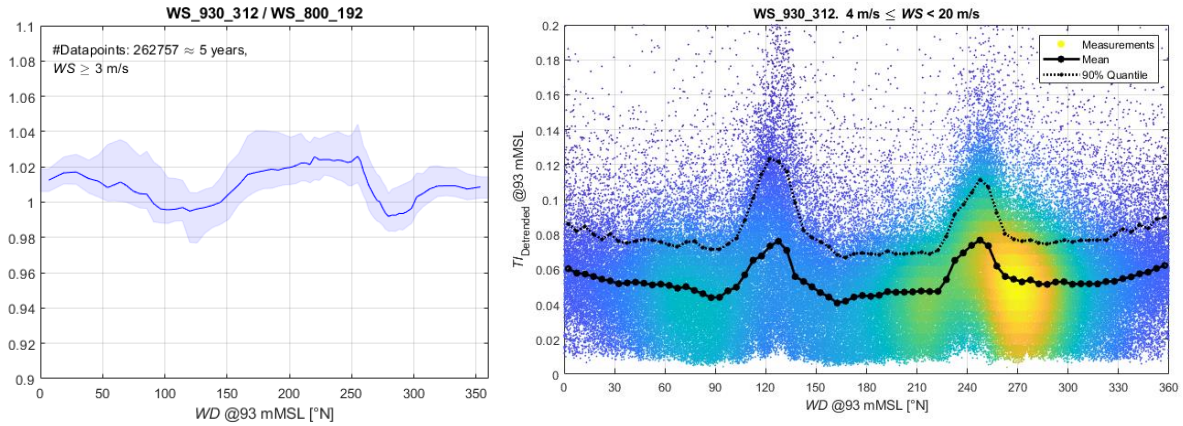

Figure B-16: **Left**: ratio of mean wind speed measured at the 93 mMSL- and 80 mMSL anemometers as a function of wind direction. **Right**: Turbulence intensity measured at 93 mMSL as a function of wind direction.

Appendix C. Turbulence Intensity Conditions

This appendix provides an analysis of freestream turbulence conditions offshore, applicable to sites located far from shore where the influence of land is negligible. For the results presented herein to be applicable, the minimum distance to the coastline varies depending on the type of onshore roughness and orography. As per the discussion in Section 2.7 of [POLLAK], and the conclusions of [PO293], such coastal effects can be considered negligible for distances larger than 20 km, however, a site-specific analysis is always required.

Furthermore, this appendix argues that either of the four met mast datasets considered in the analysis (IJmuiden, Dogger Bank West, FINO1, FINO2) form a sound basis for characterizing turbulence intensity conditions at offshore sites. In effect:

- The analysis demonstrates that sea surface roughness and atmospheric stability affect turbulence conditions in a similar fashion at all four sites.
- A simple model is provided, explaining the mechanism as play.
- Roughness and atmospheric stability conditions are similar at KFII and FINO2, thereby this dataset is applicable. Furthermore, use of any of the other datasets (from sites with more prevalence of unstable conditions) would result in a conservative choice for KFII.

Eventually, and following the same argumentation as in [THORWA], namely that the dataset is several years long, of high quality, and contains mean wind speed (lidar) measurements near the considered hub height, the IJmuiden dataset is highlighted as suitable for deriving the Normal Turbulence Model at offshore sites, especially in the North Sea but also possibly in other regions.

In the remainder of this appendix, atmospheric stability is characterized using the Obukhov length computed from ERA5 time series.

C.1 Note on measurement datasets

The measurement datasets used in the analysis come from four publicly available cup anemometer datasets:

- The IJmuiden met mast in the Dutch North Sea, documented in Section 4 of [THORWA].
- The FINO1 dataset, documented in [FINO].
- The Dogger Bank West (DBW) dataset, documented in [DBW].
- The FINO2 dataset, documented in [FINO].

For each dataset, only freestream conditions have been selected (i.e. no wakes from neighboring wind farms, or from the mast). For DBW, the cup anemometers mounted on the booms pointing to the Northwest have been used (measurements from the opposite anemometers are erroneous due to a mismatch between the logger and the type of anemometer).

C.2 Introduction

In the Atmospheric Boundary Layer (ABL), the mean- and turbulent quantities of the wind flow are interlinked. A simple (yet realistic and well-accepted) expression of the dependency of the mean wind speed $\overline{\mathrm{U}}$ with the elevation above the surface, z is provided in Eq. C-1, see background and references in [GG24], where:

- $\overline{\mathrm{U}} = \mathrm{U(t)} - \mathrm{u'(t)}$, with $\mathrm{u'(t)}$ the short-term fluctuations over typically 10- to 30min[8].
- u_{*0} is the friction velocity at the surface (proportional to the square root to the vertical momentum flux $\overline{\mathrm{u'w'}}$).
- z_0 is the roughness length, itself a function of u_{*0} (see below).
- $\mathrm{L} =$ is the Obukhov length, a measure of atmospheric stability.
- ψ_{m} is a stability-dependent function, derived from the Monin-Obukhov Stability Theory (MOST) and experiments.
- κ is the Von Karman constant (here taken equal to 0.4), and $\mathrm{g(z, z_i, L_{MBL})}$ is a function of z, the ABL height $\mathrm{z_i}$ and an additional length scale $\mathrm{L_{MBL}}$ (characterizing turbulent eddies in the middle of the ABL); see [GRYNING07] and [GG24].

$$\overline{U}(z) = \frac{u_{*0}}{\kappa}\left(ln\left(\frac{z}{z_0}\right) - \psi_m\left(\frac{z}{L}\right) + g(z, z_i, L_{MBL})\right) \qquad \text{Eq. C-1}$$

The Turbulence Intensity (*TI*) is the ratio of the standard deviation of the longitudinal component of the horizontal wind speed $\sigma_U = \overline{u'u'}^{1/2}$ and the mean wind speed $\overline{\mathrm{U}}$ derived from Eq. C-1:

$$\mathrm{TI(z)} = \frac{\sigma_{\mathrm{U}}(\mathrm{z})}{\overline{\mathrm{U}}(\mathrm{z})} \qquad \text{Eq. C-2}$$

Offshore, the roughness length varies with u_{*0} (wave height increases with wind speed), this is most often described using a Charnock relationship, see Eq. C-3 and [GG24], where:

- α_{Ch} is the Charnock parameter, either constant or sea state dependent.
- α_{M} is a parameter linking u_{*0} and ν, the air kinematic viscosity (a term only relevant for very small wind speeds, smaller than 3 m/s at 10 mASL for instance)

$$\mathrm{z_0} = \alpha_{\mathrm{Ch}} \cdot \frac{\mathrm{u}_{*0}^2}{\mathrm{g}} + \alpha_{\mathrm{M}} \cdot \frac{\nu}{\mathrm{u}_{*0}} \qquad \text{Eq. C-3}$$

An illustration of the dependency of u_{*0} and z_0 with wind speed for neutral conditions ($\psi_{\mathrm{m}}\left(\frac{\mathrm{z}}{\mathrm{L}}\right) = 0$) is shown in Figure C-1.

[8] In this study, 10-minute measured statistics have been used, and no detrending (linear, or high-pass filter) have been applied.

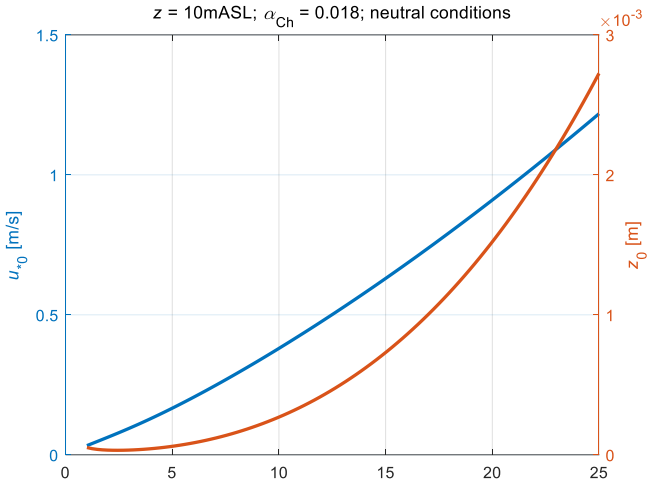

Figure C-1: Illustration of the relationship between wind speed (x-axis), roughness length (right y-axis) and friction velocity (left y-axis).

Mean wind speed and turbulence are thereby primarily driven by atmospheric stability and sea surface roughness. When accounting for differences in elevation, sea state and stability, turbulence conditions are similar across far offshore locations. This is illustrated in Figure C-2 and Figure C-3, where binned mean and standard deviation values of σ_U and TI are plotted for the four met mast datasets and four distinct atmospheric stability classes. The IJmuiden dataset tends to show slightly larger *TI* values due to its lower elevation and a slightly larger portion of large TI values caused by low-frequency outliers.

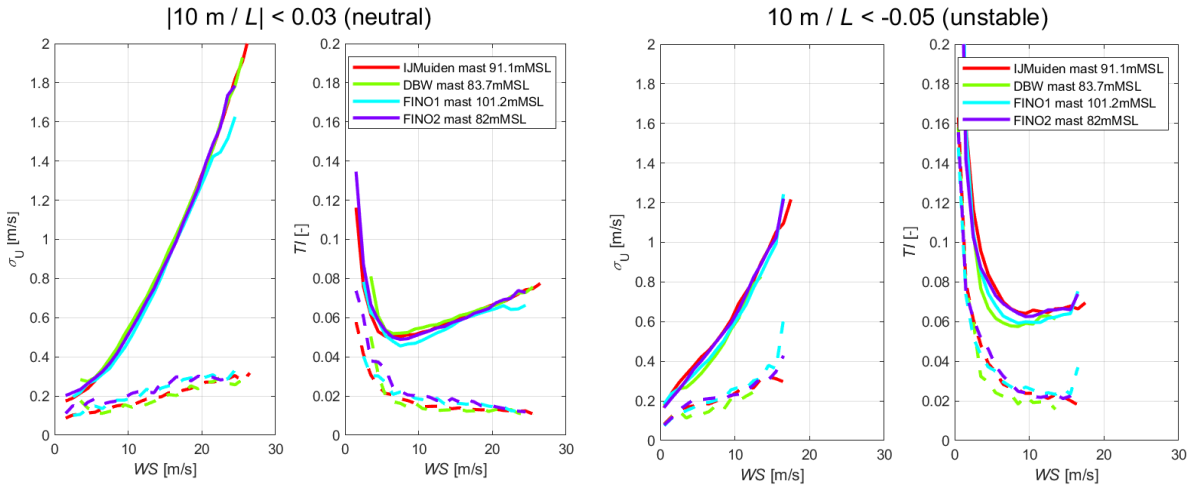

Figure C-2: Mean (full line) and standard deviation (dashed line) of σ_U and TI measured at four different offshore met masts, for neutral (left) and unstable (right) conditions.

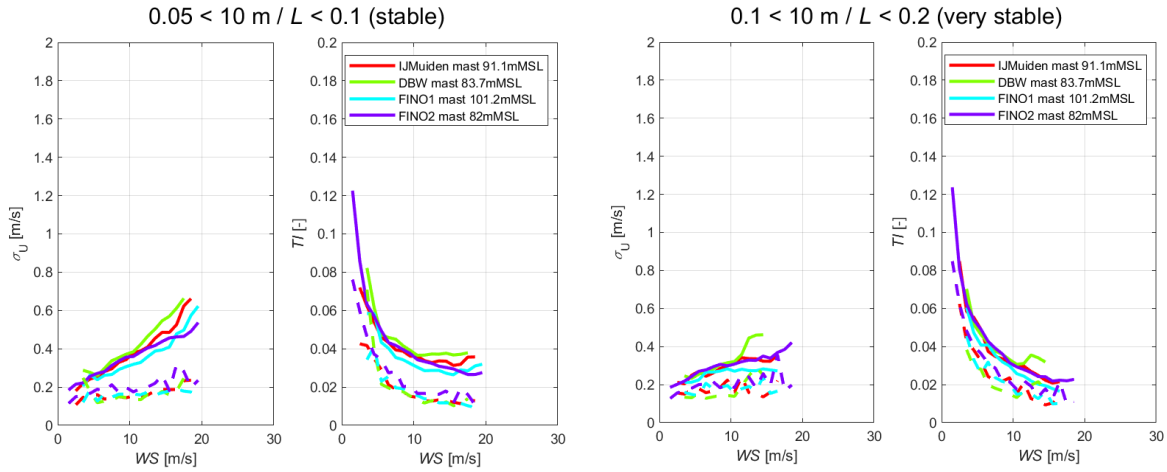

Figure C-3: Mean (full line) and standard deviation (dashed line) of σ_U and TI measured at four different offshore met masts, for stable (left) and very stable (right) conditions.

C.3 Turbulence Intensity Modelling

Modelling $TI(z)$ consists of modelling $\sigma_U(z)$ and $\overline{U}(z)$. The latter can be done using Eq. C-1, and for the former several approaches have been proposed:

1) Fitting $\sigma_U(\overline{U(z)})$ from measurement datasets, see Section 5.4.1 of [EMEIS18].
2) Assuming that $\sigma_U(z)$ is proportional to u_{*0}, or can be derived from stability-dependent surface layer spectra.
3) Deriving $\sigma_U(z)$ from $k(z)$ where k is the turbulent kinetic energy, derived from a mesoscale model, see [DTU24].
4) Deriving σ_U from turbulence scaling laws, see [WANG14] or [MATAJI22].

A summary of the pros and cons for each method is provided in Table C-1.

Method	Pro	Cons
1)	Simple, when measurements are available.	Only valid for the elevation and atmospheric conditions matching the subset of data used for fitting.
2)	Requires only u_{*0} which can be derived from a simple algorithm such as COARE, or directly obtained from model data.	Assuming $\sigma_U(z) \sim u_{*0}$ leads to an overestimation of TI at large elevations. The Kaimal spectral forms were derived using a measurement in the surface layer (32 m tower in the Kansas experiment), and the validity of the relationship $\sigma_U(z)/u_{*0}$ needs to be demonstrated offshore at large elevations.
3)	Can be derived using model data.	Requires elevation-specific tuning, and the conversion from k to σ_U remains heuristic.
4)	Based on physical scaling laws.	Requires validation in offshore wind energy context.

Table C-1: Summary of the pros and cons of four different methods to model $\sigma_U(z)$.

An example of the conservatism implied by the assumption $\sigma_U(z) \sim u_{*0}$ is provided below. This method is proposed in Section 6.4.3.3 of [IEC6131]. There, it is assumed implicitly that:

$$\sigma_U(z) = 2.5 \cdot u_*(z) = 2.5 \cdot u_{*0}(z) \qquad \text{Eq. C-4}$$

This is a classical approach, derived from surface-layer results published in the 1980s, see [PANOF84] and Section 3.1.2 of [FRANDSEN92]. Since $1/\kappa = 2.5$, this conveniently leads to:

$$\sigma_U(z) = 2.5 \cdot u_*(z) = 2.5 \cdot u_{*0}(z) \qquad \text{Eq. C-5}$$

$$\sigma_U(z) = \frac{1}{ln\left(\frac{z}{z_0}\right)}$$

A constant value of $1.28 \cdot 4 \cdot TI(U = 15\ \mathrm{m/s})$ is then added to σ_U for computing the 90th percent quantile. As illustrated in Figure C-4 this leads to very conservative estimates, primarily due to the way the p_{90} is computed, and the assumption $\sigma_U(z) \sim u_{*0}$.

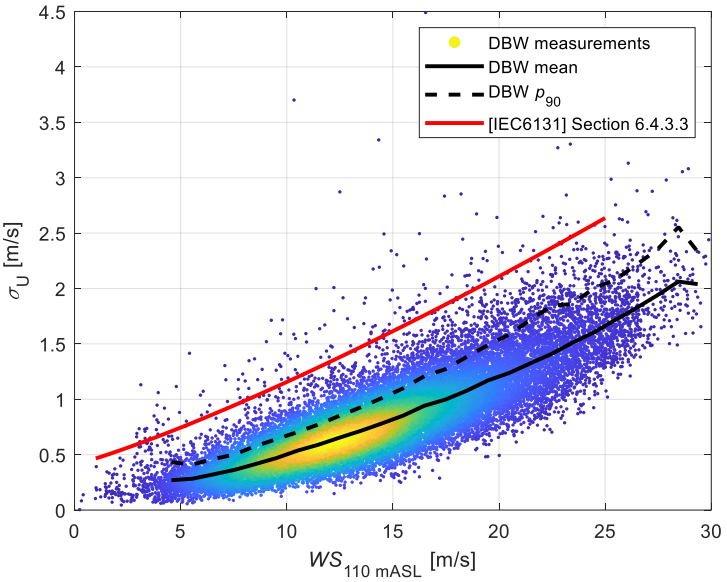

Figure C-4: This figure shows measured turbulence intensity values in neutral conditions at the DBW met mast (scatter, full and dashed black lines), and the 90th percent quantile modelled using the guidance in [IEC6131] (red line).

These shortcomings can be improved by choosing another way to derive $\sigma_U(z)$ from u_{*0}, for example:

- Using a neutral Kaimal spectrum formulation, a ratio $\sigma_U(z)/u_{*0}$ can be derived, but the resulting values (around 2.1) are still much larger than what is observed offshore at large elevations (around 1.6 at 90 mMSL at IJmuiden, from Figure 5 of [HOLTSLAG15]).
- Alternatively, the ratios $\sigma_U(z)/\ u_*(z)$ and $u_*(z)/\ u_{*0}$ can be parametrized as a function of atmospheric stability and/or ABL height, see [EMD18], but these remain heuristic.

To provide a physical basis for the relationship between $\sigma_U(z)$ and u_{*0}, the present report proposes to use a simple model based on the attached eddies hypothesis and the seminal work of [TOWNSEND76], consequently researched and validated both experimentally and numerically see [MARUSIC13] and [HWANG20]. The model leads to the following relationship:

$$\left(\frac{\sigma_U(z)}{u_{*0}}\right)^2 = B - A \cdot \ln\left(\frac{z}{\delta}\right)$$ Eq. C-6

where:

- δ is a characteristic length scale of the flow.
- $A = 1.26$ is a universal constant [MARUSIC13].
- B is flow-case dependent.

As for the MOST, this model relies on the assumption that the eddies' characteristic length grows proportionally to z. Two critical assumptions are listed in Section 2 of [MARUSIC19]: "(a) characteristic attached eddies are self-similar, meaning that their energy density is constant and their entire geometry scales only with distance from the wall, and (b) eddies have a constant characteristic velocity scale". Eq. C-6 is then derived assuming that $u_*(z) \approx u_{*0}$; this is not generally true in the ABL, as opposed to the type of channel flows studied in the previous references, but ABL-specific studies such as [TENNEKES73] have shown that a logarithmic profile can be obtained without having to assume constant shear stress, it is, therefore, possible that Eq. C-6 holds without having to make this assumption.

For the application to the offshore wind flow, δ is here set to z_i, which depends on atmospheric stability and u_{*0} (z_i increases with u_{*0} and decreases with increasing stability); this is analogous to the method used in [PUCCIONI22] (where the analysis is limited to neutral conditions).

A validation study is performed using:

- Measurements of $\sigma_U(z)$ from 5 cup anemometers (110.0, 104.5, 83.7, 53.5, 38.3 mMSL) at the Dogger Bank West met mast, for the wind directional bin [200; 360[° free from mast effects.
- u_{*0} derived using MOST (where L is computed from ERA5, and $\alpha_{Ch} = 0.018$) using wind speed from the lowest measurement elevation (38 mMSL).
- z_i is taken from ERA5.

As shown in Figure C-5 for unstable and neutral conditions the slope of $(\sigma_U(z)/u_{*0})^2$ as a function of $\ln(z/z_i)$ is very close to the universal value $A = 1.26$. For large wind speeds, a value $B = 0.6$ seems appropriate. The measured values depart from the Townsend model for small values, this is possibly due to low-frequency background turbulence (mesoscale). In effect, observations show that mean values of $\sigma_U(z)$ do not converge to 0 m/s for small values of u_{*0}. This is accounted for in a revised version of the Townsend model, defined below and shown with red dashed lines in Figure C-5:

$$\sigma_U(z)^2 = \sigma_{U,T}(z)^2 + \sigma_{U,bgd}(z)^2$$ Eq. C-7

where $\sigma_{U,T}(z)^2$ is computed using Eq. C-6 and $\sigma_{U,bgd}(z) = 0.2$ m/s.

Stable conditions are included in the analysis in Figure B-6. The suggested model overpredicts the measured values. This is possibly due to the overestimation of the ABL

height in ERA5, a known feature of this dataset [SINCLAIR22], [XI24]. To remediate this deficiency, ABL height values from ERA5 are divided by a factor of 2 for stable conditions ($10/L > 0.03$).

Modelled turbulence intensity is then obtained by combining Eq. C-7 and Eq. C-1. This model does not account for the stochasticity of the wind field, it provides a unique value of $\sigma_U(z)$ for given values of u_{*0}, L and z_i. Some stochasticity is inherently present in the ERA5 dataset, but the time series do not include microscale variability. For deriving a Normal Turbulence Model, the standard deviation of $\sigma_U(z)$, $\sigma_{\sigma_U}(z)$ is then computed as follows:

$$\sigma_{\sigma_U}(z)^2 = (C \cdot u_{*0})^2 + {\sigma_{\sigma_{U,bgd}}}^2 \qquad \text{Eq. C-8}$$

with $C = 0.3$ and $\sigma_{\sigma_{U,bgd}} = 0.125$ m/s, empirical values derived from the Dogger Bank West measurements, see Figure C-7.

The model is tested against measurements at the IJmuiden met mast (three elevations) and FINO1 (top sensor only), it generally captures both trends and magnitudes of turbulence well; see Figure C-8 to Figure C-12.

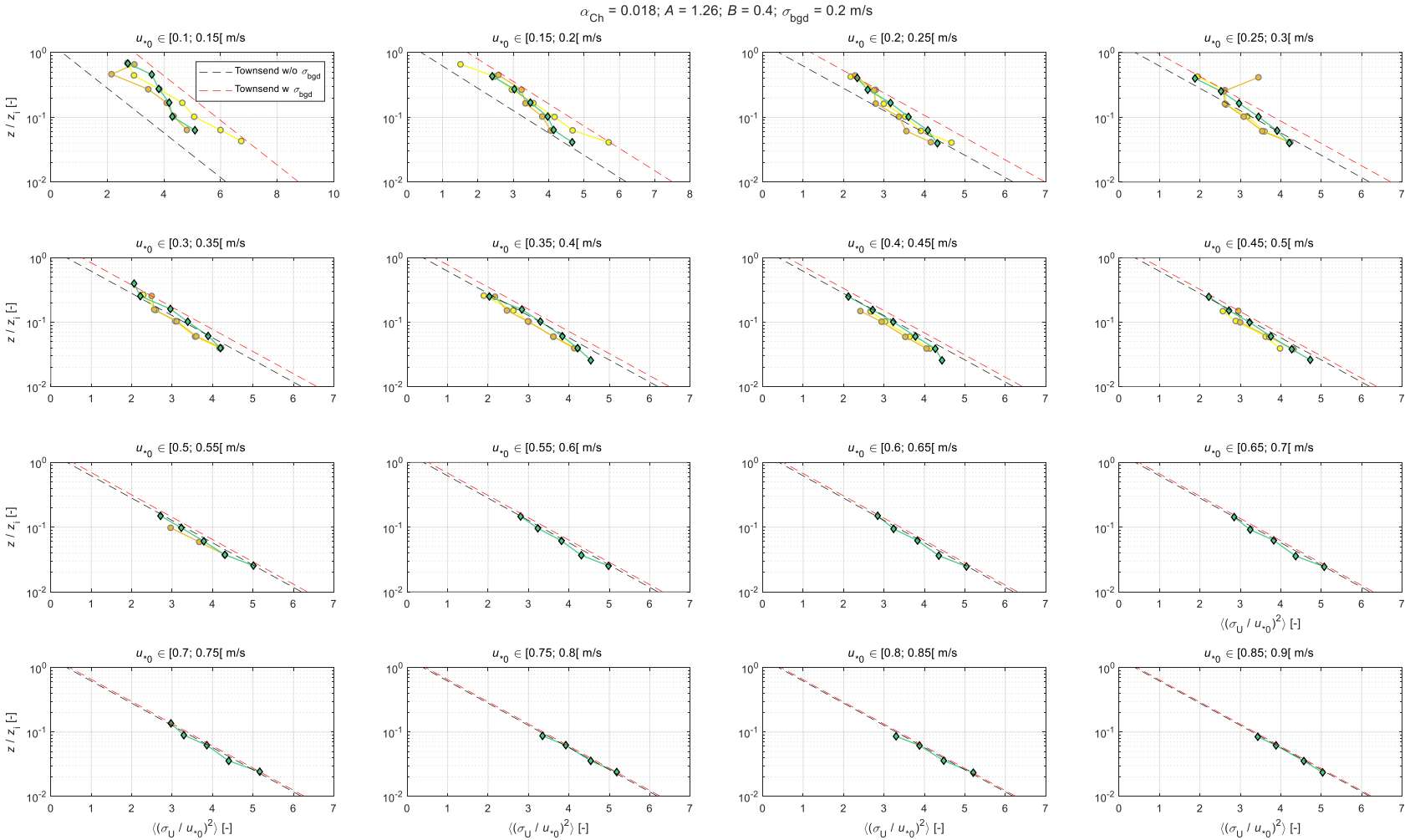

Figure C-5: For unstable (yellow), near-neutral unstable (brown) and neutral (green) stability conditions, and for several bins of surface friction velocity, this figure shows measured mean ratios $(\sigma_U(z)/u_{*0})^2$ as a function of z/z_i. The black line shows the original Townsend model (Eq. C-6), the red line shows the modified model (Eq. C-7).

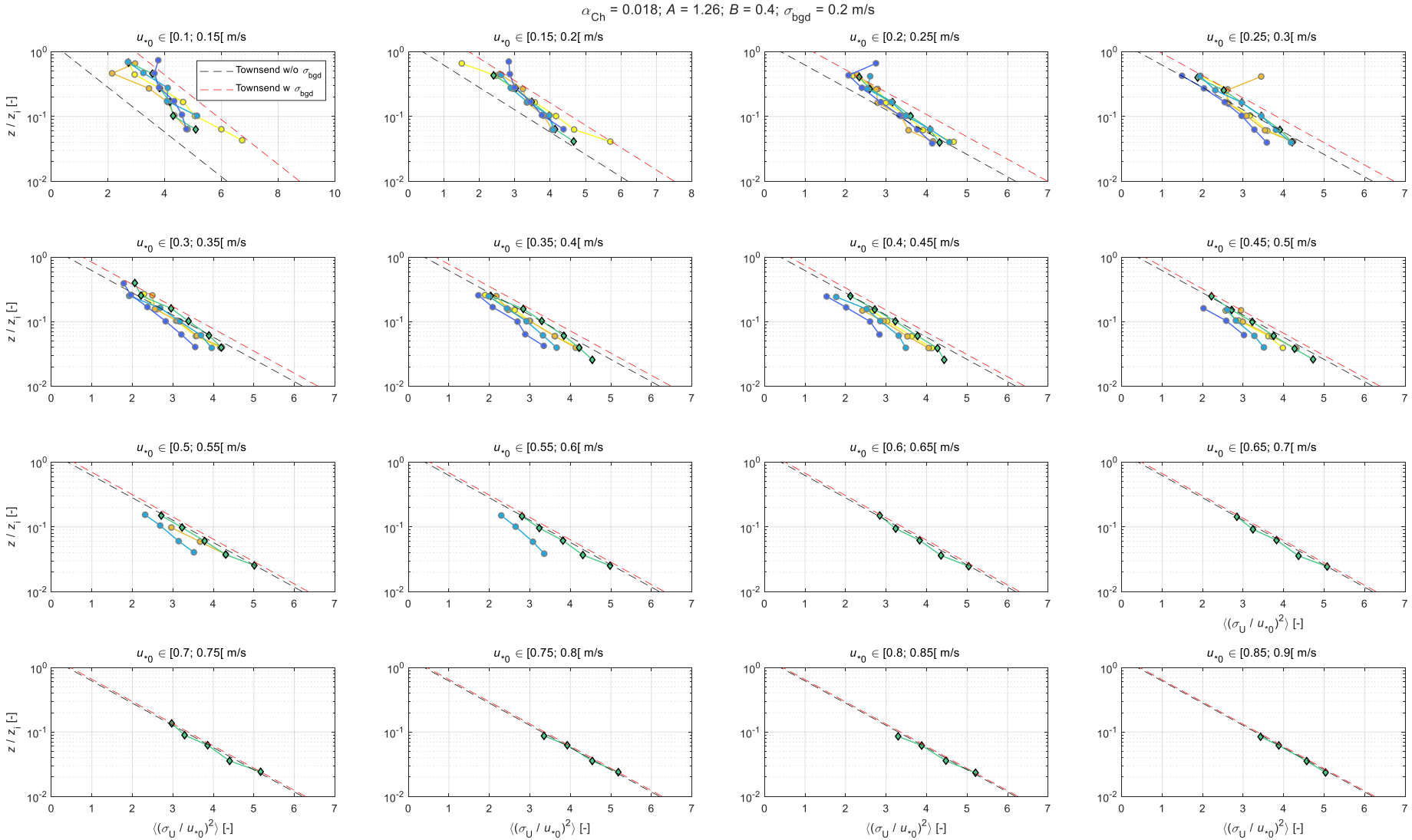

Figure C-6: Same as Figure C-5, with two additional stability classes: near-neutral stable (light blue), and stable (blue). The model overprediction of measured values for stable classes has been addressed as described in the text.

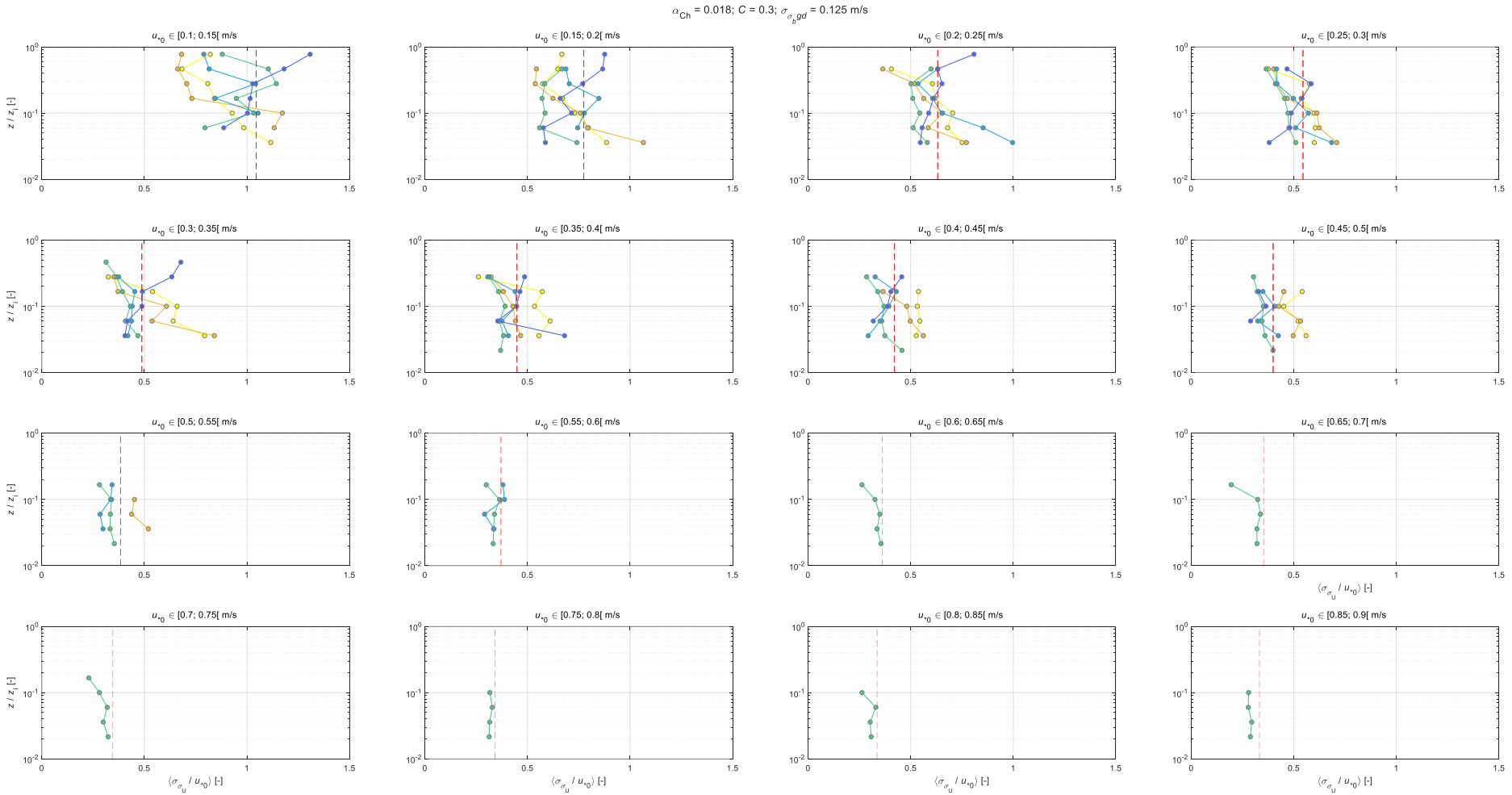

Figure C-7: Using the same colour code as in Figure C-6, this figure shows mean ratios of $\sigma_{\sigma_U}(z)/u_{*0}$ and the model results (Eq. C-8) with dashed red lines.

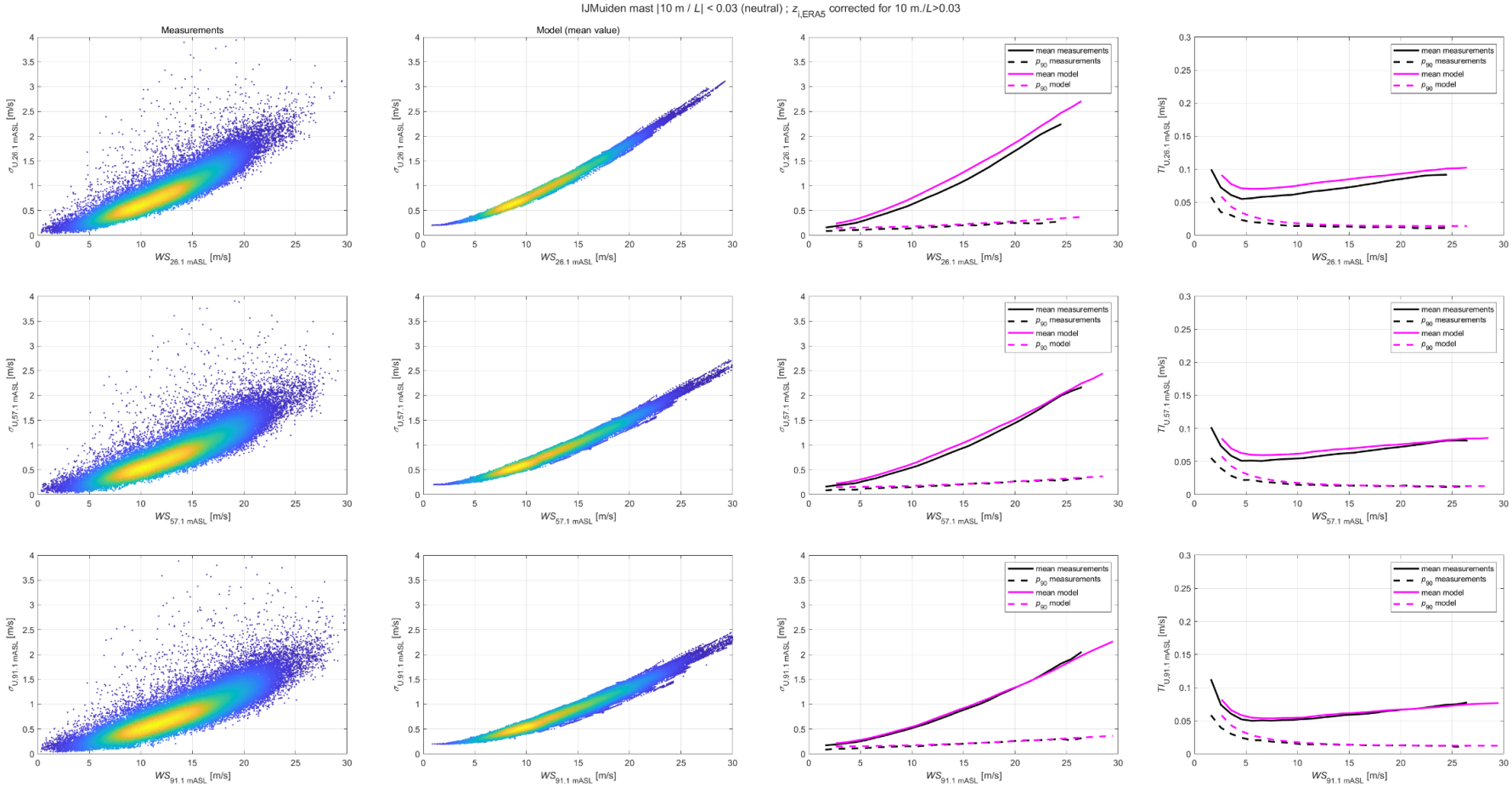

Figure C-8: For neutral conditions, comparison of measured and modelled turbulence values at the IJmuiden met mast.

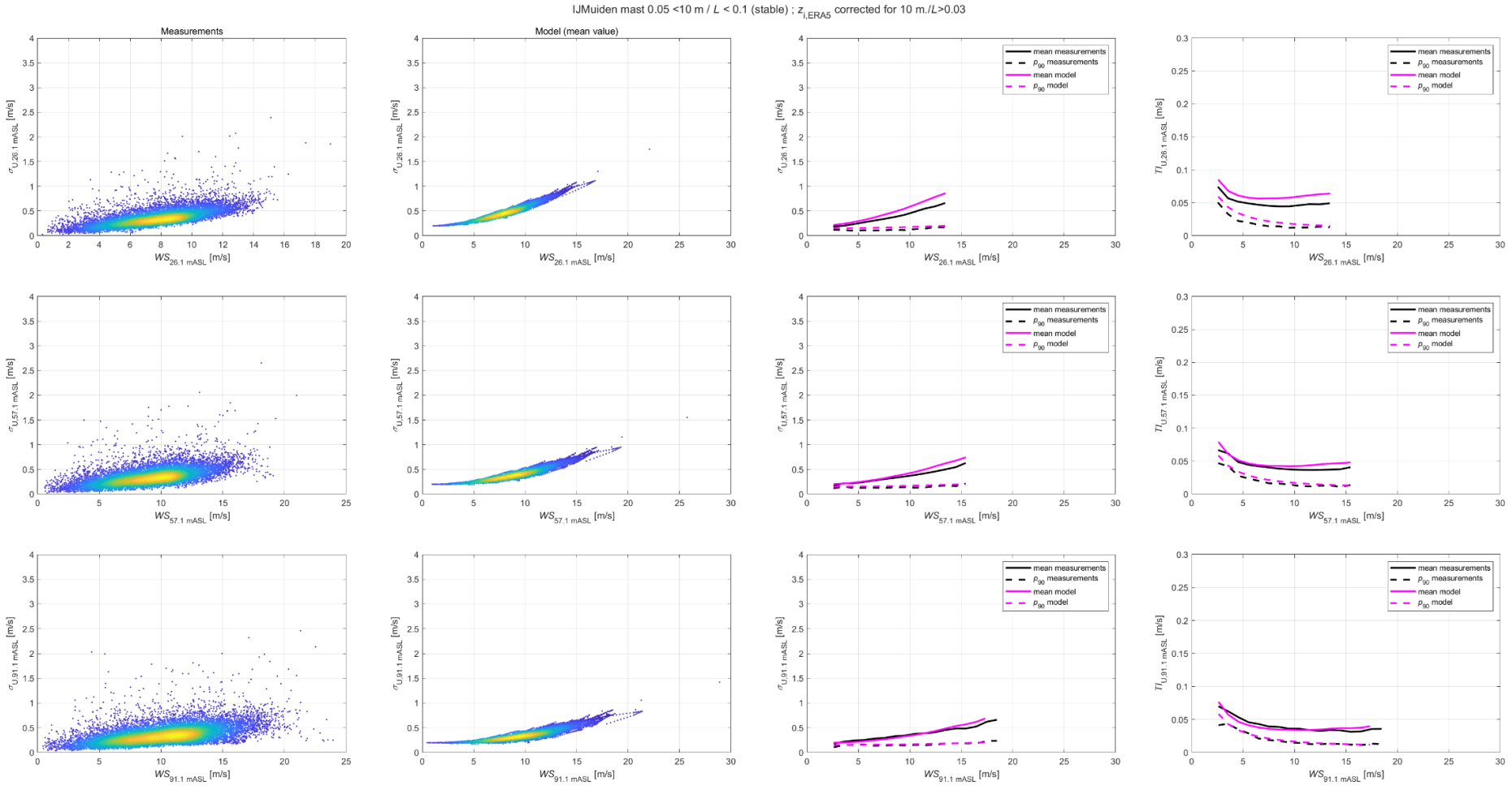

Figure C-9: For stable conditions, comparison of measured and modelled turbulence values at the IJmuiden met mast.

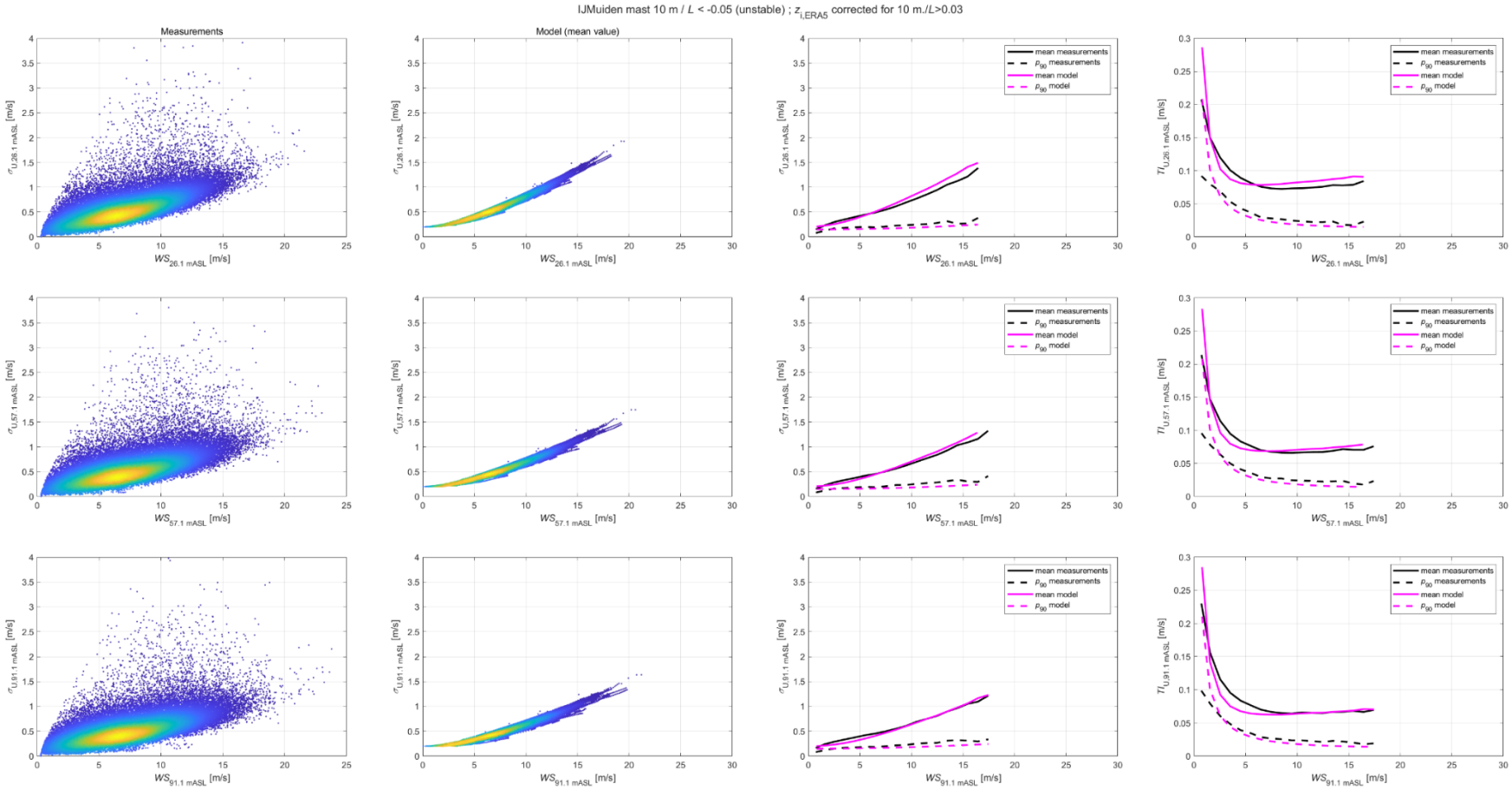

Figure C-10: For unstable conditions, comparison of measured and modelled turbulence values at the IJmuiden met mast.

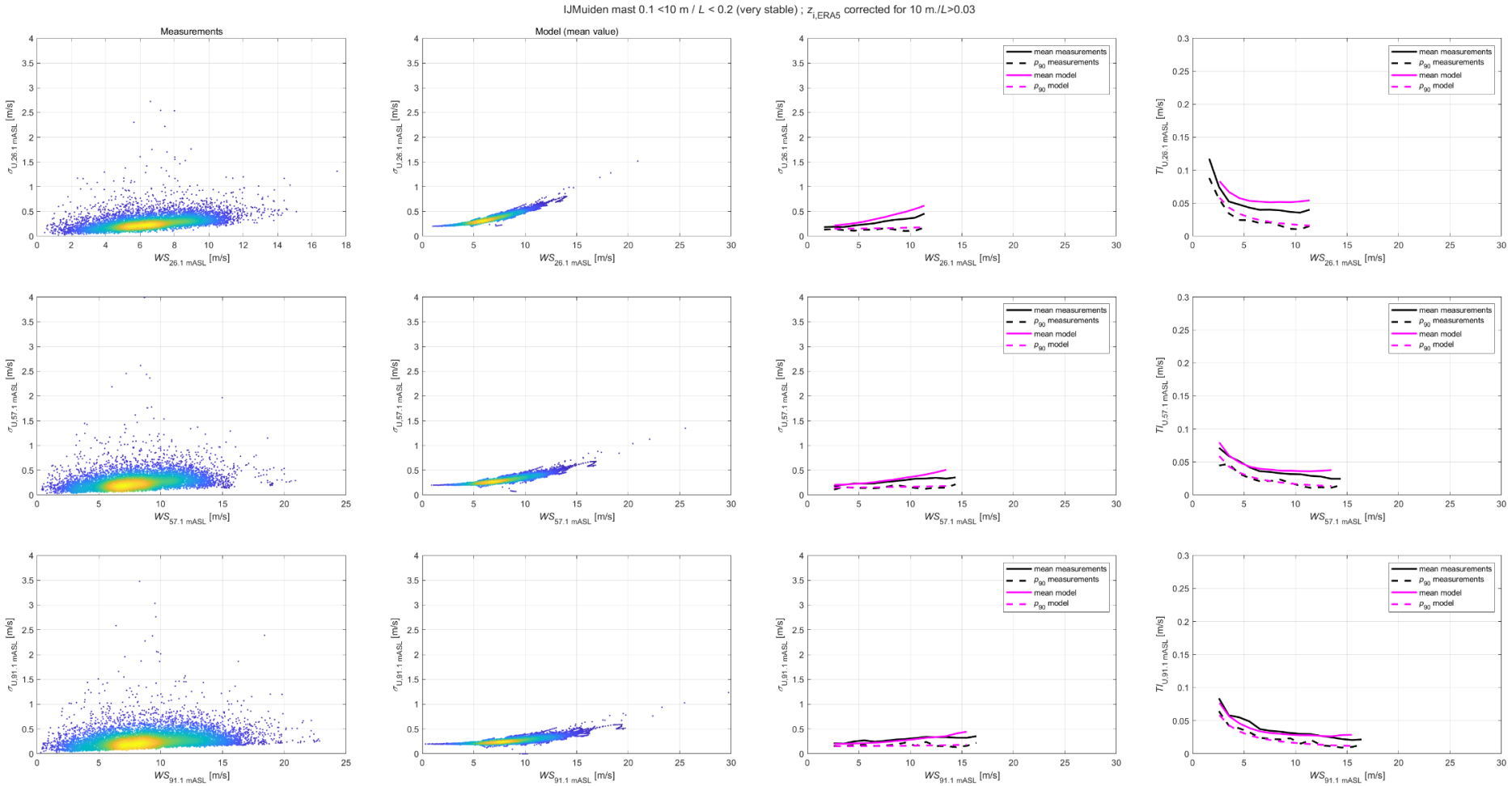

Figure C-11: For very stable conditions, comparison of measured and modelled turbulence values at the IJmuiden met mast.

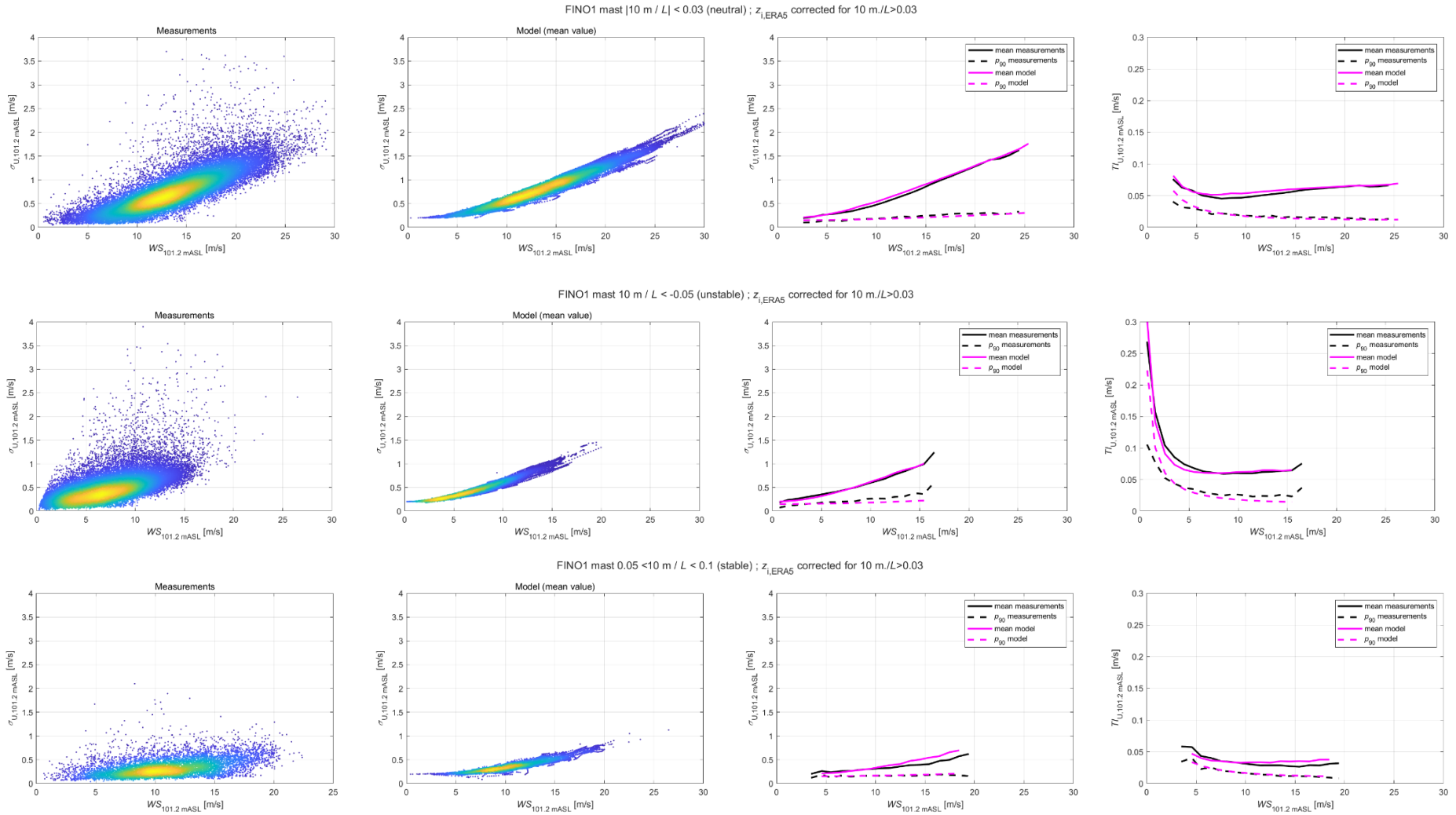

Figure C-12: For neutral, unstable and stable conditions, comparison of measured and modelled turbulence values at the FINO1 met mast.

C.4 Application to Kriegers Flak II

Figure C-13 shows mean *TI* modelled results (2000-2024) for the four met mast locations, as well as the Horns Reef 3 offshore wind farm location. As expected, due to the larger frequency of occurrence of stable conditions in the Baltic Sea, the model predicts smaller values at FINO2 than for the North Sea. The difference at large wind speeds between IJmuiden/DBW and FINO1/HR3 is due to z_i values being relatively smaller in the German Bight and close to the Danish coast. These results confirm the applicability of the IJmuiden dataset for characterising turbulence conditions at the Kriegers Flak II site, in either of two forms:

- As a confirmation that the values derived from the FINO2 dataset, although yielding relatively low ambient turbulence compared to other publicly available datasets, are reasonable when considering the atmospheric stability conditions at the site and the agreement with the independent model presented herein.
- As an alternative to the use of the FINO2 dataset, mitigating some of its shortcomings. For example, the IJmuiden dataset includes lidar-measured wind speeds near hub height, which reduces the uncertainty associated with the vertical extrapolation that for FINO2 is carried out over a distance of approximately 50 m using wind shear measured by boom-mounted anemometers.

While the present document has chosen the first of the two approaches above, the use of the IJmuiden dataset together with the turbulence model presented herein provides added confidence in the *TI* values concluded in this document.

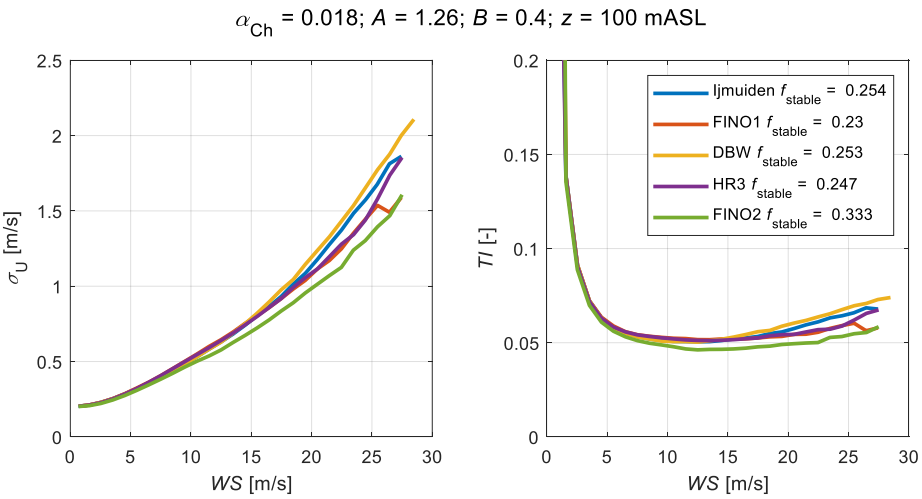

Figure C-13: Comparison of modelled *TI* values across several locations, see text.